Simulation Based Optimization of Complex Monolithic Composite Structures Using Cellular Core Technology

Curtis W. Hickmott

A dissertation

submitted in partial fulfillment of the

requirements for the degree of

Doctor of Philosophy

University of Washington

2015

Reading Committee:

Brian Flinn, Chair

Dwayne D. Arola

K. Bhagwan Das

Program Authorized to Offer Degree:

Materials Science and Engineering

University of Washington

Abstract

Simulation Based Optimization of Complex Monolithic Composite Structures Using Cellular Core Technology

Curtis W. Hickmott

Chair of Supervisory Committee:

Dr. Brian D. Flinn, Research Associate Professor

Materials Science and Engineering

Cellular core tooling is a new technology which has the capability to manufacture complex integrated monolithic composite structures. This novel tooling method utilizes thermoplastic cellular cores as inner tooling. The semi-rigid nature of the cellular cores makes them convenient for lay-up, and under autoclave temperature and pressure they soften and expand providing uniform compaction on all surfaces including internal features such as ribs and spar tubes. This process has the capability of developing fully optimized aerospace structures by reducing or eliminating assembly using fasteners or bonded joints. The technology is studied in the context of evaluating its capabilities, advantages, and limitations in developing high quality structures. The complex nature of these parts has led to development of a model using the Finite Element Analysis (FEA) software Abaqus and the plug-in COMPRO Common Component Architecture

(CCA) provided by Convergent Manufacturing Technologies. This model utilizes a “virtual autoclave” technique to simulate temperature profiles, resin flow paths, and ultimately deformation from residual stress. A model has been developed simulating the temperature profile during curing of composite parts made with the cellular core technology. While modeling of composites has been performed in the past, this project will look to take this existing knowledge and apply it to this new manufacturing method capable of building more complex parts and develop a model designed specifically for building large, complex components with a high degree of accuracy. The model development has been carried out in conjunction with experimental validation. A double box beam structure was chosen for analysis to determine the effects of the technology on internal ribs and joints. Double box beams were manufactured and sectioned into T-joints for characterization. Mechanical behavior of T-joints was performed using the T-joint pull-off test and compared to traditional tooling methods. Components made with the cellular core tooling method showed an improved strength at the joints. It is expected that this knowledge will help optimize the processing of complex, integrated structures and benefit applications in aerospace where lighter, structurally efficient components would be advantageous.

Table of Contents

Chapter 1: Introduction **13**

1.1 Motivation 13

1.2 Project Scope 14

1.3 Project Goal 15

1.4 Document Organization 16

1.5 Carbon Fiber Reinforced Polymer Composites 16

1.6 Processing Techniques for Fiber Reinforced Polymer Composites 18

1.6.1 Vacuum Bagging 18

1.6.2 Autoclave Processing 19

1.6.3 Bladder Molding 21

1.7 Cellular Core Technology (CCT) 22

1.8 Residual Stress Development in Fiber Reinforced Polymer Composites 25

1.9 Finite Element Analysis (FEA) 28

1.10 Process Modeling 29

1.10.1 COMPRO Common Component Architecture (CCA) 30

1.10.2 Raven Simulation Software 34

1.11 Literature Review of Process Modeling in Composites 34

1.11.1 Modeling of Flat Plate Laminates 35

1.11.2 Modeling of Angled Laminates 37

Chapter 2: Characterization of Composite Structures Processed with CCT **40**

2.1 Processing Defects in Composites 40

2.2 Mechanical Properties of Composite T-Joints 41

2.2.1 Digital Image Correlation (DIC) 42
2.3 Design of Experiments 43
2.4 Manufacturing of Double Box Beams 45
2.4.1 Materials 45
2.4.2 Cellular Core Tooling 47
2.4.3 Aluminum Tooling 50
2.5 Processing Evaluation 50
2.6 Mechanical Testing of Composite T-Joints – Approach 53
2.6.1 Digital Image Correlation (DIC) 56
2.7 Discussion of Results 56
2.7.1 Characterization of T-Joints 57
2.7.2 Mechanical Testing of T-Joint Composite Structures 58
2.7.3 Digital Image Correlation in T-Joint Composite Structures 63
2.8 Summary of CCT Composite Characterization 64
Chapter 3: Thermal Modeling of CCT **66**
3.1 Heat Transfer in Composites 66
3.1.1 Heat Transfer Coefficient 68
3.2 Thermal Plate Model 71
3.3 COMRO CCA – Thermal Model 74
3.4 Thermochemical Model – CCT Approach 74
3.4.1 Thermochemical Model – Aluminum Tooling Approach 79
3.5 Experimental Temperature Data 80
3.6 Differential Scanning Calorimetry (DSC) 81
3.7 Discussion of Results 82

3.7.1 Sensitivity Analysis 83

3.7.2 Thermal Model Validation 87

3.7.3 Degree of Cure Validation 95

3.8 Summary of Thermal Modeling 97

Chapter 4: Process-Induced Stress Modeling of CCT 99

4.1 Mathematical Approach to Stress Analysis 99

4.2 COMRO CCA – CCT Stress Model 104

4.2.1 COMRO CCA – Aluminum Stress Model 108

4.3 Experimental Spring-In Approach 109

4.4 Discussion of Results 111

4.4.1 Spring-In Comparison 111

4.4.2 Stress Analysis 116

4.5 Summary of Stress Model 126

Chapter 5: Summary of Key Findings 128

5.1 Joint Characterization 128

5.2 Mechanical Testing 128

5.3 Thermal Model Profile 129

5.4 Stress Analysis 130

5.5 Impact 130

5.6 Future Work 131

5.6.1 Resin Flow Model 131

Works Cited 133

Appendices 136

List of Figures

Figure 1. Schematic of Bagging System for vacuum bagging and autoclave processing

Figure 2. Graph of cure profile, resin degree of cure and viscosity from RAVEN software simulation

Figure 3. Schematic of Bladder Molding Design

Figure 4. Schematic of Cellular Core Technology (CCT)

Figure 5. Demonstration of the CCT process on a wing structure

Figure 6. Schematic of the stages of resin crosslinking

Figure 7. Schematic of spring-in around corner of part

Figure 8. Illustration of pressure variation through plies and resin flow perpendicular and parallel to pressure

Figure 9. Figure of part and predicted spring-in by COMPRO CCA[21]

Figure 10. Examples of subset tracking

Figure 11. Design of experiments matrix for a 2^3 factorial analysis

Figure 12. Image of thermoplastic cellular core with prepreg plies wrapped around

Figure 13. Skin plies added to the cellular cores before closing the mold

Figure 14. Representative double box beam

Figure 15. Example of joint structures and filler noodle calculation

Figure 16. Example of cell gap location in part

Figure 17. Example joint with representative flaws

Figure 18. Image and diagram of T-joint tensile test set-up

Figure 19. Splice lay-up used for 2 and 4 ply double box beams

Figure 20. Image of low quality part

Figure 21. Image of high quality part

Figure 22. Image showing failure mode in cracked part at 1.5 mm extension

Figure 23. Load vs. Extension curve for T-joint samples

Figure 24. Maximum force and average maximum force for each part

Figure 25. Original and Improved Sample 5 (black diamond with error bars)

Figure 26. DIC image showing strain in T-joint tensile test

Figure 27. Image of modeled plate with mesh showing mesh density through thickness

Figure 28. Temperature and degree of cure for FEA model and mathematical model

Figure 29. Image of assembly cross section

Figure 30. Image of assembly and mesh

Figure 31. Image of assembly and mesh for aluminum tooling part

Figure 32. Image of thermocouple locations

Figure 33. Sensitivity analysis of inside HTC – Middle rib

Figure 34. Sensitivity analysis of outside HTC – Bottom Joint

Figure 35. Sensitivity analysis of outside HTC – Middle Rib

Figure 36. Sensitivity analysis of outside HTC – Top Joint

Figure 37. Location of Thermal profile data – Outside aluminum wedge

Figure 38. Graph of thermal profile in model and autoclave – Outside aluminum wedge

Figure 39. Location of Thermal profile data – Bottom composite skin

Figure 40. Graph of thermal profile in model and autoclave – Bottom composite skin

Figure 41. Location of Thermal profile data – Top composite skin

Figure 42. Graph of thermal profile in model and autoclave – Top composite skin

Figure 43. Location of Thermal profile data – Middle composite rib

Figure 44. Graph of thermal profile in model and autoclave – Middle composite rib

Figure 45. Graph of temperature difference between model and experimental data

Figure 46. Graph of modeled degree of cure throughout DBB

Figure 47. Boundary conditions at the end of simulation to allow warpage

Figure 48. Image of locations of spring-in measurement

Figure 49. Image of Precision Coordinate Machine

Figure 50. Sample locations for CMM measurements on rib and skin surfaces

Figure 51. Spring-in angle approach

Figure 52. 3-D plot of CMM measurements taken from experimental samples

Figure 53. Representation of the effect of tool warpage

Figure 54. Curvature measure in sample processed with aluminum tooling

Figure 55. Contact pressure distribution on the middle rib at gel point in both processing methods

Figure 56. Measured thickness variation along middle rib

Figure 57. Image of node locations for closer study

Figure 58. Graph of rib node stress (S33) profiles

Figure 59. Graph of rib node strain (E33) profiles

Figure 60. Contact pressure inside the T-Joint in aluminum tooling

Figure 61. Contact pressure inside the T-Joint in CCT

Figure 62. Contact pressure on the top skin around the noodle

Figure 63. Image of node location for study

Figure 64. Contact pressure observed over cure cycle at node 5401 in both processing methods

List of Tables

Table 1. Comparison of Specific Strength and Modulus in common aerospace materials

Table 2. Required inputs for each model in COMPRO CCA

Table 3. Design matrix of samples made with the variables and combinations studied

Table 4. Design matrix of the samples made for mechanical testing

Table 5. Full design of experiments analysis chart

Table 6. Material Thermal Properties for AS4-3501-6 tape

Table 7. Table of Cure Recipe used in Abaqus COMPRO CCA

Table 8. Compiled degree of cure data to 120˚C of CCT model vs. experimental

Table 9. Compiled degree of cure data to 176 ˚C of Al tooling model vs. panel

Table 10. Compiled Spring-in Data

Table 11. Complimentary Spring-in angles

Dedication

The work presented in this thesis owes a significant amount of gratitude to many individuals without whom this would not have been possible. First, to my advisor Professor Brian D. Flinn for his support and technical advice over the years. To the many members of the Flinn Research Group, thank you for your enthusiasm and encouragement throughout graduate school. To my committee members; Professor Dwayne Arola, Professor K.B. Das, Professor Mark Tuttle, and Geoff Butler, thank you for all of your advice and guidance throughout this work.

To Professor K.B. Das, thank you for always taking the time to give me your advice and wisdom over the years.

Thank you to Bill Rodman of inVision for providing an exciting and novel topic for graduate school. In addition thank you for all of the opportunities you have made available and the advice and encouragement offered over the years.

Much of this work would not have been possible without the technical expertise from Convergent Manufacturing Technologies, specifically Corey Lynam and Nick Cicchine for their knowledge and understanding of the finite element method and composites manufacturing techniques. In addition Geoff Butler of The Boeing Company for his advice on developing the model with COMPRO CCA.

The work performed to create the mathematical model of a plate laminate could not have been accomplished without Professor Lucien Brush, whose understanding of Fortran and discretizing differential equations was invaluable to this work.

Finally, to my family and friends for all of the support and encouragement over the years, without whom this would not have been possible.

Chapter 1: Introduction

This paper outlines efforts made to understand and apply Cellular Core Technology (CCT) to aerospace structures. The motivation behind this work will be introduced along with a review of information relating to processing, mechanical testing, and modeling of composites. Processing of composites using CCT will be discussed. Process modeling will be applied to CCT as a tool to understand and optimize manufacturing with CCT. Efforts to and validate the modeling work will be reviewed and comparisons made to traditional methods of manufacturing.

1.1 Motivation

Fiber reinforced composite materials have become highly desirable for a variety of applications because of their high performance capabilities. Aerospace has increasingly looked to composite materials because of their light weight, high strength, high stiffness, and resistance to fatigue. This combination of properties makes these materials ideal for the demanding requirements in aerospace.

Despite the many advantages of carbon fiber composites, several challenges still remain. The structure of composite materials necessitates different manufacturing methods. A variety of manufacturing methods are available depending on the materials, shape, and quality of the required part. Composite materials have the potential to develop large continuous, complex structures easily through the lay-up process. This approach maximizes the benefits of continuous fibers and reduces weight of the structure. New manufacturing methods now exist with the capability to develop complex structures but little has been done to optimize these structures. It is

this area that the incorporation of modeling may prove powerful in helping to predict and improve part dimensionality prior to building large, expensive prototypes.

1.2 Project Scope

This project focuses on the use of cellular cores for manufacturing complex shapes in aerospace structures. The technology is studied in the context of evaluating its capabilities, advantages, and limitations in developing high quality structures. A comprehensive understanding of the process is given based on the data collected, identifying key parameters and their relative effect on the performance. It is expected that this knowledge will help optimize the process and lead to applications in aerospace which could benefit from lighter, structurally efficient components. In addition to developing a knowledge base for this process, this project focuses on building a model of the cellular core technology to provide more knowledge about a final product before manufacturing. Prototype development can be an expensive stage in production, increasing exponentially with part size and complexity. A challenge when developing complex, integrated structures is the expensive prototypes necessary to validate the structure. Tooling alone can have significant expenses; the ability to minimize redesigns of tooling components could have significant long term savings. A robust model designed specifically for the cellular core process would enhance the prototype development and streamline improvements before large investments are made. A model has the capability to predict key pieces of information about the final part including heating rate (lead/lag zones), degree of cure, internal stress and potential deformation. From this a structure design can be optimized and only developed after rigorous testing has proven the resulting structure will have high quality. While modeling of composites

has been performed in the past, this project will look to take this existing knowledge and apply it to this new manufacturing method capable of building more complex parts and develop a model designed specifically for building large, complex components with a high degree of accuracy.

In the following sections previous literature will be presented on topics related to the current research. Work done previously on modeling of composites will be discussed; this knowledge has been used to help build the work currently being done to develop a model for complex shapes. Complimentary to this, previous work regarding mechanical testing of complex structures (T-joints) is discussed. Background will be presented on relevant modeling knowledge and testing of T-joints.

1.3 Project Goal

The goal of this work is to identify what challenges remain in building complex structures and demonstrate that cellular core technology has the capability to create these structures optimizing the manufacturing process. The primary objective of this project has been to design a model for the curing of composite structures using cellular core technology. Once the feasibility of developing this model has been demonstrated a second model using aluminum tooling will have been developed for comparison. Using these two models, key differences in how these processing methods interact with a part have been identified and correlated to the final structures. This can be used as a resource to help understand the capabilities and limitations of manufacturing with this novel tooling method. From this a knowledge base can be established regarding the modeling and manufacturing of complex structures using cellular core tooling.

1.4 Document Organization

This document is organized into chapters covering the processing, testing, and modeling of composite structures using CCT. The current chapter focuses on the motivation behind this project and introduces necessary background information. Chapter 2 covers a review of mechanical testing of composite T-joints and the approach taken in this work to optimize, design and test composite T-joints made with CCT. Chapter 3 focuses on the thermal model developed to simulate processing with CCT, including background, model design, validation, and testing performed. Chapter 4 covers the background, model approach, and discussion of results for the stress model developed. Finally, chapter 5 summarizes the work done and the conclusions made.

1.5 Carbon Fiber Reinforced Polymer Composites

Carbon fiber reinforced polymer (CFRP) composites are used most extensively in aerospace for their high specific strength and specific modulus. The specific strength and modulus scale the strength and modulus by the density of the material. These values more accurately convey the efficiency that carbon fiber has as a structural material where weight savings is critical. Table 1 below displays typical values for specific strength and specific modulus for materials used in aerospace[1]. Where σ is the materials strength, ρ is the materials density, and E is the materials elastic modulus.

Eq. 1 and 2 $$Specific\ Strength = \frac{\sigma}{\rho} \qquad Specific\ Modulus = \frac{E}{\rho}$$

Table 1. Comparison of Specific Strength and Modulus in common aerospace materials

Material	Tensile Modulus (E, GPa)	Tensile Strength (σ, GPa)	Density (ρ, g/cm^3)	Specific Modulus	Specific Strength
Steel	210.0	.34-2.1	7.8	26.9	.043-.27
Aluminum	70.0	.14-.62	2.7	25.9	.052-.23
Glass Fibers	85.5	4.6	2.48	34.5	1.85
Graphite Fibers	390.0	2.1	1.9	205.0	1.1
Graphite Fibers	240.0	2.5	1.9	126.0	1.3
Carbon Composite (Uni)	83.0 (.58 V_f)	.38 (.58 V_f)	1.54	53.5	.24

Typically an epoxy based matrix is used with carbon fiber to create the composite material, in some situations a bismaleimide (BMI) resin is used for high temperature applications[2]. The matrix material is important to understand not only for mechanical properties but also for processing purposes which will be discussed in depth later. There are many ways to combine fibers and resin but aerospace generally uses resin that has been "pre-impregnated" with fibers or "prepreg"[1]. Prepreg is desirable for its high volume fraction of fibers and therefore high mechanical properties. It comes in the form of plies with continuous fibers either in one direction (unidirectional tape) or a variety of weave patterns. These plies can be stacked to create a laminate tailored to a specific application by favoring specific directions when placing fibers, creating a laminate that is highly optimized for a specific application. This versatility is another advantage of composite materials and makes them highly efficient at carrying loads.

The epoxy used in prepreg materials are thermoset polymers which cure at elevated temperatures. The epoxy undergoes an irreversible chemical reaction whereby crosslinking occurs between the polymer chains[1, 3]. The crosslinking is an exothermic reaction, releasing energy as bonds are formed. Using Differential Scanning Calorimetry (DSC) the heat given off can be measured to determine the percentage of crosslinking or degree of cure. As the reaction

takes place the degree of cure approaches 100%, generally a value above 90% is considered fully cured. During heating, the viscosity of the epoxy drops and the epoxy becomes more "runny." As the crosslinking occurs the viscosity increases until the epoxy becomes rigid. In addition to the viscosity increasing until the epoxy is cured, there is a small decrease in volume or shrinking as the resin crosslinks due to the density increase when crosslinking occurs. The cure kinetics of the epoxy will be important when understanding the role of the epoxy in modeling.

1.6 Processing Techniques for Fiber Reinforced Polymer Composites

There are a large variety of processing methods for composites, every one dictated by factors such as geometry, application, and cost. There is a range of qualities observed in these methods, and each one has unique advantages, limitations, and challenges. With fiber composites there is a strong correlation between mechanical properties and processing technique. Some high performance applications require high processing quality regardless of cost while other may care more about keeping production under a certain value. In addition there is also trade-offs between manufacturing individual components or large structures. With increased shape/size/complexity there is typically a significant cost increase. This section discusses some of the common processing methods found in the composites industry including vacuum bagging, autoclave processing, and bladder molding.

1.6.1 Vacuum Bagging

One of the most common manufacturing methods is vacuum bagging. This method is generally used either in tandem with oven curing or autoclave processing. The approach revolves around

bagging of a composite part against a tooled surface to help maintain the part shape as curing takes place. A vacuum bag seals the part to the tool and restricts the shape of the part, at elevated temperature the resin will run and if the part is not confined it will lose its shape. The bagging process controls the inherent part quality, porosity and resin rich areas can be mitigated by proper bagging lay-up. A schematic of a traditional bagging design is shown in figure 1 below for reference.

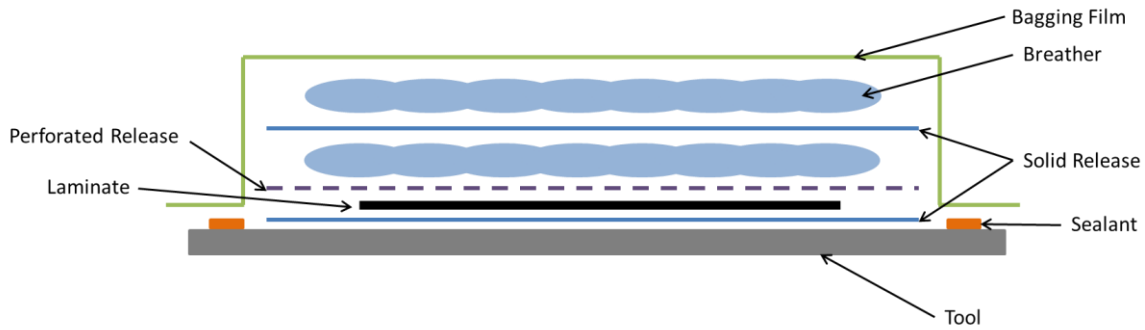

Figure 1. Schematic of Bagging System for vacuum bagging and autoclave processing

This approach uses a cloth as “bleeder” to collect excess resin that is removed during cure. The release films keep the epoxy from curing to the bleeder or the tool. Depending on whether this process is used with an oven or autoclave can greatly affect the cost. Often this method is included in many processing methods as a means to control the shape the part by bagging it against a tool.

1.6.2 Autoclave Processing

Autoclave processing is the leading method of manufacturing primary structure in the aerospace industry. The high quality of the parts produced makes this an attractive method for meeting the

high performance demands seen in aerospace structures. The autoclave provides pressure and heat to consolidate and cure the epoxy. The curing of epoxy requires a specific cure cycle to lower resin viscosity and promote resin flow. The epoxy must be allowed sufficient time at lower viscosity to flow and consolidate, a graph of temperature, degree of cure, cure rate, and resin viscosity is shown in figure 2 below demonstrating the dynamic relationship observed.

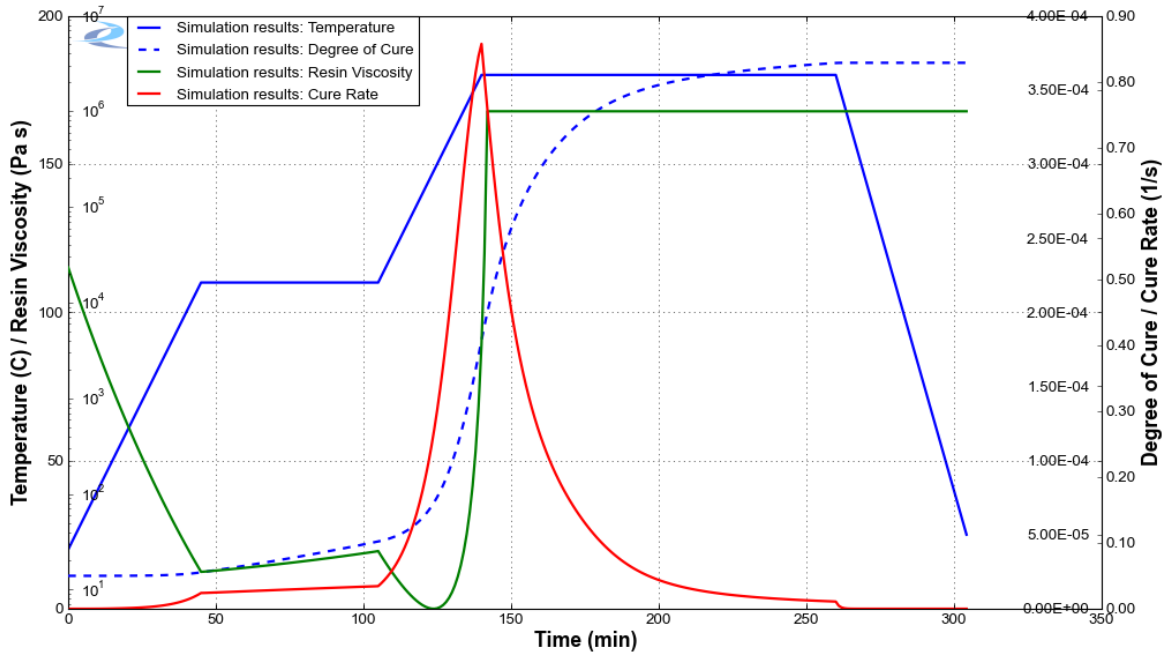

Figure 2. Graph of cure profile, resin degree of cure and viscosity from RAVEN software simulation

The temperature ramp rate is highly controlled, if the temperature increases too quickly the resin will not have enough time at a lower viscosity and gel too early, allowing inadequate time for resin flow. In addition, if the temperature ramps too quickly the autoclave may overshoot the desired hold temp increasing internal stress by curing at a higher than desired temperature. If the rate is too slow the resin will never reach a low enough viscosity to flow and gelation will

occur[4]. A rate that allows the epoxy to heat up quickly enough to achieve the lowest possible viscosity, while not heating up so quickly as to begin crosslinking prematurely is desired for ideal resin flow. This balance is necessary for a high quality part and a priority when designing a new processing method. The required ramp rate must be achievable and the temperature cannot vary too drastically within a part or residual stress will form and weaken the structure. Ultimately a degree of cure higher than 90% is ideal for a composite part.

The pressure applied through the autoclave acts to compact the plies forming a solid laminate. The low resin viscosity and high pressure consolidate the plies by removing excess resin and air from the material. Air or gas can be left behind as voids in the resin which lower the overall part strength by contributing to the defect quantity. Voids act as stress concentrations forming weak spots in the structure, typically under 3% porosity is required for industry certified composite structures[5].

1.6.3 Bladder Molding

An alternate processing method commonly used is bladder molding, which uses an inflatable bladder to cure plies against a clamshell mold. Prepreg plies are applied up against the mold and enclosed with the bladder. Positive pressure is applied inside the bladder to consolidate the plies while they cure. This method has several advantages over traditional bagging methods; the bag allows for more complex shapes and features co-cured together. While advantageous for certain geometries, there are also limitations to this approach; the geometries are limited as laying plies

directly on the bladder is difficult and the bladders can be susceptible to leaks which ruin the part. A schematic of the bladder molding design is shown below in figure 3[6].

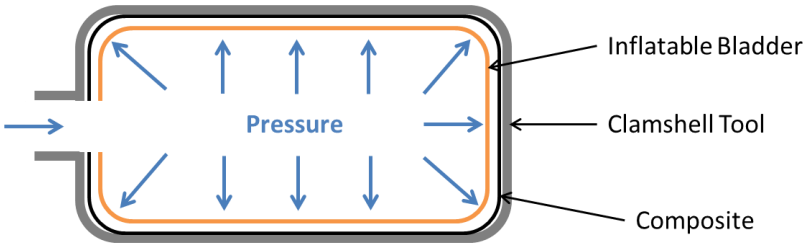

Figure 3. Schematic of Bladder Molding Design

1.7 Cellular Core Technology (CCT)

Traditionally composite parts are made in simple geometries and assembled after curing. Manufacturing of complex and unique shapes can be challenging to design for a variety of shapes without the costs increasing exponentially. Because of this parts are bolted or bonded together, and sometimes both[7,8]. Parts that are fastened together require drilling holes, but this creates complications for composite materials. Generally parts that are assembled after cure must be thicker and stronger to account for the disjointed structure, stress around holes in composites are generally higher than those in metals making them susceptible to premature failure[9-12]. Bonding is regarded as a more ideal joining method because of the lack of holes, and the more seamless stress transfer between parts. In practice however, verifying bond strength is a challenge that is still proving difficult. There is still no way to determine bond strength without actually testing and breaking the bond. Non-destructive Inspection (NDI) techniques can be used to verify that the surfaces are in contact, but beyond that whether a bond has the potential to hold 100% of the required load or 10% is difficult to determine. However co-cured parts can more

efficiently transfer stress throughout a part without the worry of bonds “unzipping” or stress around holes exceeding the allowable range[8].

Recent advances have developed new approaches to manufacturing composite structures that allow greater diversity of design. InVision Technologies LLC has developed a new processing method using thermoplastic bottles to create complex parts. The method uses a combination of autoclave and bladder molding concepts to create high quality, low defect parts with high complexity. The ability to create complex shapes removes manufacturing design limitations allowing creation of highly optimized structures[13]. The process uses thermoplastic cellular cores as semi-rigid tooling, these hollow cores are used as internal tooling with composite plies layered around them. Then these parts are placed in a metal clamshell mold to provide a rigid surface for the plies to cure against. The thermoplastic cores are connected to autoclave pressure, at elevated temperature the cores soften and the pressure compacts the plies against adjacent cores or the outer tooling. The semi-rigid nature of the tooling allows plies to be placed directly on them and each core to be assembled together. During cure the part is evenly consolidated throughout the part by the bottles and internal features such as ribs connecting skins can be co-cured into the structure as shown in figure 4.

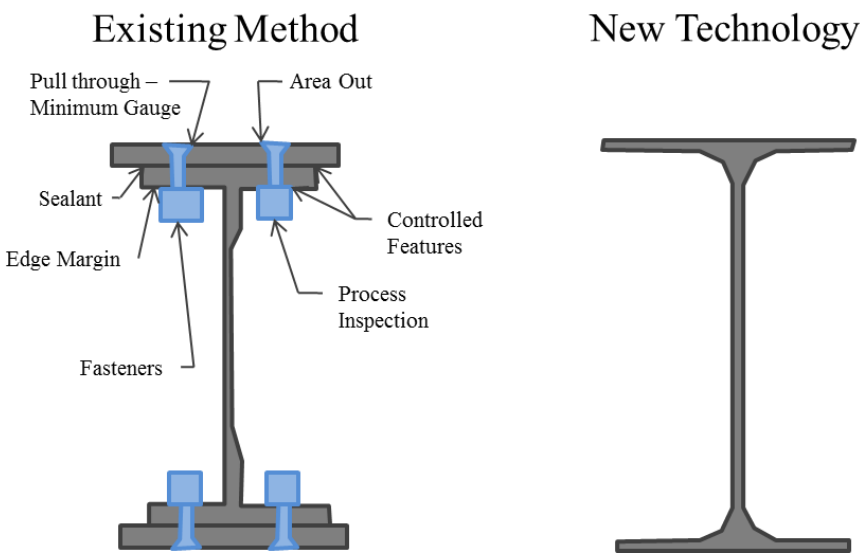

Figure 4. Schematic of Cellular Core Technology (CCT)

This creates a highly optimized design free of disjointed parts and fasteners. In addition the process allows dimensional control over the part and internal features necessary to meet aerospace tolerances. The advantage of this process over similar methods already in use (bladder molding) is the ability to create internal features such as rib stiffeners and complex tooling can be cost-effectively manufactured into any shape desirable. Figure 5 below demonstrates how a part is made with the CCT process highlighting the ability to co-cure the structure.

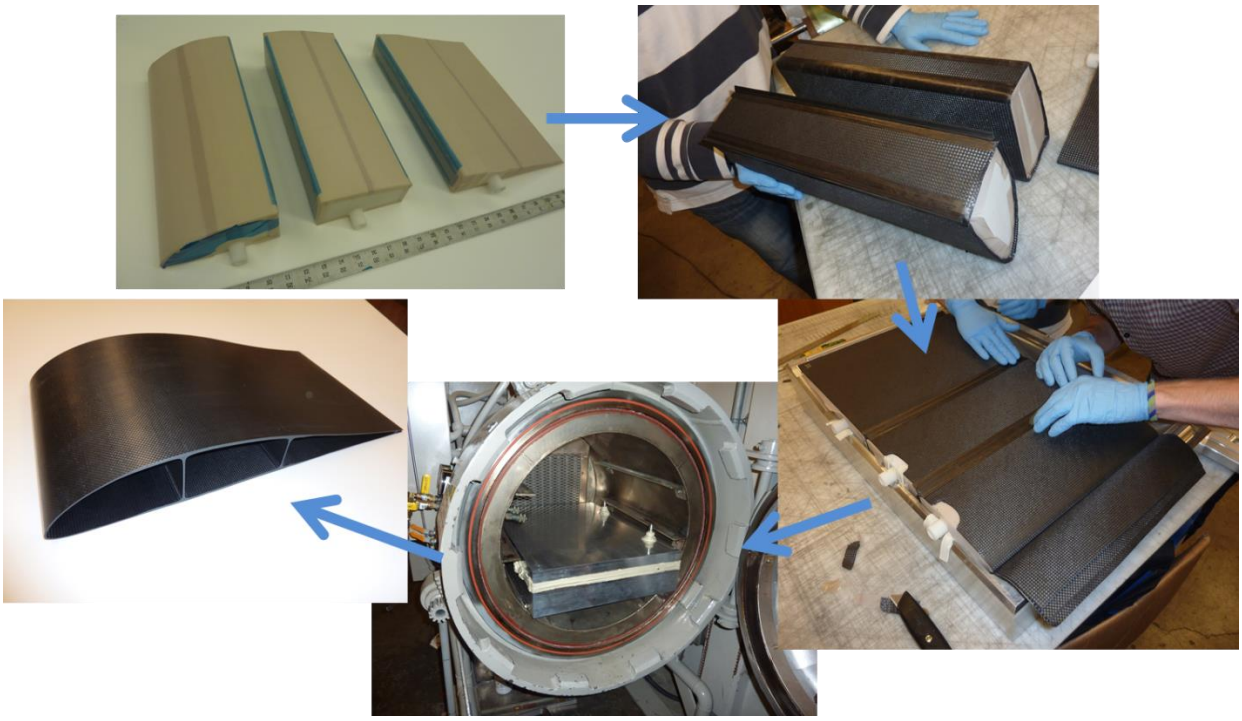

Figure 5. Demonstration of the CCT process on a wing structure

1.8 Residual Stress Development in Fiber Reinforced Polymer Composites

Process-induced part warpage is always a concern when manufacturing composite structures; residual stress is usually the cause of any deformation that occurs. These concerns become greater when the part is thicker or the geometry is complex. There are several ways that residual stress can develop within a part; most often temperature gradients, degree of cure, degree of cure gradients, resin cure shrinkage, and tool-part interactions will be the cause of any internal stress[14-17].

First a more detailed concept of resin cure kinetics must be established to understand how residual stress can develop. There are three stages to the curing of a thermoset (shown below in

figure 6); Stage 1 where the resin is completely viscous (image 1), stage 2 where the resin exhibits viscoelastic properties (image 2 and 3), and stage 3 or the completely elastic region (image 4). At this point the material is rigid and the covalent bonds formed during crosslinking are permanent thus the key to a thermoset polymer[18, 19]. As the degree of cure increases so does the modulus of the resin. As crosslinking begins, the rate is dependent on the formation of covalent bonds, but as gelation occurs the rate controlling parameter switches to diffusion of polymers through the developing macromolecular network.

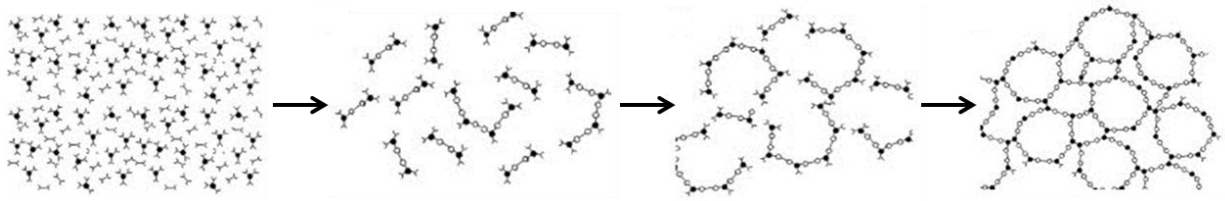

Figure 6. Schematic of the stages of resin crosslinking

Gelation occurs at approximately 45% to 50% crosslinking at which point there is a sharp increase in the modulus. This trend is inversely proportional to the change in volume which decreases as crosslinking occurs and the density increases[18, 19]. Shown in earlier in figure 2 the cure rate spikes and then drops drastically due to the changing rate controlling mechanism.

Anisotropy of fiber composites causes the volume shrinkage to be asymmetric. The fibers restrict shrinking of the resin in the longitudinal direction, creating microscopic strain at the fiber and matrix interface. In the transverse direction the strain is unrestricted and shrinking occurs. In a laminate this creates varying degrees of strain within the stack. Deformation from this strain is corrected for by designing symmetric laminates to balance opposing strains. When the shape

becomes more complex than a flat panel the strain becomes more complicated. In an L-shaped part the combined effects of the anisotropy in the composite, the thermal mismatch between the tool and part, and the shrinkage in the resin can cause warpage known as spring back. The low longitudinal strain combined with the high radial strain at the corner cause the angle to spring in deforming the part potentially weakening it or taking it out of tolerance[18]. This phenomenon is show in figure 7.

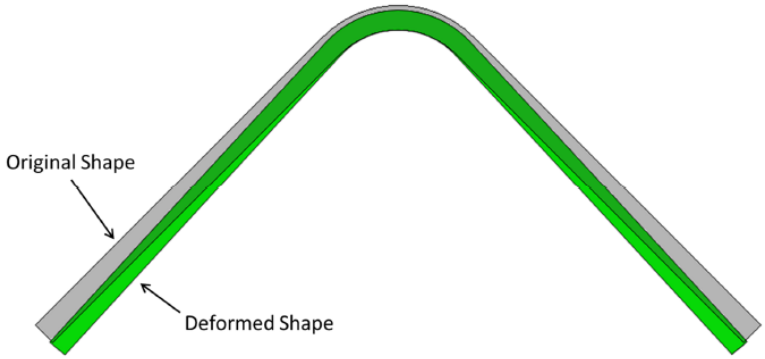

Figure 7. Schematic of spring-in around corner of part

In addition to resin shrinkage during cure, thermal strains can arise if the part is heated non-uniformly. If the temperature varies within a part, the cure rate may differ and some areas may cure before others leading to local resin shrinkage. Because of the variable resin modulus in a part curing non-uniformly, resin shrinkage becomes locked in and creates internal stress as the cure propagates. This strain leads to further deformation. The likelihood of this affecting a part increases with the complexity. Metal and any internal tooling will slow heat to inner features and could create a thermal lag zone in the part.

The tool-part interaction plays a strong role in the final magnitude of stress developed during cure. Metallic tooling is beneficial because of its hard, smooth surface to cure against. However, many metals have a high coefficient of thermal expansion and during cure they will heat quickly and expand imposing constraints on the composite. The tooling puts shear and normal stresses on the part during the expansion and contraction. The forces during expansion cause little permanent strain as the epoxy is still pliable, but during cooling the resin has cured and the composite is rigid. At this point shear stress is put on the tool side of the part, while the far side can relax more readily. Because the part cures in a state with strain applied by the tool, residual stress develops and results in deformation once the tool is removed. In addition to the above mentioned factors the final stress of the part is affected by the resin, fiber type, weave pattern, ply number (thickness), and part geometry, making the results highly specific for each case[18]. Because of the large number of variables that can contribute to stress and deformation, it can be very difficult to predict the final shape of a part. A model that fully encompasses these ideas will help improve accuracy of deformation prior to building structures. This becomes more valuable as the part complexity increases and each part becomes more costly and time consuming to make.

1.9 Finite Element Analysis (FEA)

Finite Element Analysis (FEA) has been used extensively for predicting system response and end states. The finite element method simplifies a structure by breaking it into a series of elements connected at nodes. These discretized elements and nodes approximating a structure make up a mesh. The elements mimic material properties allowing the user to solve complex engineering problem by approximating a complex structure. Loads and boundary conditions can be placed on

the mesh and the response calculated. There are a wide variety of problems that can be solved this way including but not limited to stress, heat, dynamics and fluids[20]. The power to predict loadings can be advantageous for engineering applications, reducing the number of experimental samples, and creating a strong understanding of the key variables. However, the accuracy of this method is dependent on the user, and must be supported by experimental results, otherwise the solution is meaningless. Without confirmation the answers generated have no grounds for accuracy[20, 21]. As a complimentary method FEA is incredibly useful for solving complex problems and provide support for experimental results. An example of the use of FEA can be seen in the building block test scheme, whereby bigger and bigger samples of a structure are tested as they are optimized. This saves time and money during sample generation, so that large prototypes have only been created once the components have been optimized. If FEA is done in tandem with testing throughout the process, any data obtained from the simulations of the components can be used as input to help predict how the full structure will perform prior to final testing. In aerospace where the final part can be something as large as a wing, there may very few tests for a given situation because the structure is so large and complex. FEA provides a wealth of information that would not have been available otherwise when testing is limited because of cost.

1.10 Process Modeling

The ability to tailor part design to specific applications is incredibly powerful with respect to structure optimization. Parts can be made efficiently in terms of load carrying and weight. As structures become more application specific, prototype design and testing becomes more

challenging as each structure is unique in shape, size, thickness, number of tools, etc. The cost of several iterations of a prototype can add up very quickly. An accurate and robust model for manufacturing complex structures can help streamline manufacturing design. The ability to predict residual stress and deformation greatly improves a manufacturer's ability to make successful, high quality parts and decreases the number of parts scrapped for manufacturing defects. Modeling can be a powerful engineering tool but requires a strong understanding of the governing laws to implement successfully. At its core a model is a mathematical tool which uses physical laws to represent a system. There are several key components which are generally included when developing any type of model which include: *model boundaries*, *physical laws*, *constitutive laws*, *boundary conditions*, *assumptions*, and *experimental validation*[20]. By applying this method to the curing of composite parts, a model can be developed to simulate the chemical behavior and physical response of the composite. In the past this approach has been divided into sub-models capable of handling certain aspects of the cure, specifically thermal analysis, resin flow kinetics, and stress analysis.

1.10.1 COMPRO Common Component Architecture (CCA)

Convergent Manufacturing Technologies has developed a plug-in tool for the FEA software Abaqus which has the ability to model curing of composite parts. The software uses an integrated sub-model approach to break the complex task into simpler models and solve for a solution[22]. The three sub-models are the thermochemical, flow, and stress model. The thermochemical model handles the temperature profile and the heat generation through the part, including tooling and bagging material. The flow model maps the viscosity of the resin and predicts resin flow

paths. And finally the stress model predicts any residual stress development and part warpage. The combination of these models can produce an accurate simulation for the curing of composite parts. This study has focused on the thermochemical model and the stress model assuming the resin flow to be negligible in the self-contained tooling. The essential modules included within each of these simulations were the part, property, assembly, step, interaction, load, mesh, and job modules. The approach for each will be covered briefly below.

The part module is used to render the 3D drawings of a part or parts of interest. Drawing and dimensioning or importing the required part is the preferred method for developing a model. Once all of the pieces have been constructed the property module is used to give each component material properties. ~~F~~or each component of the model different material properties are required to encompass the necessary scope. Shown below are the variables necessary for each step in the model[22]

Table 2. Required inputs for each model in COMPRO CCA

Thermal Module	Density of the composite Density of the resin Specific heat capacity Thermal conductivity Resin heat generation Resin degree of cure Resin heat of reaction
Resin Flow Module	Fluid pressure Fluid Viscosity Permeability of the solid porous structure Effective stress tensor of the solid porous structure
Stress Module	Internal work Work done by external forces Strain tensor Stress tensor Free thermal strain tensor Initial stress tensor Displacement vector Body forces Surface forces

The parts can then be assembled in the assembly module. During the assembly module an instance of each part is created and the position on each part instance is defined. Either independent or dependent instances can be chosen; a dependent instance will update as any changes are made to the original part without needing to redefine the location relative to other part instances, while an independent instance will not automatically update.

The step module is used to define and organize the actions taking place on the part. This allows loads, interactions and boundary conditions to be tailored to each step created. In all models an

initial step is used to define initial boundary conditions and any predefined fields such as starting a temperature. In any steps after this loads are activated and boundary conditions are applied. Once the required steps are defined, relevant interactions are declared in the interaction module. Boundary conditions are defined here; symmetry can be applied for model efficiency and interaction between different materials at surfaces. Tie conditions are generally used between adjacent surfaces for heat transfer problems. In some cases surface interactions that include a friction component are used in stress problems. The load module is then used to define what action is placed on the part, for this work temperature loads and pressure loads are applied during the virtual autoclave cycle. The thermal module of the study only requires a temperature profile to follow.

The mesh module defines how the nodes and elements that make up the mesh are assembled. The design of the mesh will dictate how accurate and efficient the model solution is. In order to create a high quality mesh, the part is broken into substructures by a process known as partitioning. This creates simple blocks for the mesh to build with. Ideally structures should be broken down into small cubes as a mesh can easily be generated from those, but this is not always possible. In regard to this work, the tooling and part were partitioned into the smallest components possible, more effort is necessary when building the mesh of composite structures due to their complexity and especially when that is the primary area of focus.

The final module of interest is the job module, used to set up the simulation. Here a model run was defined which uses the part assembly, steps, boundary conditions, and loads to run the

model. From this an output database report is created with the time, temperature, position, and cure data for each node which can be accessed for analysis.

1.10.2 Raven Simulation Software

In addition to the COMPRO CCA developed by Convergent Manufacturing Technologies, a simplified version of this software is also available for use[22]. The Raven Simulation Software developed by Convergent handles basic simulations in 0, 1, or 2 dimensions. This software is another tool available for understanding a material response to heat. Using experimentally generated data files a temperature profile can be designated and resin cure kinetics data can be obtained. Information from degree of cure, resin viscosity, glass transition temperature and resin modulus can all be collected. While not as robust a methods such as COMPRO CCA, Raven can provide quick answers to processing related questions.

1.11 Literature Review of Process Modeling in Composites

Work has been done previously in the field of modeling composite part processing. A review of literature shows studies performed exclusively on flat panels or simple shapes. In this section previous work in this field will be discussed.

1.11.1 Modeling of Flat Plate Laminates

Initially Loos and Springer studied the curing of epoxy resins and their role in the processing of composite parts[17]. Using a thermochemical model, a flow model, and stress model, they were able to predict the temperature, resin distribution, degree of cure, void sizes, and residual stress all relative to position and time in a flat panel. Loos and Springer used the law of conservation of energy and resin cure kinetics to create an expression for heat transfer in a composite shown in equation 3.

Eq. 3 $$\frac{\partial}{\partial t}\left(\rho C_p T\right) = \frac{\partial}{\partial z}\left(k\frac{\partial T}{\partial z}\right) + \dot{Q}$$

In this equation ρ represents density, C_P represents specific heat, k is the thermal conductivity, and $\dot{Q}$ is the rate of heat generation from the chemical reaction. Using this expression they were able to approximate the heat evolved at a given time step and knowing the total heat of reaction H_R, were able to calculate degree of cure, α. A resin flow model was developed to account for pressure in the composite, including resin flow both parallel and perpendicular to the applied pressure. Resin viscosity was determined based on the relationship between viscosity and degree of cure using experimental data[17]. Using the law of conservation of mass and Darcy's Law, Loos and Springer formulated an expression for the resin flow normal and parallel to the laminate.

Eq. 4 $$\frac{\partial M}{\partial t} = -\rho_r A_z V_z = -\rho_r A_z S_c \frac{P_c - P_u}{\int_0^{h_c} \mu dz}$$

This equation represents the resin mass flow out of the composite, where ρ_r is the density of the resin, A_z is the cross-sectional area, V_z is the velocity of the resin, h_c is the compacted plies thickness, P_u is the pressure at the interface, P_c is the pressure at location h_c in the composite, and . An assumption is made that resin flow perpendicular to the applied pressure (in-plane with laminate) is constrained to only along the direction of fibers in each ply. This assumption is justified by the argument that greater resistance exists if the resin tries to flow perpendicular to the fibers. A schematic of this approach is shown below in figure 8, Loos and Springer defined two regions through the thickness of the laminate; Region I and Region II. Region I is characterized as the plies that are situated closer to the side with pressure and consist of consolidated plies with no excess resin. While Region II consists of unconsolidated plies with excess resin and as cure progresses Region I grows through the thickness.

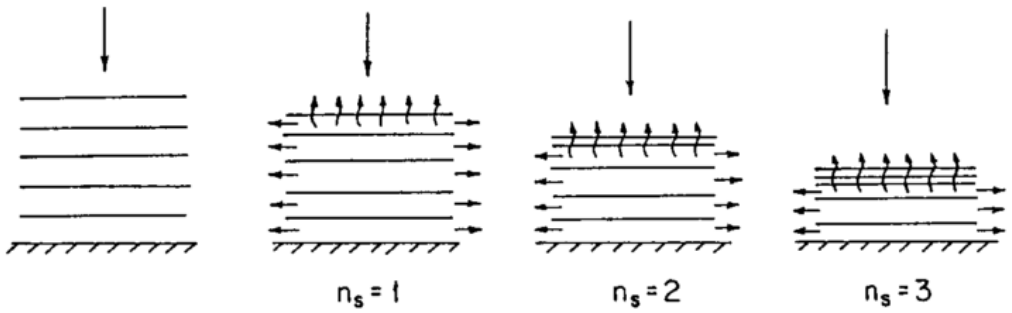

Figure 8. Illustration of pressure variation through plies and resin flow perpendicular and parallel to pressure

The stress analysis becomes straightforward, based on the Q matrix of the laminate and the strains imposed by the temperature difference and position in the laminate. These expressions are given below in equation 5 and 6.

Eq. 5 $$e_j = \alpha_j(T - T_a)$$

Eq. 6 $$\sigma_i = Q_{ij}(e_{oj} - e_j)$$

Where α is the thermal expansion coefficient used to determine the strain in a given ply (e_j). Loos and Springer were able to use these concepts to build a program that could generate the temperature profile, degree of cure, resin viscosity, and residual stress in the laminate all with respect to position and time[17].

This approach has been duplicated in other studies and material systems and even some simple shapes[16, 19, 23]. Bogetti and Gillespie performed a similar study on thick-section thermoset composite laminates[19]. Using a one dimensional cure simulation combined with laminate plate theory they were able to study the relationship between heating profile, degree of cure, and stress development in parts of significant thickness where the thermal gradient is not negligible. This study is covered in detail in chapters 3 and 4 with the thermal model and stress model.

1.11.2 Modeling of Angled Laminates

The most complex structures found in published works that model composites processing were performed by Fernlund on L and C-Channel structures[14]. This paper examined the effect processing conditions can have on spring-in of angles laminates. The study examined cure cycle, tool-part interaction, geometry, and the lay-up on deformation in composites. The study uses the COMPRO CCA program to model the cure, this work also the first reference to process

modeling of composites with FEA. The model incorporates both tooling and angled parts which undergo a cure and in the end step a "tool removal" stage is added which allows the cured laminate to deform. They found that due to geometric locking of the tool and part together in the C-channel, the spring-in was approximately 30% higher than in the L-shaped parts[14]. They also found the spring in to vary significantly based on tool surface, material, and cure cycle (one stage vs. two stage cure). Fernlund was able to get good correlation between the models and the experimental data, validating the use of COMPRO as a predictive tool in composites processing[14].

Fernlund and Floyd published another paper on L-shaped composite parts in an attempt to predict spring in and develop tooling to compensate for it[23]. Fernlund and Floyd used COMPRO CCA to predict part deformation due to residual stress from tool growth, spring-in, tool-part interaction, and cure gradients. Using the predicted deformation a tool was designed deformation mapped using a coordinate measuring machine (CMM). Figure 9 shows the studied part and the spring-in observed.

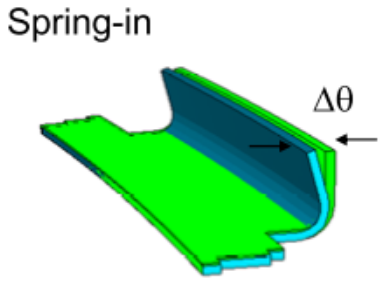

Figure 9. Figure of part and predicted spring-in by COMPRO CCA[21]

The results showed good correlation between the model and the experimental samples indicating again the advantages of predictive modeling in tool design.

Process modeling has been shown to be a powerful tool in composites manufacturing, providing a wealth of data regarding a part before attempted builds. The math has proven valuable in predicting process states on flat panels and now that FEA has been incorporated it is significantly easier to apply these techniques to more complex parts. Simple geometries have been studied showing good correlation between the model and experimental data. This project will look to provide new information on this subject by applying these techniques to a processing method with the capability of manufacturing complex structures.

Chapter 2: Characterization of Composite Structures Processed with CCT

This chapter covers the manufacturing and characterization of composite structures made with CCT. Work will be presented on the optimization of processing using cross sectional images and mechanical testing. Background on processing defects and mechanical testing of composites is discussed with respect to T-Joints.

2.1 Processing Defects in Composites

There are several defects that can arise from poor composite processing. Typical issues include porosity, fiber wrinkling, and resin starvation. Void content in composites is a constant concern during processing, typically porosity can developed from trapped air or moisture during cure[5]. Ply wrinkling can occur in areas of poor consolidation when fibers are allowed too much movement and bending. All of these issues can be mitigated by proper consolidation of the plies forming a solid laminate. Consolidation is attributed to several factors including geometry, tooling, cure cycle, and pressure. Part geometry and tooling can influence resin flow patterns and pressure variations creating areas of high or low resin content with a part. Given the rule of mixtures variations in resin content can influence the final part strength and stiffness. Together the cure cycle and pressure will interact to dictate resin viscosity and formation of voids. As discussed earlier, higher pressures have been shown to minimize void content and an appropriate cure cycle will give the resin adequate time at a low enough viscosity to allow the pressure to consolidate plies[5].

Detection of processing defects can be challenging given the variations in size and location within a part. Some methods for detection include non-destructive inspection (NDI) using ultrasonic inspection techniques. Other methods use destructive testing either by cross-sectional imaging or mechanical testing designed to test matrix dominated properties. Short beam shear testing, flexural testing, or compression testing can be indicative of void content and the effect of mechanical properties[5].

2.2 Mechanical Properties of Composite T-Joints

Structure validation can be performed in a variety of ways, mechanical testing is commonly used when qualifying new manufacturing methods. With the newly complex geometries capable with the CCT finding ways to compare these to existing structures is a challenge. Internal ribs that are co-cured into a structure are the cornerstone of what makes the integrated structures an innovative technology. The T-joints connecting these ribs are the base component of what makes these structures possible and where mechanical testing will be focused. There is currently enough literature already available on the testing of the T-joint geometry to establish criteria for testing parameters[24-26].

The simplest test which can be performed on a T-joint is the tension test. This test is a powerful tool for comparing ply adhesion and consolidation. The geometry causes the in-plane loads created by tension on the rib to result in out of plane peeling where the rib meets the skin plies at the joint[24]. The various designs of these joints have been attempted using secondary bonding methods or other stitching techniques[24, 26]. T-joints have been made using intermediate layers between the rib and skin using co-bonding to secure the parts together. I-beams have been used

as ribs and bonded to the skins and in some cases fastened as well. It is common practice to include these fasteners to avoid "unzipping" of the bond. Failure in these joints typically occurs at the innermost plies against a filler noodle at 45 degrees to the load direction halfway between the rib and skin. The filler noodle fibers are along the length of the joint making them transverse to the load path and causing failure at the interface between the plies of the rib and the filler matrix[24, 25]. Because fracture is directed into the interface of the plies and filler this test can be a powerful tool for measuring consolidation at joints. It is a matrix dominated test which means porosity will have a greater influence on the strength than a test purely in plane with fibers.

2.2.1 Digital Image Correlation (DIC)

To improve the information obtained from mechanical testing, Digital Image Correlation (DIC) can be performed. DIC is a full-field measurement technique for imaging samples during mechanical testing which captures sample displacement. Using cameras to track relative sample movement the full-field strain map can be computed. The method uses features on the surface to track distortion and local strain. Generally to obtain a full map of the displacement, a random speckle pattern is created on the surface, generally white with black speckles. This speckle pattern is broken down into smaller grids called subsets which have a unique image within them that allows the camera to track their movement[26-28]. These subsets are each tracked and from the subset displacement vectors are created which build the strain map, this is shown in figure 10 below which demonstrates the change in subset location and shape during testing.

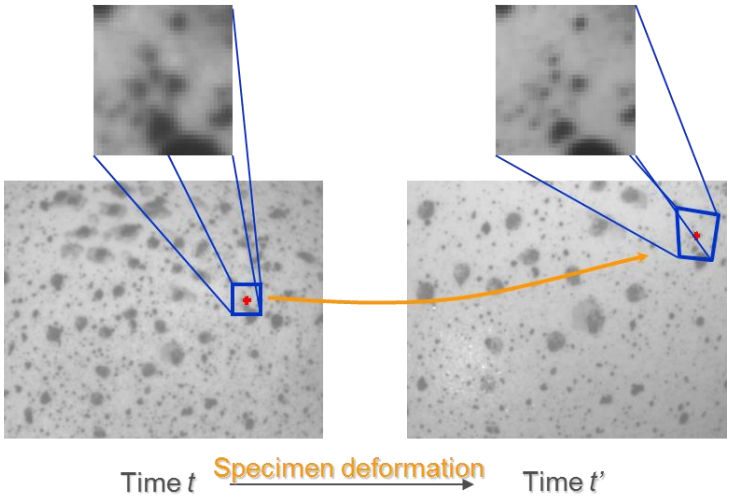

Figure 10. Examples of subset tracking

This method is highly accurate over a large range of sizes and scales. It offers the ability to find local strains at a point or along a line, with focus on any of the principal strains, x-direction strains, y-direction strains, major or minor strain directions. For samples with high stiffness and low strain as is the case with carbon fiber composites, it can be advantageous for sample analysis to go back and determine where strain concentrations are highest and how the stress moves through the part which may not be possible visually. In addition this test method is non-contact so samples can be taken to failure, which in the case of carbon composites is beneficial due to their sudden and catastrophic failures.

2.3 Design of Experiments

A common strategy for approaching experiments with a large number of variables is a Design of Experiments (DOE), using the fewest possible variety of samples and maximizing the amount of valuable information obtained. The 2^k factorial design matrix is a commonly used method for

designing experimental approach[29]. The number of variables, k, can each be divided into two options for each variable, this allows a design matrix to be built exploring the possible combinations that can be made, this is shown below in figure 11[30].

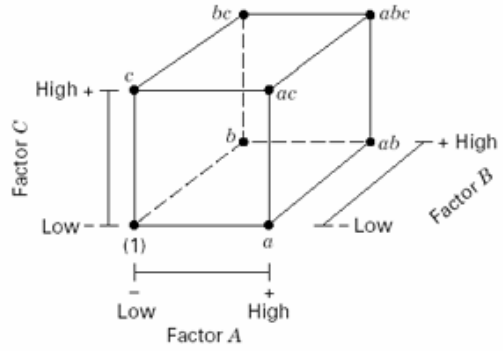

(a) Geometric view

Run	Factor A	B	C
1	–	–	–
2	+	–	–
3	–	+	–
4	+	+	–
5	–	–	+
6	+	–	+
7	–	+	+
8	+	+	+

(b) The design matrix

Figure 11. Design of experiments matrix for a 2^3 factorial analysis

From these combinations the samples or parts are manufactured and tested. From the results, the variables can be studied individually as well as the combined effect of any combination of variables analyzed[33]. This method creates a very systematic process for examining a high number of variables and their contributions. Taking a look specifically at Factor A shown in figure 11, the effect of that variable can be found from the difference in the average values between the high and low conditions as shown in equation 7. Within each variable, two possibilities exist, and by taking the summed difference between the two possibilities and dividing by the number of samples, the effect is found[33].

Eq. 7 $$\text{Effect} = \frac{(R_2 + R_4 + R_6 + R_8)}{4n} - \frac{(R_1 + R_3 + R_5 + R_7)}{4n}$$

In addition this process can be repeated for each factor and every combination of factors (B, C, AB, AC, BC, and ABC). The absolute value of these numbers gives an initial impression of each variables effect. The sum of the squares (SS) for the effects are the next piece of information needed to calculate the percent contribution, it is found by squaring the effect before it is divided by the number of samples and then dividing by eight times the number of samples. A total SS value is found and used to calculate the percentage for each individual SS value which is the final percent contribution. This approach creates an efficient and standardized method for comparing weighted variables[33].

2.4 Manufacturing of Double Box Beams

This section focuses on the manufacturing of Double Box Beams (DBB) using the Cellular Core Technology process. Double box beams were also produced using traditional aluminum tooling as a metric for comparison. Pre-impregnated carbon fiber was used in this study, parts were manufactured with an autoclave to develop aerospace grade structures. Comparisons were made based on visual inspection, characterization, and mechanical testing. Optical microscopy was used to identify differences in quality measured visually. Mechanical testing was performed to validate the CCT process as well.

2.4.1 Materials

This work was done using pre-impregnated (prepreg) carbon fiber materials. Two carbon fiber prepreg materials were used for this study; Nelcote E-765 and Cycom 5320-1. The Nelcote E-

765 provided by Park Advanced Composite Systems was used as both a unidirectional tape and a plain weave fabric[31]. The carbon fiber is T700 material for the unidirectional tape and a T300 plain weave fabric. The resin system has the following cure cycle:

1. Ramp to 130 ˚C (270 ˚F) at 2.2 ˚C/min with a pressure of .6 MPa (89 psi) at a rate of .1 MPa/min (20 psi/min)
2. Hold for 2 hours at 130 ˚C and .6 MPa (the hold temperature was increased to 4 hours for parts made with the DDB due to tooling size)
3. Cool to room temp at 2.2 ˚C/min and atmospheric pressure

The Cycom 5320-1 is an out of autoclave material used for comparisons to model results. This material was chosen for the amount of information available to the model and the ability to run as a two stage cure with stages of 120 ˚C and 176 ˚C. Instructions for use in an autoclave were provided by the manufacturer. A unidirectional tape with T40/800B fibers and a 5 harness weave fabric were used in this study[32]. The cure cycle for that material is given below:

1. Ramp to 120 ˚C (250˚F) at 2.2˚C/min with a pressure of .6 MPa (89 psi) at a rate of .1 MPa/min (20 psi/min)
2. Hold for 2 hours at 120˚C and .6 MPa (the hold temperature was increased to 4 hours for parts made with the DDB due to tooling size)
3. Cool to room temp at 2.2˚C/min and atmospheric pressure
4. Post cure at 175˚C (350˚F) for 2 hours after removing the cellular cores

In addition to the prepreg materials aluminum and steel tooling were used. The cellular cores are made out of an acetal thermoplastic polymer produced using rotational molding to create a hollow inside. In some cases the post cure stage was left out of processing due to the temperature range of the acetal cores. This decision also allowed for a better range of degree of cure data and minimized complexity of the model, however no samples were cured below the required hold temperature for a material and used for mechanical testing.

2.4.2 Cellular Core Tooling

The Cellular Core Technology (CCT) process involves layering plies of prepreg around thermoplastic bottles (cores) which when assembled and cured create a complex structure free of discontinuous parts assembled by fasteners. The method for integrating the cellular cores involves first determining the desired ply number and thickness, followed by identifying the tolerances required between the part and the tooling in the clamshell mold. Once a desirable fit is calculated for the required material, the tooling is polished and cleaned with acetone to remove any debris. A chemical release agent Frekote Safelease #30 is wiped on all surfaces of the tooling to prevent epoxy adhering to the surface. The thermoplastic cores are checked for any defects or tolerance issues before use. Spring steel pressure plates are applied to the sides of the cores using Teflon tape. The prepreg plies are layered around the cores in the desired lay-up as shown in figure 12. The cores are approximately 10.6 cm wide, 12.2 cm tall and 53.3 cm long, the outer geometry of the parts can vary based on the number of plies and the internal tooling components included.

Figure 12. Image of thermoplastic cellular core with prepreg plies wrapped around

The cores are then assembled forming internal ribs where the cores match up. In addition to the plies wrapped around the cores, a filler noodle is placed in the radii of the two cores. The filler noodle is a rolled piece of unidirectional tape that has been pre-formed into the shape of the two radii adjacent to one another and placed in the joint to fill space. The width of tape used is calculated from the cross-sectional area left in the joint of the two adjacent cores have had prepreg wrapped around them and the thicknedd of the unidirectional tape material. A filler noodle size of 125% to 150% the total cross-sectional area was used considering the compaction of the material during cure. A low heat was applied and the noodle was pre-formed using roller bars to fit the desired area. After the noodle had been added, skin plies were placed over the top and bottom surfaces to connect the two cores curing everything together. Figure 13 below shows the placement of the cores in the aluminum clamshell mold and skin plies applied after the noodle placement.

Figure 13. Skin plies added to the cellular cores before closing the mold

The part is sealed in a clamshell mold and cured in an autoclave at the required recipe for the material. The part is then removed, the cores pulled out. Any edges are sanded and cut before testing. A representative sample is shown below in figure 14.

Figure 14. Representative double box beam

The final lay-up of the double box beams consisted of the following ply orientations in each section

Single Core Wrap → $[+/- 45 \text{ weave}]_2$ or $[+/- 45 \text{ weave}]_4$

Skin Plies → $[0/90 \text{ weave}]_3$

2.4.3 Aluminum Tooling

A similar approach was used for preparing the control samples made with the aluminum tooling. Frekote Safelease #30 was applied to the tool surfaces and prepreg plies wrapped around the two aluminum square tubing beams used. Given that the square aluminum tubing had the same radius as one of the conditions for the cellular cores (.635 cm) the filler noodle size was the same. Skin plies were place in the same manner as the lay-up of the cellular cores. Aluminum caul plates were placed on the top and bottom of the skin plies to insure even consolidation and smooth surfaces.

2.5 Processing Evaluation

Using this approach for building double box beams, two studies were performed to evaluate the processing capabilities of CCT. The design of experiments (DOE) approach was used for these studies, first a processing DOE was performed to understand the impact of different variables on consolidation, and second a DOE designed to compare mechanical properties was performed. The processing DOE studied four variables of interest; the radius, noodle size, cell gap, and pressure with two conditions used for each variable. The table of values used for each run is shown in table 3, the radius used were 3.175 mm (.125 in.) and 6.35 mm (.25 in.) for the tooling.

Table 3. Design matrix of samples made with the variables and combinations studied

Run	Radius (mm)	Noodle Size (%)	Cell Gap (mm)	Pressure (kPa)
1	3.175	125	3.5	310
2	6.35	75	3.5	310
3	6.35	125	2.8	310
4	3.175	75	3.5	620
5	6.35	75	2.8	620
6	3.175	125	2.8	620
7	6.35	125	3.5	620
8	3.175	75	2.8	310

The noodle size values were calculated from the filler volume available in the joint after plies had been wrapped around the tooling. The filler noodle volume was found geometrically from the percentage of space available in the joint, knowing that compaction would occur during the cure. The space was calculated by adding the ply thickness to the tool radius and computing the remaining space. Using the known ply thickness for the filler noodle material, the amount of material needed to fill that space was calculated. This approach is demonstrated below in figure 15.

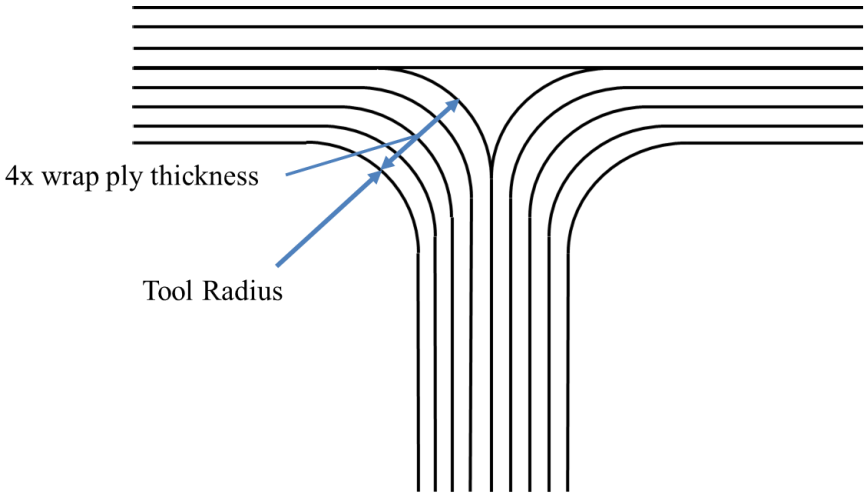

$$Noodle\ Filler\ Area = \frac{1}{2}((4-\pi) \times (tool\ Radius + (\#\ of\ wrap\ plies \times ply\ thickness))^2)$$

Figure 15. Example of joint structures and filler noodle calculation

The cell gap refers to the excess room left between the tooling and the composite through the thickness of the rib. This value is calculated from the ply thickness, geometry of the cellular cores, and the room available inside the clamshell mold. A schematic of this area is shown in figure 16. Finally the pressure is varied to understand the impact on the expansion of the cores.

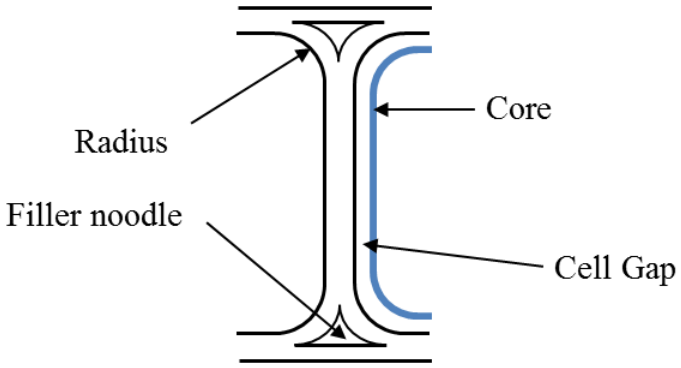

Figure 16. Example of cell gap location in part

Using this study, samples are produced and cross-sectioned for imaging. Parts were evaluated for defects such as porosity and wrinkles. Figure 17 below shows a representative image with the defects of interest. Samples were assessed based on quality of the joints and assigned a value of poor, moderate or high quality.

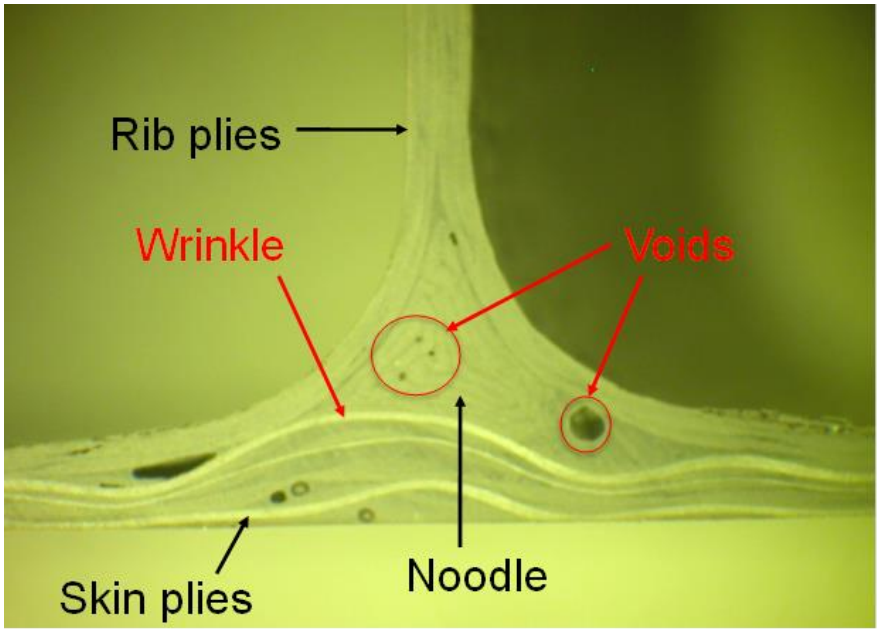

Figure 17. Example joint with representative flaws

2.6 Mechanical Testing of Composite T-Joints

Following the processing DOE, mechanical testing was performed on the joints. A second DOE was developed to evaluate the consolidation of the joints. The T-Joint tensile test was chosen because of the matrix dominated failure in the joints which will show more variation in performance from consolidation. Mechanical testing of these structures was performed using an Instron 4505 in a tension test designed to simulate the rib pulling away from the skin plies. The

test simulates a stiff skin scenario whereby tension is applied on the rib until failure. Samples for the T-joint tensile test were cut from the bottom joint of the double box beam structures and bonded to 2.54 mm thick aluminum. Both the composite skin and the aluminum were sanded with 60 grit sandpaper and wiped clean before applying a paste adhesive to the surface and curing under heat and pressure. This design is advantageous as it helps stiffen the composite skin which is only 5 to 7 plies thick, but also allows for a surface to which you can clamp down on without damaging the specimens. Holes were drilled into the rib of the specimen away from the joint to avoid compromising the area of interest. These were used to bolt aluminum plates which could be clamped in the Instron. In no tests did the holes made by drilling affect the results of the test. The samples all failed in the desired area near the joints. Samples were tested at 1 mm/min until failure, a schematic of this set up is shown in figure 15 below.

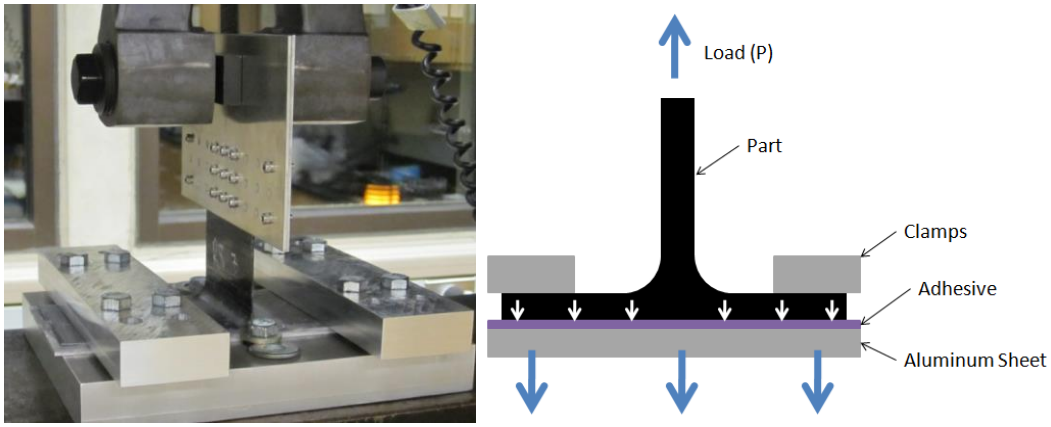

Figure 18. Image and diagram of T-joint tensile test set-up

The variables in question are shown below in table 4. Three variables were chosen for this study; the tool radius, the number of rib plies and splices around the joint.

Table 4. Design matrix of the samples made for mechanical testing

Run	Radius (cm)	Rib Plies	Splices
1	6.35	8	Yes
2	3.175	8	Yes
3	6.35	4	Yes
4	3.175	4	Yes
5	6.35	8	No
6	3.175	8	No
7	6.35	4	No
8	3.175	4	No
Lower Control	6.35	4	Yes
Upper Control	6.35	8	No

The use of splices was studied to determine the effect of discontinuous plies near the joint and whether or not they would drive failure away from the joint. Shown below in figure 19 are the schematic for the splice stacking sequence used in the 2-ply and 4-ply box beams. An overlap splice was used to stagger the discontinuous plies near the joint.

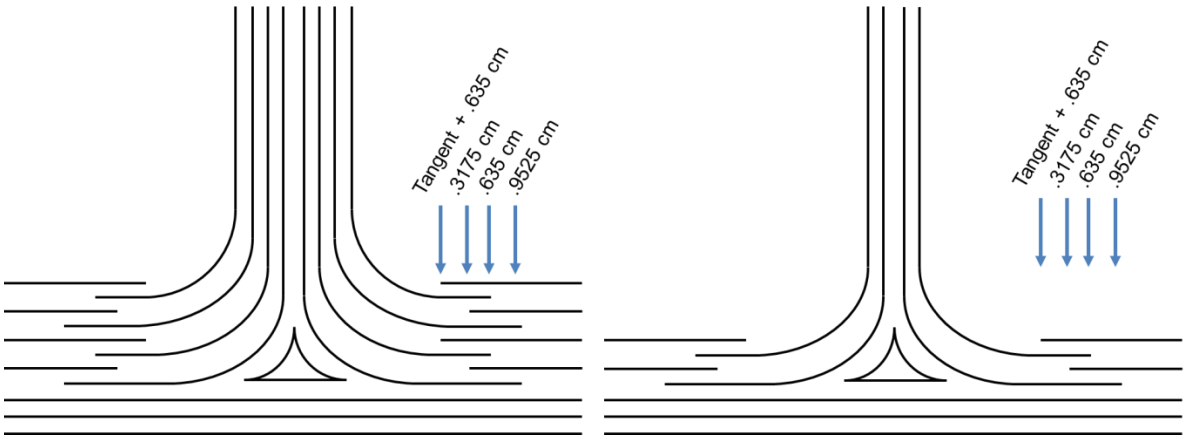

Figure 19. Splice lay-up used for 2 and 4 ply double box beams

2.6.1 Digital Image Correlation (DIC)

Digital Image Correlation (DIC) was performed in conjunction with T-joint tensile testing to gather more data about the failure of the samples. The cross sections of T-joint samples were painted with a white and black speckle pattern; this pattern is used by the cameras to track specimen movement. Five images were taken each second of the test. The Vic-2D software developed by Correlated Solutions was used to evaluate the tracked deformation. Since the DIC technique is non-contact, tensile testing was performed to failure. The strain was mapped on samples during testing and areas of high strain were isolated for analysis.

2.7 Discussion of Results

This section covers the work done to understand and optimize the processing of composites with cellular cores. Several tests were performed on the DBB using the design of experiments 2^k factorial analysis. The first test matrix was an optical test performed by taking cross sections of the samples and examining the part quality. The factors studied were pressure, the gap between cores, noodle size, and core radius. Table 3 outlines the samples made for the cross-sectional imaging and the combination of variables in each part. Using information from first design of experiments a second test matrix was made to study the mechanical performance of the parts made with CCT and compare that to aluminum processing. The variables included for evaluation were radius, number of rib plies, and spliced plies vs. continuous. Table 4 shows the sample combinations made.

2.7.1 Characterization of T-Joints

Initially the microstructure of parts made with cellular core tooling was examined, specifically looking at porosity, ply consolidation, and wrinkles. Pressure, radius size, noodle size and gap size between cellular cores were varied to determine their effects on part consolidation, specifically at T-joints and corners. These initial tests helped optimized the processing and set standards for future mechanical testing. Figures 20 and 21 show representative samples and the variance in quality observed. It was concluded that cell gap, noodle size, and radius were all necessary for producing a high part quality, but not all equally important and the interaction between variables could not be ignored. Parts could be made at 310 kPa without a significant drop in compaction if the filler noodle was adequately large enough to fill the space and shaped well to conform to the joint. The filler noodle size was studied further and it was found that 125% to 150% of the filler volume was satisfactory as well for filler the joint. Porosity appeared to be a larger concern than wrinkles in the joints as an improperly sized or shaped noodle would contribute directly to empty space that the material would struggle to fill in some cases. The gap between cells was the most significant factor for producing a high quality part. All of the parts with a large cell gap did not consolidate, indicating that there is a limit to the expansion of the bottles. It has also been speculated that the fibers themselves can restrict expansion so limiting the amount of space the cores must expand to fill is essential for part quality.

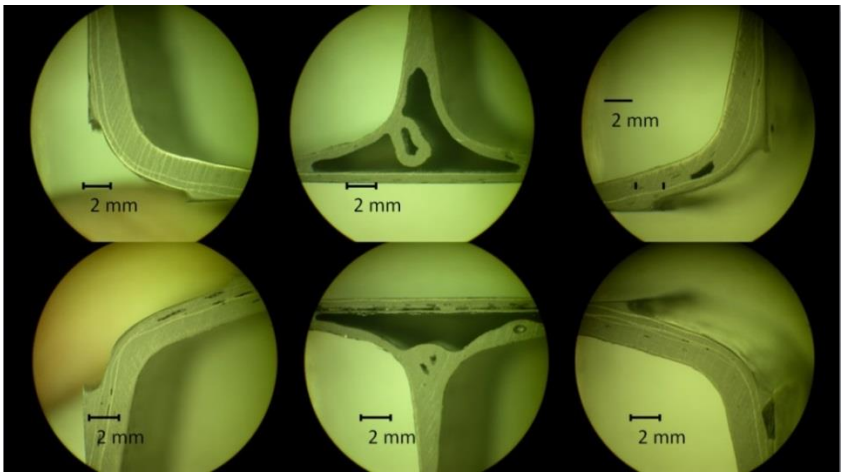

Figure 20. Image of low quality part

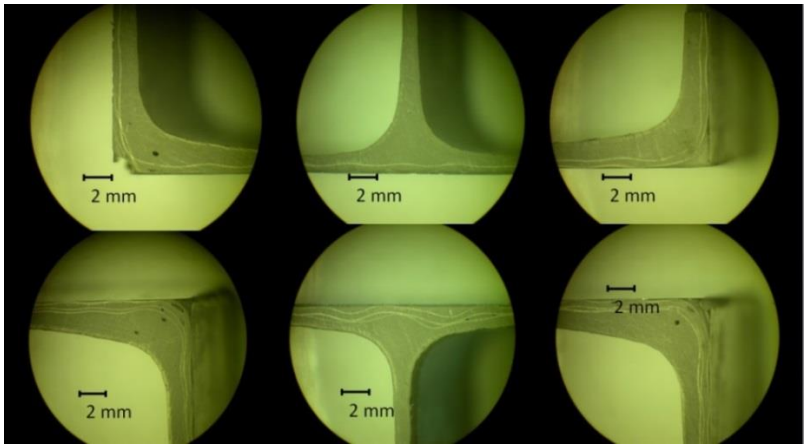

Figure 21. Image of high quality part

2.7.2 Mechanical Testing of T-Joint Composite Structures

The joint connecting rib and skin plies was identified as an area of study, as such the T-joint tensile test was designed with the intent to cause failure at that location. With the exception of one specimen from part 6, which failed in adhesion to the aluminum and was left out of the study, the rest of the samples failed in the joint. Failure occurred either by: A) crack growth between the skin plies and the rib plies that wrapped around the tool or B) in the middle of the

rib plies up the length of the rib. In all cases, the crack began at or around the filler noodle and propagated away from the junction and in most cases eventually grew in all three directions. A typical failure is shown in figure 22 and the load profile is shown in figure 23.

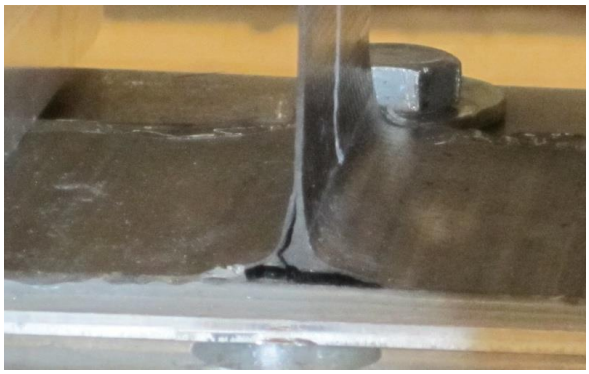

Figure 22. Image showing failure mode in cracked part at 1.5 mm extension

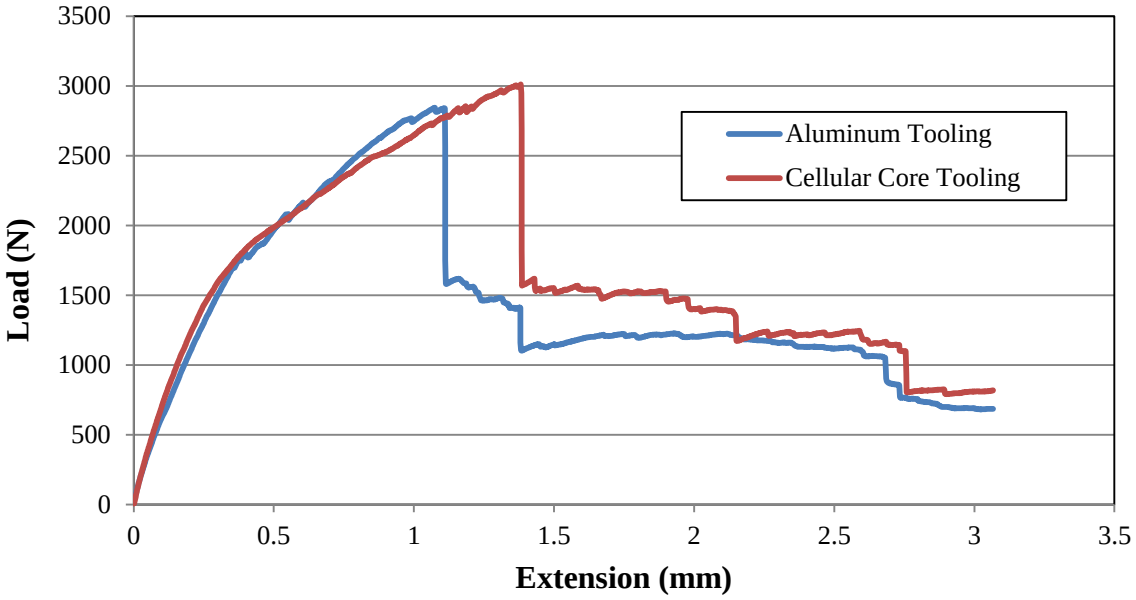

Figure 23. Load vs. Extension curve for T-joint samples

The maximum strength of each part was identified and recorded for comparison. Those values and the average for each part can be seen for each test in Figure 24.

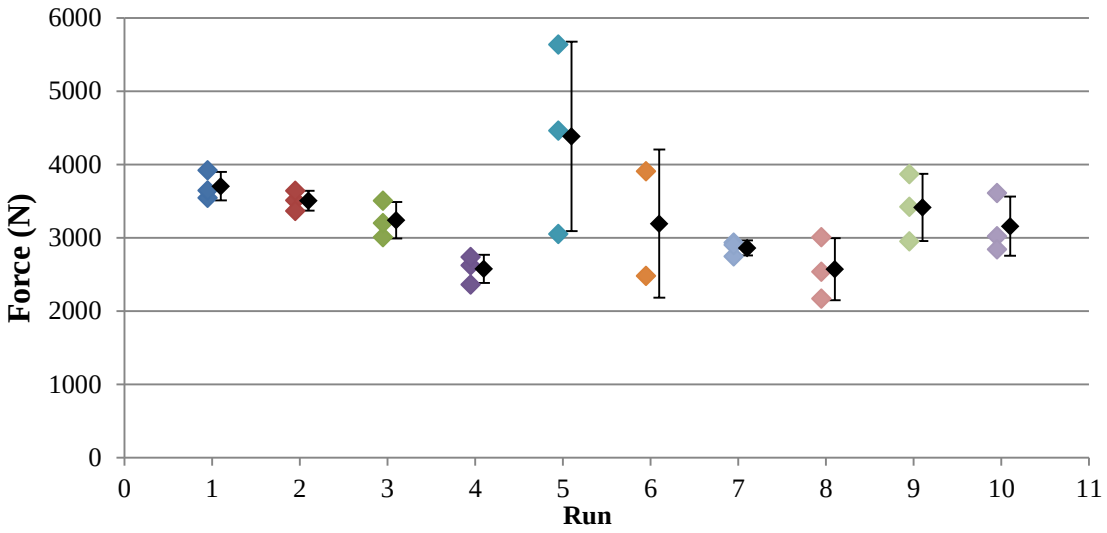

Figure 24. Maximum force and average maximum force for each part

The cellular core tooling parts can be directly compared to the metal tooling parts. Parts 3 and 5 have the same lay-up as the control parts (9 and 10) made with aluminum tooling. The cellular core parts have a higher average pull off strength than the control parts, indicating an improved mechanical performance from the cellular cores. This is important for illustrating that cellular core tooling has the potential to be mechanically superior to traditional tooling. This data is also shown in Table 6 with the actual values. It should be noted that the standard deviation in Run 5 is much greater than the variance in the controls. Specimen 5 was sectioned and examined to find porosity in the joint of the sample explaining the high variance between the coupons. Specimen 5 was expected to have the highest pull-off strength given the lay-up and ply number which held true, however, processing defects led to premature failure in some of the samples. An improved

specimen 5 was made with an increased noodle filler volume (125% to 150%) and compared to the original samples shown in figure 25.

Using analysis methods tailored for design of experiments matrices, more than just comparisons between the tooling methods can be evaluated. The relative weight of the variables in question is evaluated and the results shown in Table 5. The number of rib plies is found as the largest factor affecting mechanical strength for this test. Doubling the number of rib plies from 4 to 8 showed a clear effect on the strength and support our understanding. The second largest contributing factor, the radius, also makes clear sense from two perspectives, the larger radius allows a larger noodle to fill the joint improving strength, and the large radii is a much smoother out of plane transition creating a smaller stress concentration at the joint. This data is supported in literature findings as well, larger radii create a stronger joint. The splices appeared to have no effect on the part strength indicating there is good overlap between the plies. It also suggests that splices could be used in manufacturing when continuous plies are not feasible.

Table 5. Full design of experiments analysis chart

Run	Radius (cm)	Rib Plies	Splices	R/P	R/S	P/S	R/P/S	Average (N)
1	6.35	8	Yes	+	+	+	+	3703.99
2	3.175	8	Yes	-	-	+	-	3505.46
3	6.35	4	Yes	-	+	-	-	**3238.84**
4	3.175	4	Yes	+	-	-	+	2574.37
5	6.35	8	No	+	-	-	-	**4383.31**
6	3.175	8	No	-	+	-	+	3192.98
7	6.35	4	No	-	-	+	+	2860.69
8	3.175	4	No	+	+	+	-	2570.84
Lower Control	6.35	4	Yes	N/A	N/A	N/A	N/A	**3158.23**
Upper Control	6.35	8	No	N/A	N/A	N/A	N/A	**3412.96**
Effect	195.26	295.08	1.24	36.21	-51.43	-62.38	-113.87	
% Contribution	**26.11**	**59.63**	**0.00**	**0.90**	**1.81**	**2.66**	**8.88**	

In addition to the effects of radius, rib plies, and splices, the combined effect of any of these variables can be studied as well. Using the same techniques as individual variables, the percent contribution is calculated, as shown above, the contributions from combined variables are significantly smaller than the effects of rib plies and radius. The effect of any two variables appears negligible but there is a small jump in the percent contribution from the effect of all three variables.

Further analysis of sample 5 concluded that porosity caused the high standard deviation observed. This sample was built again after re-evaluating the noodle size with more attention paid to final noodle shape. The part was re-made with the noodle increased from 125% to 150% size. The original and improved T-joint mechanical data is shown below. There is a significant improvement in both strength and consistency within the samples indicating that the problem was mitigated. The improved sample showed a 49% increase in average strength over the original sample and a 91% increase over the sample made with aluminum tooling. Unfortunately,

the last of the materials were used for the improved CCT sample, not allowing an aluminum tooled sample with 150% filler noodle to be made for direct comparison.

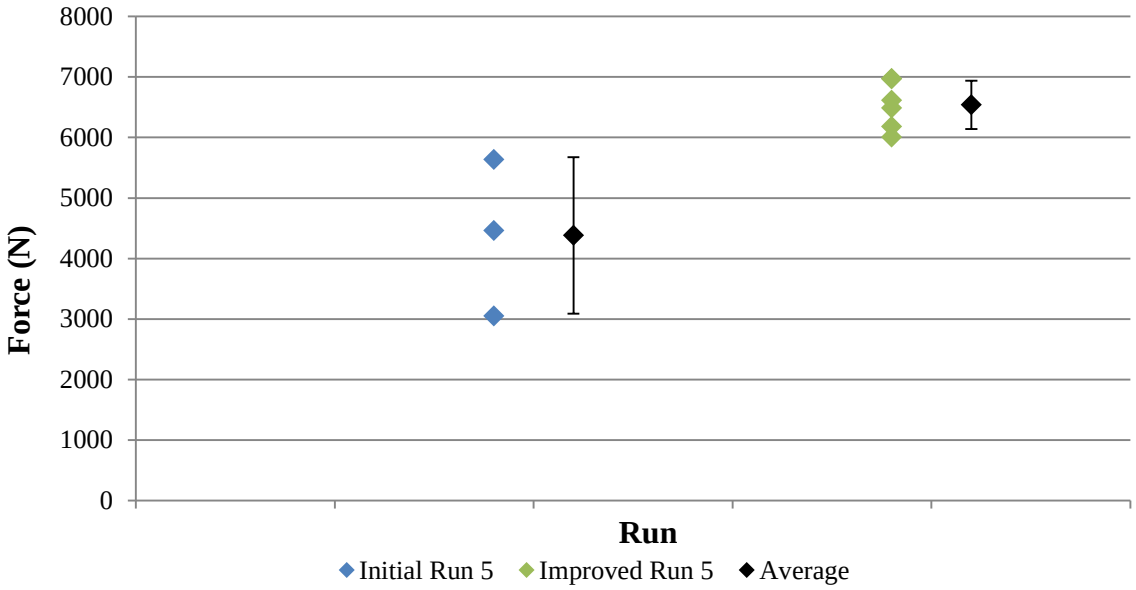

Figure 25. Original and Improved Sample 5 (black diamond with error bars)

2.7.3 Digital Image Correlation in T-Joint Composite Structures

Analysis using DIC confirms what was shown during mechanical testing. The strain is highest at the interface between the filler noodle and the rib plies. At this location the fibers in the noodle run along the cross section perpendicular to the load path. The fibers of the rib plies also curve out of plane with the load direction as they move into the skin of the part. This means that the joint is the most likely location for failure as high interlaminar normal stresses are created which cause a peeling failure as the rib plies pull away from the noodle and the crack propagates away from the joint. Figure 26 shows an image taken during DIC highlighting the strain in the sample

around the noodle; where the red line intersects the noodle outline indicates where failure occurred.

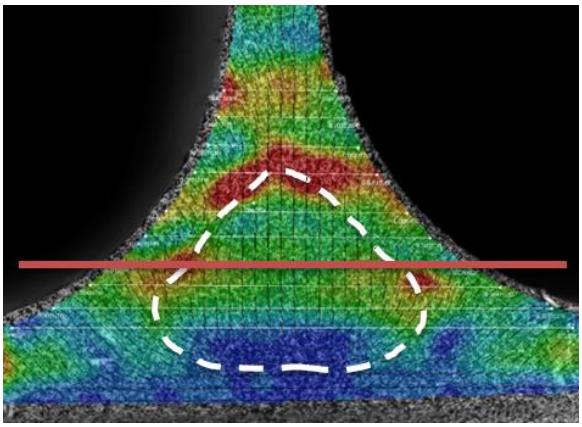

Figure 26. DIC image showing strain in T-joint tensile test

2.8 Summary of CCT Composite Characterization

Samples were prepared using two different tooling methods; cellular cores and aluminum tooling. A design of experiments approach was used to evaluate the microstructure of T-Joints. It was concluded that the cell gap was the most critical factor in determining part quality at the joints, but each variable played a significant role. Noodle size and shape were one of the more difficult processing challenges having a very diverse range of effects on the joint. If not properly prepared the noodle could single-handedly cause major porosity around the noodle. While high pressure is important for processing it was found that high pressure was not significant enough to overcome a small or poorly shaped noodle. Using this information T-Joints were manufactured for mechanical testing on the basis of evaluating consolidation at the joints. The out of plane transfer of stress around a joint made the matrix dominated peel failure ideal for exposing

porosity and improper consolidation. The CCT process performed well in regard to strength relative to the control samples, indicating that the CCT process has equivalent if not superior strength to samples processing with aluminum. Some porosity in CCT samples was noted and corrected for, showing a significant improvement over the original sample.

Chapter 3: Thermal Modeling of CCT

This chapter focuses on the background and approach taken for developing the thermal model. The mathematical expression for heat transfer in composites is discussed in detail as justification for the method. The mathematical expression for heat transfer coefficient (HTC) is given and its influence on modeling practices. Procedures for developing the thermal model and collecting experimental data for model validation are discussed. Results of the modeling are given and conclusions from the data are summarized.

3.1 Heat Transfer in Composites

The first stage of modeling composite processing is the heat transfer through a part. The heating profile dictates the instantaneous degree of cure throughout the structure, the rate of cure, and the instantaneous resin viscosity which are all necessary for later stages in the model. The heat transfer can be a complex step and part specific due to factors ranging from geometry, materials, tooling, autoclave, and the cure recipe. This model is fundamentally a three dimensional heat transfer model with a heat generation term added for the exotherm of the resin ($\dot{Q}$) which is then fed into the resin kinetics model. Because of this, the thermochemical module is often broken down further into two sub-models; the heat transfer model and the resin cure kinetics model. The heat transfer model maps the temperature profile throughout the part during cure. This becomes challenging as structures become more complex and the heating profile can vary significantly throughout the part. Material property values are imported to account for heat capacity, thermal conductivity, and any heat generated during the process (exotherm of the resin). The second half

of the model handles the resin cure kinetics. The degree of cure is the final value determined, but the relationship between the heat transfer and cure kinetics is incredibly strong, as the resin cures there is heat generation from the resin exotherm and the thermal conductivity is changing as the degree of cure increases. This means that the heat transfer must adjust at each time interval to account for the difference in the resin chemistry. The governing equation for the thermochemical module is given below[15].

Eq. 8 $$\frac{\partial}{\partial t}\left(\rho C_p T\right) = \frac{\partial}{\partial x}\left(k_{xx}\frac{\partial T}{\partial x}\right) + \frac{\partial}{\partial y}\left(k_{yy}\frac{\partial T}{\partial y}\right) + \frac{\partial}{\partial z}\left(k_{zz}\frac{\partial T}{\partial z}\right) + \dot{Q}$$

Eq. 9 $$\dot{Q} = \frac{d\alpha}{dt}(1 - V_f)\rho_r H_R$$

Where ρ is the density or the resin or fibers, k is the thermal conductivity, C_p is the specific heat of the material, and α is the degree of cure. The cure rate is denoted by $\frac{d\alpha}{dt}$ and H_r is the total heat of reaction. The rate of cure is a complex term which is determined in a variety of ways using either mechanistic or empirical methods but ultimately is a function of both temperature (T) and degree of cure (α)[18]. Often the cure rate must be expressed using two different expressions over the course of the reaction as the rate controlling parameter switches from the kinetics of bond formation to diffusion of polymer chains through the macromolecular network. Bogetti and Gillespie detail a set of empirical equations they have used to model the cure rate in epoxy systems which are given below[19].

Eq. 10 $$\frac{d\alpha}{dt} = (k_1 + k_2\alpha)(1 - \alpha)(.047 - \alpha) \text{ when } \alpha \leq .3$$

Eq. 11 $$\frac{d\alpha}{dt} = k_3(1 - \alpha) \quad \text{when } \alpha > .3$$

Where k_1, k_2, and k_3 are expressed as follows, with A representing pre-exponential coefficients and ΔE is the activation energy.

Eq. 12 $$k_1 = A_1 \exp(\frac{-\Delta E_1}{RT})$$

Eq. 13 $$k_2 = A_2 \exp(\frac{-\Delta E_2}{RT})$$

Eq. 14 $$k_3 = A_3 \exp(\frac{-\Delta E_3}{RT})$$

In the context of the CCT process, which takes advantage of the ability to create complex integrated structures, the capability to find lead and lag zones in a complicated structure can be helpful prior to building large prototypes. Areas for potential overheating from high exotherm can be identified and modified to avoid unnecessary residual stress, however this is typically an issue with thicker laminates with a higher exotherm from resin crosslinking. An example calculation has been included in Appendix A detailing the contribution of the exotherm to the overall temperature increase in a plate laminate during cure. This has been used to demonstrate that with most structures the temperature increase, while measureable is still relatively small.

3.1.1 Heat Transfer Coefficient

In autoclave processing the part is heated up by convective heat transfer and in some cases through thermal conductivity of tooling. Convective heat transfer inside an autoclave can be difficult to quantify and the turbulent flow of air can create areas with different heat transfer coefficients, particularly if there is a large part in the autoclave[18, 33]. Factors such as pressure,

location, ramp rate, and part size/shape/materials can all influence and change the heat transfer within an autoclave. Convective heat flux is described by the following equation.

Eq. 15 $$\dot{q} = hA(\Delta T_s)$$

Where h is the heat transfer coefficient, A is the surface area, and ΔT_s is the difference in temperature between the solid surface and ambient temperature. The equation for heat flux can be re-arranged to yield the following expression for the heat transfer coefficient[22, 33].

Eq. 16 $$h = \frac{\Delta Q}{A\Delta T_s \Delta t}$$

Where ΔQ is the heat gained or lost, and Δt is the time period. The heat input can be specified further by the following expression over a defined period of time (Δt).

Eq. 17 $$\Delta Q = \int \rho C_p \Delta T \, dV$$

Where ρ is the density, C_p is the specific heat of the material, V is volume, and T is temperature. Calculating the heat transfer coefficient (HTC) for an autoclave can be accomplished by measuring temperature differences during heating of known objects at various locations within the autoclave. The heat transfer is typically determined using lumped mass calorimeters, which assume no temperature gradient through the thickness of the calorimeters, simplifying equation 17 to the following expression.

Eq. 18 $$\Delta Q = \rho C_p \Delta T V$$

Using lumped mass calorimeters placed throughout an autoclave, the heat transfer coefficient can be determined by re-arranging equation 18 into the following form.

Eq. 19 $$h = \frac{\rho C_p V \dot{T}}{A \Delta T_s}$$

Where A is the surface area, $\dot{T}$ is the instantaneous temperature ramp rate, and ΔT_s is the difference in temperature between the ambient condition and the surface of the calorimeter[33]. Because of the high variance in the HTC, in many cases the HTC is found for tooling surfaces through experimental testing using calorimeters, or by guess and check modeling of those surfaces to mimic the data collected. For this study, a sensitivity analysis is performed where the HTC values of surfaces are systematically varied and compared to experimental data. This approach approximates the heating profile observed in a part and tool by finding HTC values of surfaces that match the experimental data.

As a comparison for the sensitivity analysis run to determine the HTC values required in this study, a lumped mass calorimeter approach was used against one of the surfaces. A thermocouple was imbedded into a steel rod and the difference in temperature between the rod and the ambient autoclave conditions was found. Using equation 19 and the material properties of the steel rod, the HTC value can be approximated for that location in the autoclave. This work is shown in detail in Appendix B and it was determined that the sensitivity analysis was a reliable method for approximating the HTC values inside an autoclave.

3.2 Thermal Plate Model

A one-dimensional mathematical heat transfer model was developed for a laminate using the approach outlined above by Bogetti and Gillespie[19]. The model incorporates the thermal properties of the composite (thermal conductivity, density, and specific heat) with the changing properties of the resin, specifically the crosslinking and associated exotherm. This model was used as a tool to validate that the approach taken by COMPRO CCA matches work done previously in prediction of heat evolvement through the thickness of composite parts. A matching laminate plate was developed in Abaqus for comparison using the COMPRO CCA plug-in to demonstrate the accuracy of the method.

Using the equations detailed in section 3.1 a program was built using Fortran to incrementally solve the heat transfer problem and degree of cure for a 30 mm thick composite section during a typical cure cycle. The heat transfer problem was approximated using a Taylor series and finite difference approach incrementally step through the heat conduction through the thickness. The Fortran code used can be found in Appendix C.

In tandem to the Fortran code, a 30 mm thick composite laminate was modeled with 20 plies through the thickness. The open literature material AS4-3501-6 tape material was used for this study, shown below in table 6 are the material thermal properties used for both the FEA model and the mathematical mode. This material was chosen for its well-established material properties as a check on the technique performed in this study[34].

Table 6. Material Thermal Properties for AS4-3501-6 tape

Material Property	Value
Density, ρ	1.52E3 kg/m^3
Specific Heat, C_P	9.42E2 KJ/W˚C
A1	3.503E7 sec^{-1}
A2	-3.357E-7 sec^{-1}
A3	3.266E3 sec^{-1}
Heat of Reaction	198.9 KJ/kg
E1	8.07E4 J/mol
E2	7.78E4 J/mol
E3	5.66E4 J/mol

A 20 ply panel was meshed using the DC3D20 quadratic heat transfer elements with 20 elements through the thickness. The DC3D20 are general heat conduction elements which model heat transfer through solids well, and by discretizing the through thickness into 20 elements each ply is represented as a single element. Shown below in figure 27 is an image of the plate model used.

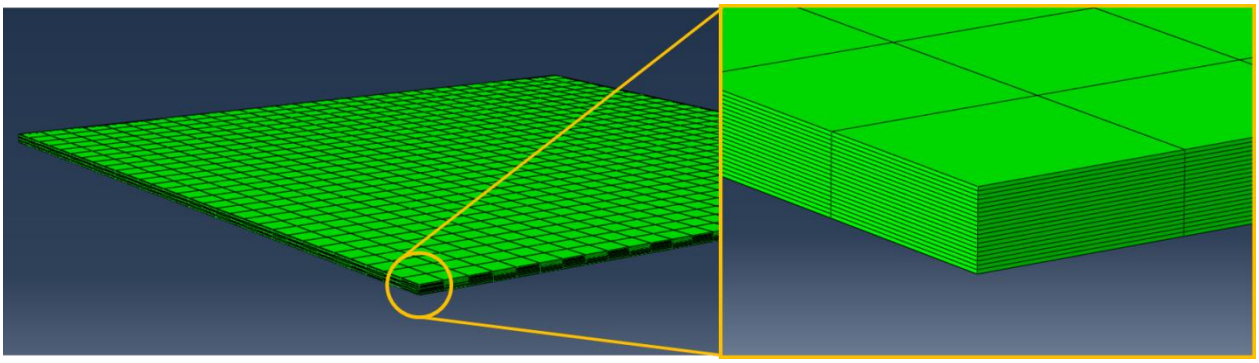

Figure 27. Image of modeled plate with mesh showing mesh density through thickness

The plate was fixed in space and a heating condition applied to the top and bottom surfaces. In both models an autoclave cure cycle was used as the boundary condition for applying heat to the surfaces. The surfaces were ramped to 176 ˚C at 1.11 ˚C/min and held for 2 hours. In the case of

the FEA model edge effects are avoided by applying heat only to the top and bottom surfaces of the panel.

The mid-plane temperature and degree of cure for both the mathematical model and the FEA model were plotted. Figure 28 shows good agreement between the two approaches as expected. Looking at the documentation for COMPRO CCA and the material file for AS4-3501-6 the FEA model uses the same analytical approach as taken by Bogetti and Gillespie which is shown in equations 8-14[35].

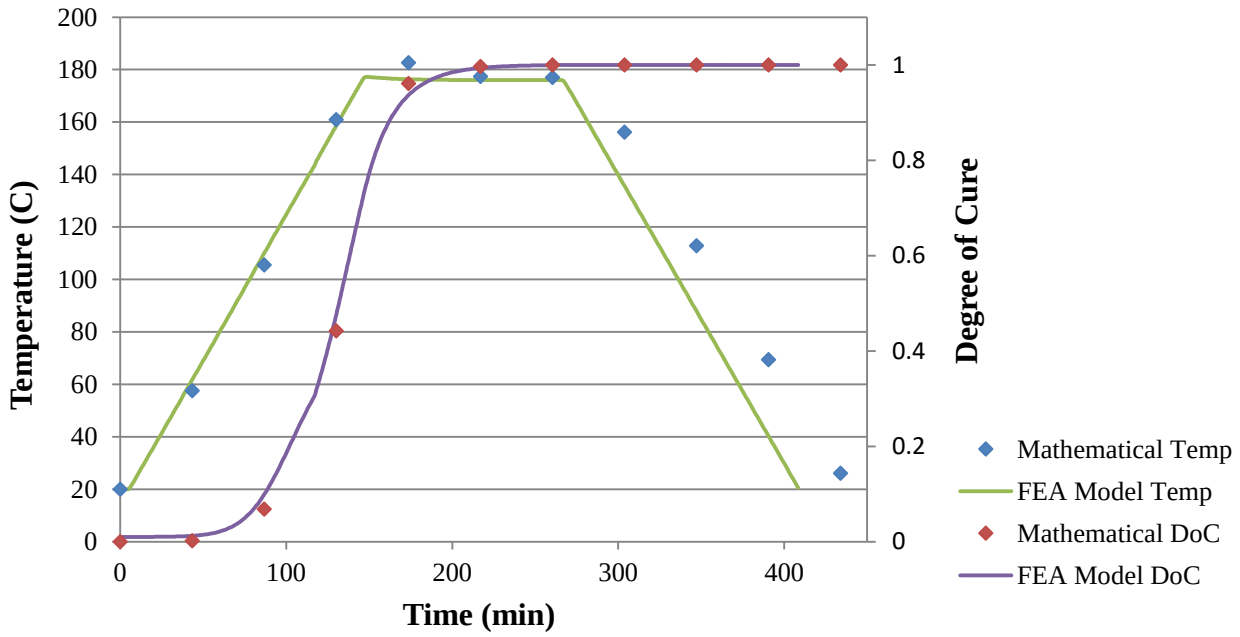

Figure 28. Temperature and degree of cure for FEA model and mathematical model

This demonstrates the accuracy of the FEA approach to modeling composite heat transfer and justifies the use for more complex structures. As the part geometry becomes more complex, a purely mathematical approach can quickly become difficult to model structures. Taking

advantage of FEA to discretize and model structures allows problem solving of otherwise impossible structures.

3.3 COMRO CCA – Thermal Model

This section outlines the approach taken for building the thermal model using CCT. Discussion of each module is presented with justification for the design of the model given. In addition a model of the aluminum tooling method has been developed for comparison to the CCT method.

3.4 Thermochemical Model – CCT Approach

The thermal analysis was carried out by importing SolidWorks 3D part files in Abaqus for the aluminum tooling and the thermoplastic cores. Composite plies were drawn up in Abaqus around the cores using the cured ply thickness of the Cycom 5320-1 material ($1.617 \times 10^{-4}\, m$). Because the flow module is ignored in this study the cured ply thickness can be defined from the beginning to model the part so that it matches with experimental data. The cured ply thickness was determined experimentally from a compaction study and also duplicated in the model data file. A representative image of the composite and the tooling components can be found in Appendix D. Partitions were created in the tooling components to help with mesh development and in the composite to separate plies. The approach to partitioning any structure is centered on breaking complex parts into smaller, simpler pieces. With the tooling components efforts were made to partition into rectangular or square components for mesh quality. In many cases because of the complex shapes in the tooling pieces are not broken into exclusively rectangular or square

components but large areas are simplified to improve meshing. With regard to the partitioning of the composite, the partitioning is performed between plies to allow for ply lay-up definition. Local material orientations were assigned to identify the stacking and fiber directions. During the stress analysis the local material orientations must be specified further for the differing fiber directions within the composite.

During the thermal profile simulation, quadratic heat transfer elements (DC3D20) are used for all components in the model. This element was chosen because as a second order quadratic heat transfer element through thick heat transfer via conduction it is well designed for heat transfer. It is also compatible with the ideal element type used in the stress analysis which is critical as will be discussed in the stress analysis section. The mesh was built using a combination of tetrahedral elements for some tooling components and quadratic elements for the composite. The composite mesh is the most critical area to mesh correctly so significant care was taken in this area. The composite was designed to have at least 4 elements through the thickness as recommended by Convergent CCA with one element representing each ply. With modeling of composites it is important to have elements and partitions in the through-thickness direction divisible by the number of plies, this insures that when ply definitions are assigned the ply locations are easily separated by the nodes between plies. This also insures that analysis is simplified when pulling data from the model, knowing exactly which ply the data is coming from is important when trying to conceptually understand the data. Higher mesh refinement was used through the thickness of the composite for this reason with no more than a ratio of 10:1 between the elements used for the length and the thickness as recommended by Convergent Manufacturing

Technologies as a starting point. A courser mesh was used for the tooling components given the ease of modeling isotropic aluminum and steel structures.

As with many models, sensitivity analyses are often the first test performed to understand what aspects of the model are most impactful. This can also be helpful for determining the most efficient design of the model, determining how course a mesh can be while still maintaining model accuracy is valuable for time savings. Mesh density analysis were performed on each component individually to see the impact on data. A mesh density was found for each tooling component that kept the model running as fast as possible while maintaining model accuracy. With respect to the composite part, the mesh density was not varied in the through thickness reason for the reason stated above; the ply stacking should match up with the element thickness. In the length of the composite a starting element length of approximately 10 times the through thickness elements was used as recommended. A mesh density analysis was performed by increasing the density and making the ration 5:1. In this case no change in the model data was observed indicating that the 10:1 ratio would serve well and save on time over the 5:1 ratio. A courser mesh was not tested given the recommendation by Convergent and knowing that any changes would not improve accuracy but only save on processing time. Following the part meshing each component was combined into the assembly. Shown in figure 29 below are the assembled parts with their respective meshes and a magnified image of the center rib in figure 30.

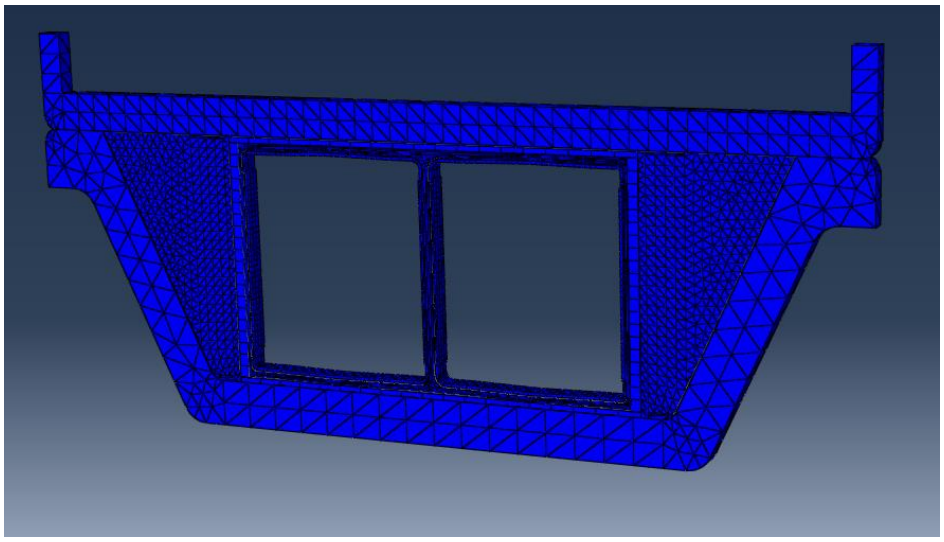

Figure 29. Image of assembly cross section

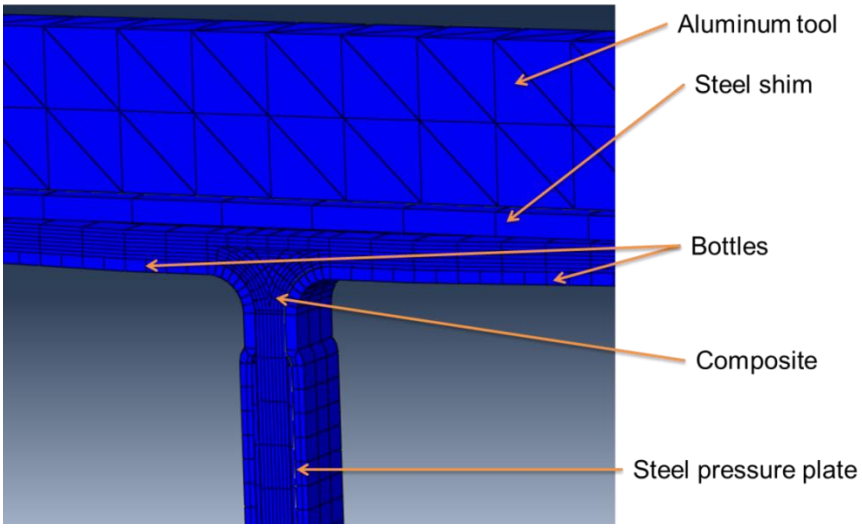

Figure 30. Image of assembly and mesh

Material data provided by Convergent Manufacturing Technologies was used for the aluminum and steel tooling. Data provided by The Boeing Company was used for modeling the Cycom 5320-1 composite material. This material was chosen because of its wealth of information regarding cure kinetics and the material has an alternate two stage cure cycle allowing the

material to initially cure at 120˚C and then post cure at 176˚C. This is important because experimentally the CCT process was limited by the cores available which must stay below 155˚C. This allowed the parts to cure at 120˚C and then run a free- standing post cure when desired. The data for the cellular cores was developed using a combination of literature values and experimental data for acetal thermoplastics. The thermal properties of the acetal were assumed constant with respect to temperature during the thermal analysis. For proprietary reasons the material data file for Cycom 5320-1 was left out of this document but an example material data file used by COMPRO CCA can be found in Appendix E.

After the assembly was built, tie constraints were used for surfaces in contact to define heat transfer between surfaces. The tie constraint specifies that adjacent nodes on different surfaces will have the same temperature values during heating. With respect to the tie constraints a master and slave surface must be specified and general practice is to assign the part with the courser mesh as the master surface, although this is more critical during stress analysis when mesh penetration can be an issue. An autoclave cure profile was defined based on what had been used for curing experimental parts and is shown in table 7 below.

Table 7. Table of Cure Recipe used in Abaqus COMPRO CCA

Time (sec)	Temperature (˚C)
0	30
600	30
3060	120
17460	120
19920	30

Through the load module a *surface film condition* is applied to all surfaces exposed to the autoclave. At this stage in the model the heat transfer coefficient (HTC) at these surfaces is defined. The tooling surfaces were broken down into different regions to define HTC values based on the suspected airflow and location in the autoclave. Values anywhere from 5 to 300 can be used based on the specific autoclave conditions and size, as well as the parts in the autoclave[33]. The higher the air flow around a location; the higher the heat transfer coefficient due to the heavy input of hot air flowing over it.

The simulation was designed to output the temperature data and degree of cure (where relevant) at each node of the assembly for matching to experimental data. From this output database the stress model was built to allow the thermal data to be used as input due to the mesh coherency.

3.4.1 Thermochemical Model – Aluminum Tooling Approach

The approach to the part made with aluminum tooling was very similar. To minimize differences the exact same composite part was used for this study. Aluminum square tubing was drawn directly into Abaqus matching the interior surface of the composite. Top and bottom caul plates were also drawn in with the thickness used in the experimental samples. A coarser mesh for the aluminum was found acceptable for the analysis, however care was taken around the radius. While a coarser mesh is necessary for the master surface in contact with a slave surface to avoid penetration, it is ideal to have close matching between the two surfaces. Convergence issues arise if the master surface is too coarse compared to the slave surface. The final assembly and mesh are shown below in figure 31.

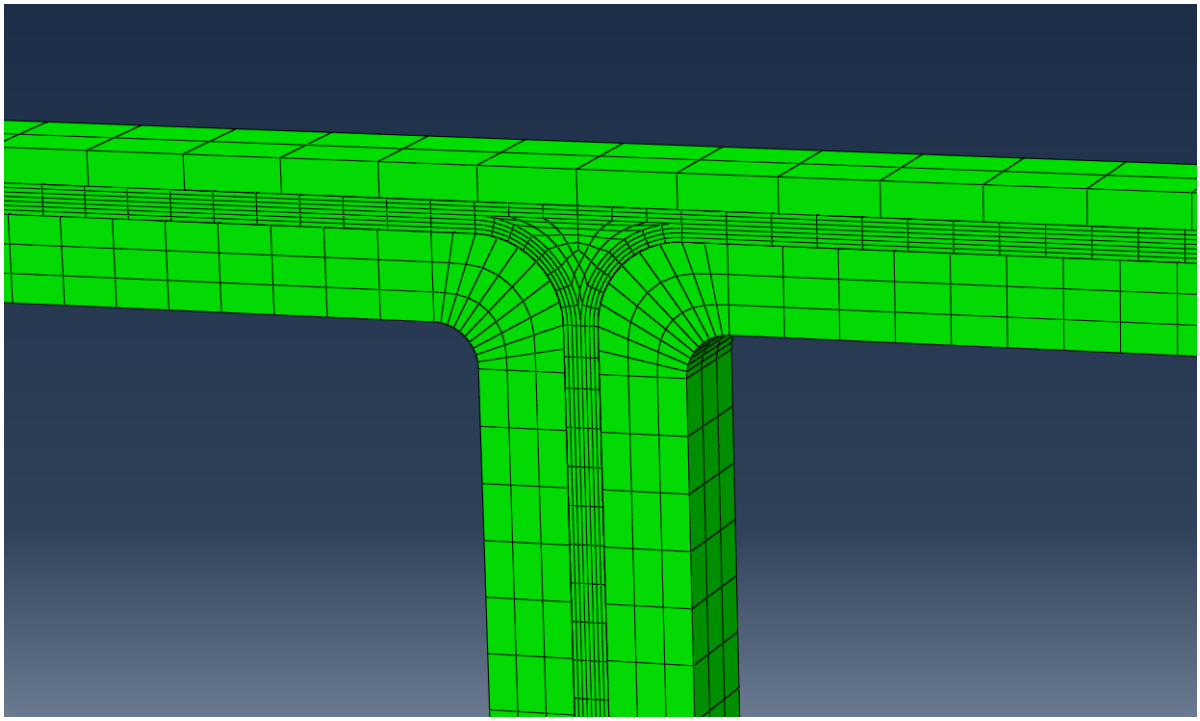

Figure 31. Image of assembly and mesh for aluminum tooling part

3.5 Experimental Temperature Data

Thermocouples were positioned throughout the DBB to obtain a comprehensive map of the temperature during the cure cycle. The locations for these thermocouples are shown in figure 32 below, the data was collected every 2 minutes throughout the run and over several cure cycles to verify consistency of the heat up, dwell and cool down.

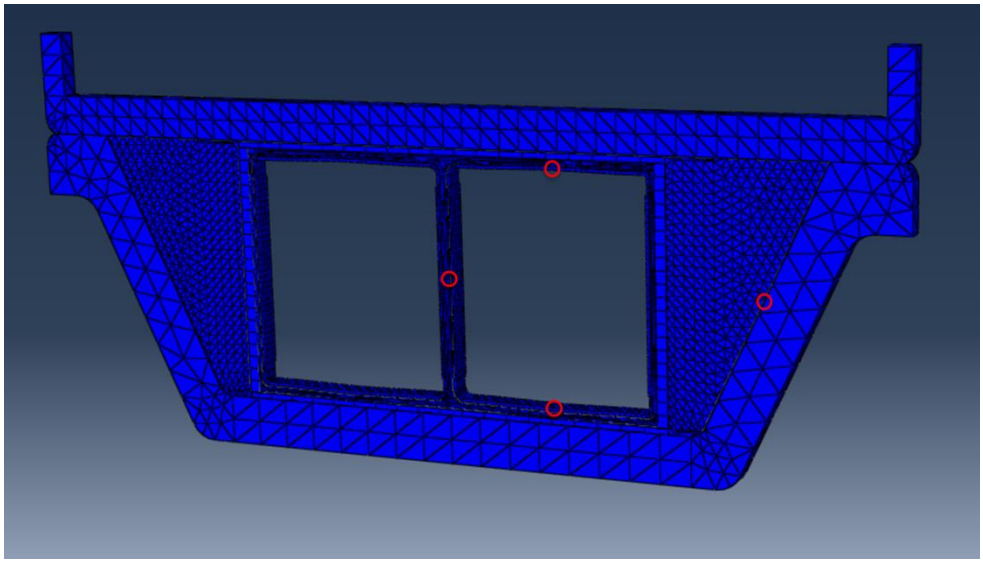

Figure 32. Image of thermocouple locations

3.6 Differential Scanning Calorimetry (DSC)

Differential Scanning Calorimetry (DSC) was performed on samples taken from the cured box beams to determine the degree of cure of the resin. Degree of cure is evaluated to understand how the part is heating up and if any areas are suspect to variance. This data is then compared to the degree of cure predicted in the model developed. DSC heats up the sample in a small chamber which can accurately monitor temperature changes. As the chamber heats up at a controlled rate, the sample will either absorb or release heat depending on whether it is endothermic or exothermic, typically epoxy cure reactions are exothermic, giving off heat as they cure. The Calorimeter will adjust how much heat it must push into the chamber based on the response of the material and this adjustment is recorded. This data is measured as a function of heat generated or lost per gram of the material. The exothermic response of epoxies while it's curing makes DSC ideal for measuring any residual curing possible.

DSC was performed on a variety of samples; first uncured prepreg samples were run in a dynamic ramp that went to 250 ˚C at 5 ˚C/min to determine the total heat generated by the epoxy. Control samples were created by running uncured samples through the DSC using the cure cycle for each material to get an ideal cure value when compared to the value of total heat generated. Together these can be used to calculate the degree of cure of the sample using the equation 20.

Eq. 20 $$\alpha\ (degree\ of\ cure) = \left(\frac{1 - Residual\ heat\ generated\ in\ sample\ from\ cured\ part}{Total\ heat\ generated\ by\ uncured\ piece}\right)$$

Finally samples were taken from various locations in the structure and the same dynamic cure was performed to determine any residual heat generated and ultimately the degree of cure. Samples were sectioned from the same locations that the temperature was originally monitored throughout the DBB (figure 25) and compared to the degree of cure in an ideal sample.

3.7 Discussion of Results

A sensitivity analysis was performed with the HTC of several surfaces to isolate its significance and match the temperature profile to experimental data. From the sensitivity analysis HTC values for the surfaces were determined. Once the HTC values had been approximated for the autoclave and the final thermal model run, degree of cure values were collected from the model and compared to experimental samples for validation.

3.7.1 Sensitivity Analysis

The Heat Transfer Coefficient (HTC) is an important variable for thermal modeling. As covered earlier the HTC values can be calculated from experimental data taken throughout an autoclave based on the heating profile around the tool. An alternative method for determining the HTC values is through experimental validation. A sensitivity analysis was performed to examine the effects of HTC on the heating profile in the part. The HTC values were varied incrementally for the outside surface of the aluminum tool and the inside surface of the cellular cores. The recommended values for HTC in an autoclave are 20.0 J/sm^2K for an aluminum surface and 80.0 J/sm^2K for a bagged composite surface so these were used as the starting values for the sensitivity analysis. The temperature profile was evaluated at the four locations specified earlier; the middle of the rib, the top skin, bottom skin, and outside the aluminum side wedge. A HTC value of 20.0 J/sm^2K on the outside surface was held constant while the HTC value on the inside was varied incrementally. For the study of inside HTC variance focus was on the middle rib as this area is most sensitive to the variations in heating efficiency. The results of this study are shown in figure 33 and compared to experimental data collected to determine the most accurate values.

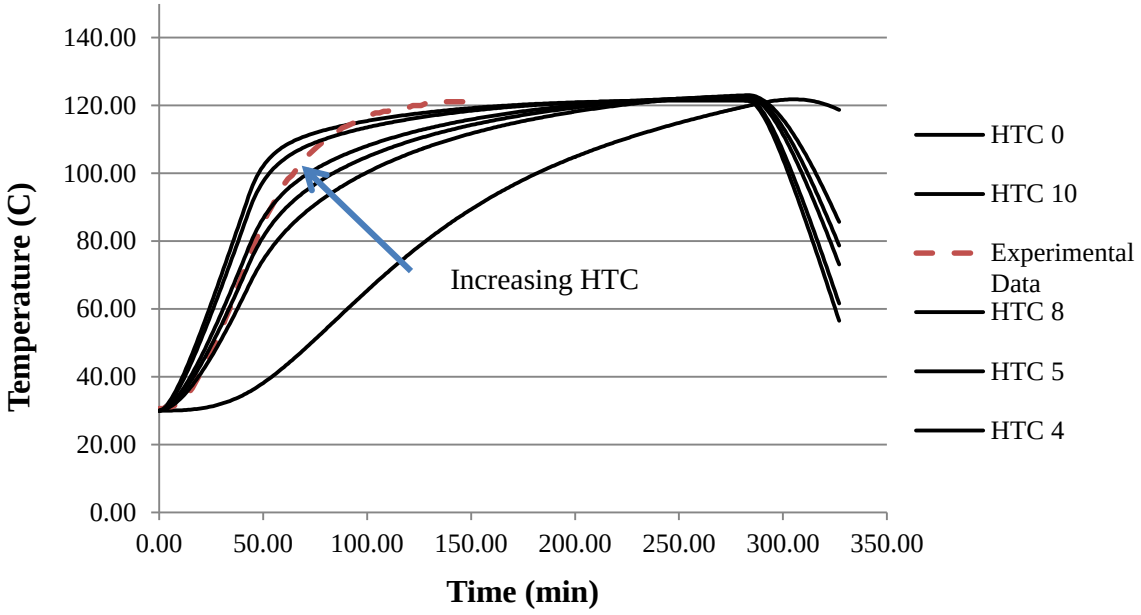

Figure 33. Sensitivity analysis of inside HTC – Middle rib

The study showed a lower HTC value was needed to match the measured data, an HTC value of approximately 2.0 J/sm^{2}K was found to most accurately match measured values. Air circulation in the cellular cores is much lower given the small opening to the autoclave, limiting the efficiency of heat transfer. The low circulation is reflected in the low HTC value required to match the data. This also indicates that heat transfer through the internal rib is not through convection inside the cores, but rather the conduction through the rest of the tooling. A value of 2.0 J/sm^{2}K was used as a new baseline for the HTC inside the cellular cores during the sensitivity analysis study for the outside HTC. After validating the heat transfer inside the tooling, the heat transfer outside the tool was varied incrementally and evaluated based on the same criteria. Figures 34-36 below show the thermal profile at the locations of interest along with the experimental data recorded. The data shows that there is a disparity in the HTC values surrounding the tooling. The bottom surface heats up faster given the small amount of material

located towards the bottom of the part. However, the top joint matched closer to 50.0 or 60.0 J/sm^{2}K, possibly due to the mass of aluminum closer to the top half of the part slowing the temperature. This also supports the theory that airflow in the autoclave is not uniform and more specificity is needed to map the HTC of the outer layer of the tool.

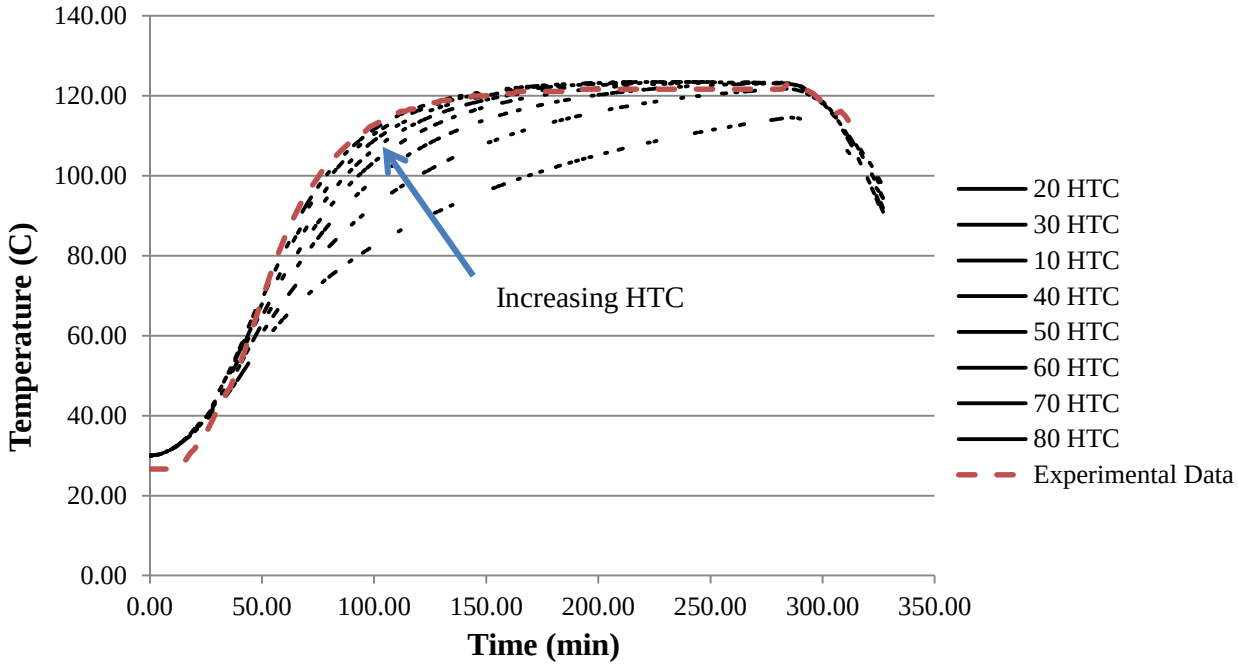

Figure 34. Sensitivity analysis of outside HTC – Bottom Joint

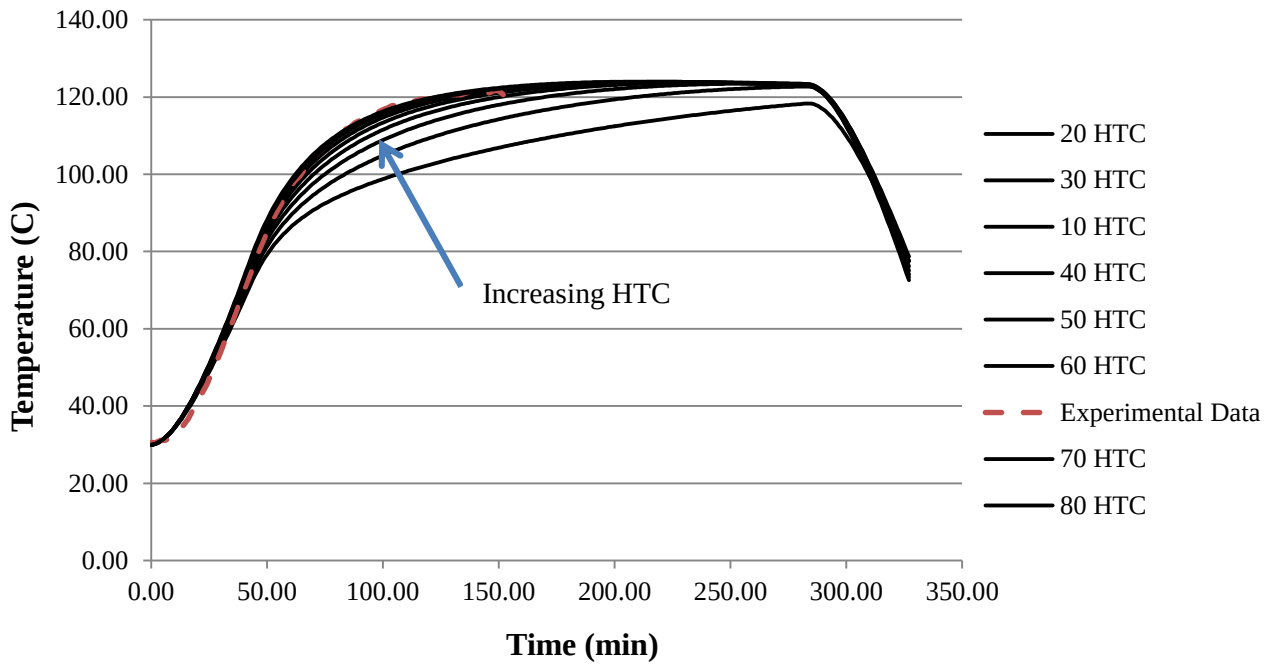

Figure 35. Sensitivity analysis of outside HTC – Middle Rib

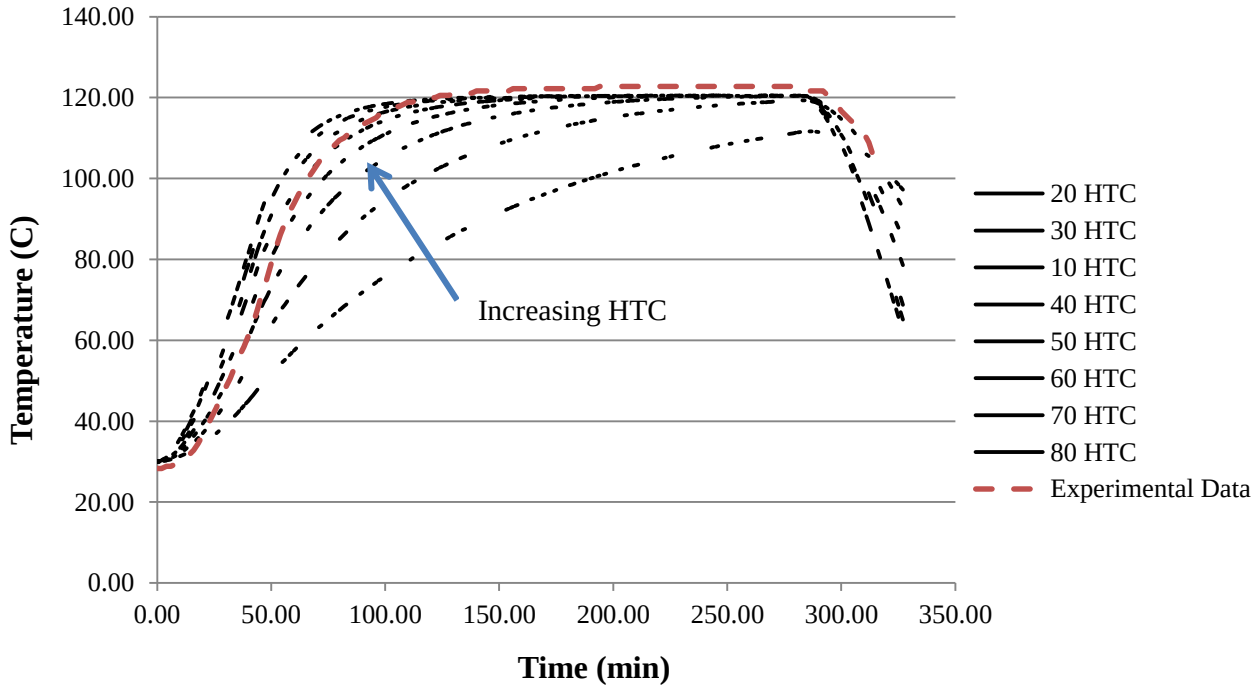

Figure 36. Sensitivity analysis of outside HTC – Top Joint

The non-uniform airflow and heat up indicated that surfaces need to be identified with more precision. The top, bottom and sides were defined as separate surfaces with an HTC of 50.0 J/sm^2K chosen for the top, 40.0 J/sm^2K for the sides and 60.0 J/sm^2K for the bottom as starting points. Sensitivity analyses were run varying the combinations of these values incrementally to find the closest match to the experimental data. Results of these HTC values at the studied locations are shown in the model validation section next.

In addition to the sensitivity analysis performed on the HTC values, a sensitivity analysis was performed on other areas of interest as well. The acetal cores were subject to several tests examining the thermal properties of the cores. The specific heat capacity and thermal conductivity were independently studied at a variety of values to quantify any effect they may have. No difference was found between any of the tests, it was concluded that the range for acetal material properties had a negligible effect on the thermal profile due to the significantly larger mass of the aluminum. The aluminum tooling dictates the heating significantly more than minor changes in the acetal properties especially given the low heat transfer inside the cores. Conduction is taking place through the tooling and into the material quicker than convection into the cores.

3.7.2 Thermal Model Validation

The results of the model show good correlation with experimental data gathered. There were four areas of interest highlighted in figure 25 earlier. The thermal profile of these locations was compared to validate the model and verify that it can be used to predict the degree of cure at

different locations. From the sensitivity analysis the final values for the HTC values were found to be 2.0 W/m^2K inside the cores, 60.0 W/m^2K on the top and sides, and 30.0 W/m^2K on the bottom. Conceptually the low value inside the cores is based on low heat transfer through convection in the cores. The position of the heating elements and fan in the autoclave imply that the top and sides receive a more consistent airflow path which explains why they have a higher HTC. The bottom surface has less room for airflow so the HTC value is not as high, however, the low thermal mass near the bottom also means that despite the low HTC value the bottom heats up at a relatively easily.

The thermal model simulates the heating profile of each node and from that the degree of cure is calculated by the model based on the resin chemistry data imported earlier. The areas of focus can be seen in figures 37, 39, 41, and 43 below followed by the temperature profile at each point. These locations were chosen to gain a full and comprehensive understanding of how the part is heating up. The first area of interest was away from the composite part between the base aluminum tool and the side wedge, this was necessary as a check that there is good mapping throughout the entire tool, not just around the part. The tooling design of the CCT process allows for cores of varying sizes to be used in the same clamshell mold just by replacing the internal tooling components. This design flexibility of the CCT process offers an advantage over other tooling methods, having a comprehensive temperature map not only helps improve the model accuracy but makes future parts easier to integrate into the modeling. Highlighted in the image below is the exact area where measurements were taken. Looking at the graph in Figure 38 good correlation can be seen between the model and the experimental data taken. It is also important to note that the experimental data is consistent within itself, insuring that the autoclave is

performing consistently. The slightly slow start by the model is a design factor built into the model accounting for the pressure increase that generally occurs at the beginning of a cure cycle. During this period in the model there is no change in temperature but in reality the pressure increase does cause an increase in temperature which is seen in the quick initial rise in temperature of the experimental data.

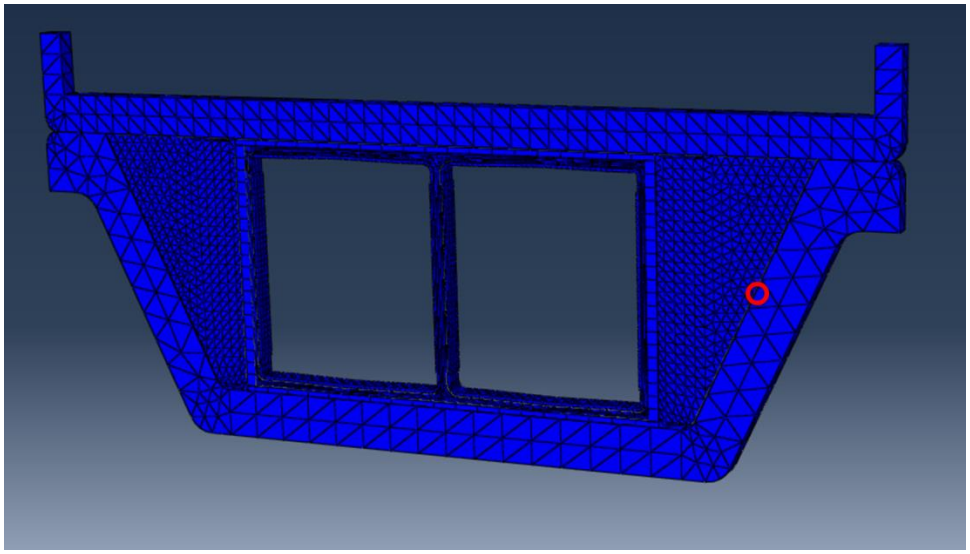

Figure 37. Location of Thermal profile data – Outside aluminum wedge

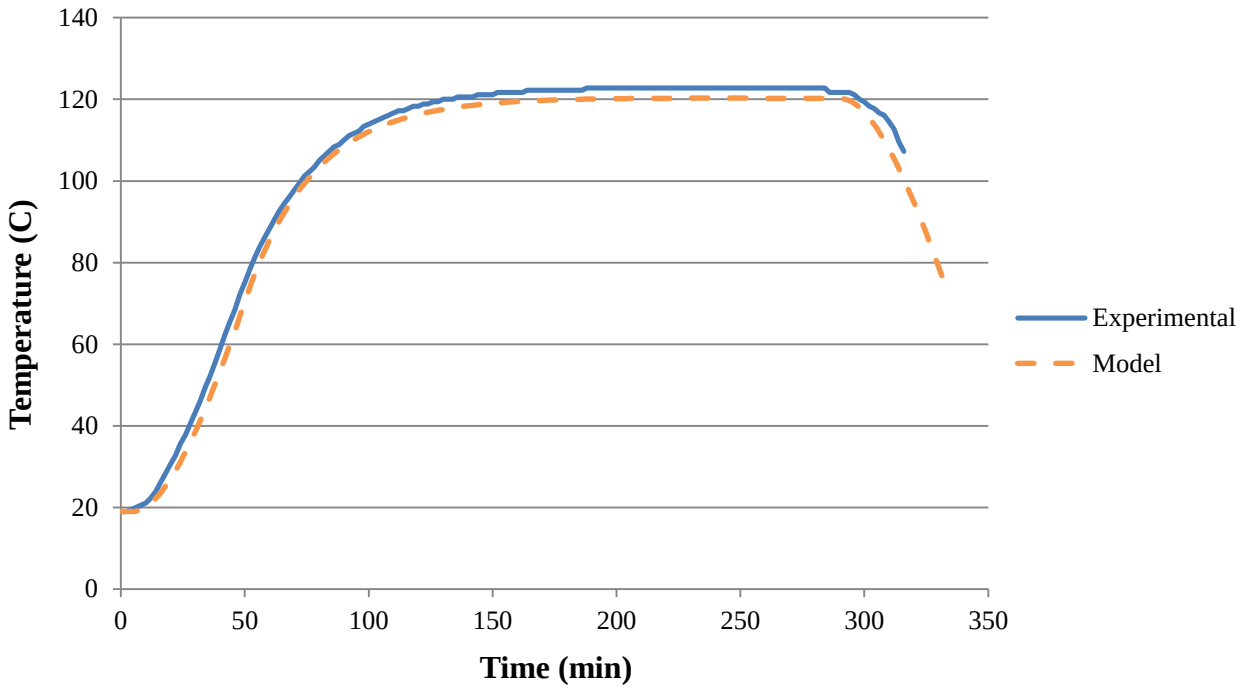

Figure 38. Graph of thermal profile in model and autoclave – Outside aluminum wedge

As can be seen in figure 40 below, the bottom skin of the composite in the model shows good agreement with experimental data, staying within 2 ˚C for most of the cure cycle with the exception of a brief spike during the ramp. As stated earlier the initial start temp in the cure cycle of the model is somewhat arbitrary, 300 seconds was chosen to allow time for the pressure to be applied in the autoclave samples but in actuality that time can fluctuate. What is important to note is the trend between the two graphs is almost identical, which implies a similar cure rate at that location.

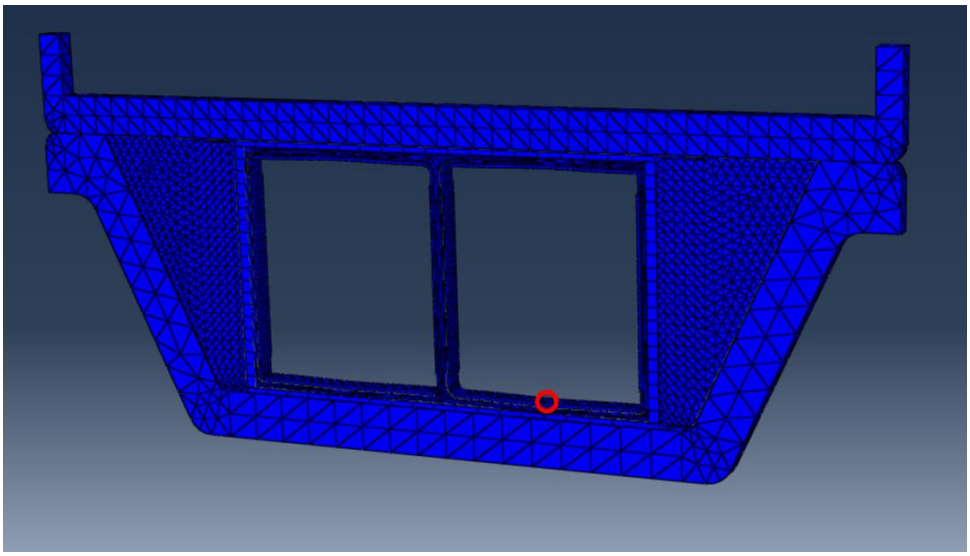

Figure 39. Location of Thermal profile data – Bottom composite skin

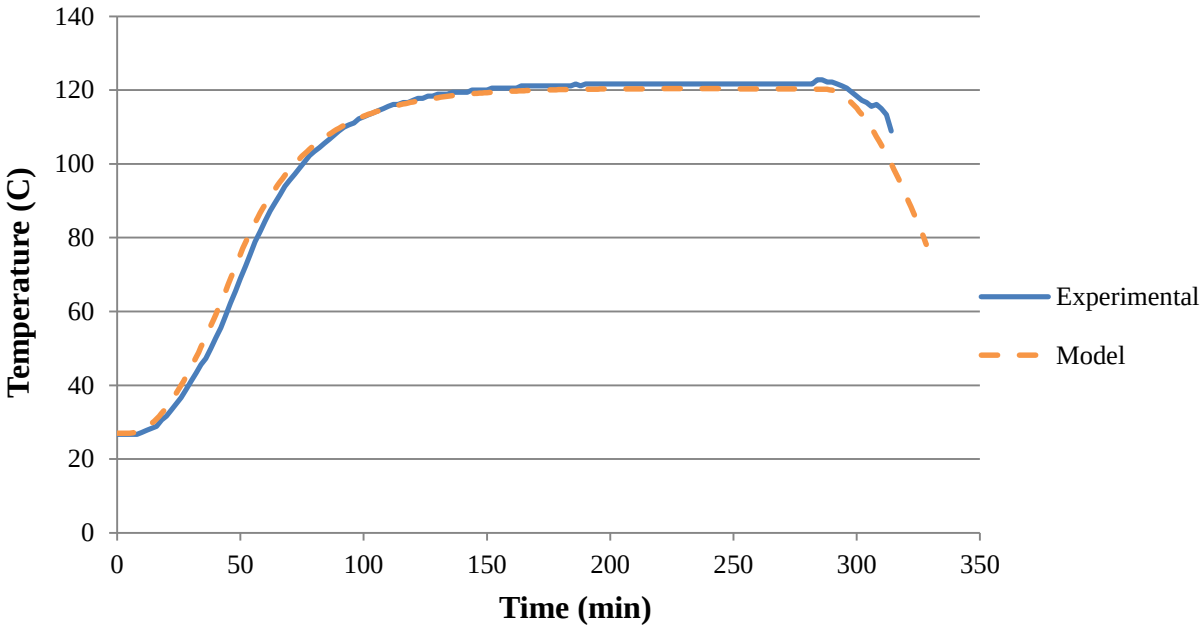

Figure 40. Graph of thermal profile in model and autoclave – Bottom composite skin

The top composite skin shown in figure 42 below also matches well with the rate of the actual data. The model appears to under predict the temperature by 2 to 4 ˚C during the course of the

cure but given the ramp rates are identical it can be assumed the model is behaving close to the experimental data. The consistency at different areas is reassuring that the model is doing an acceptable job of mapping the part.

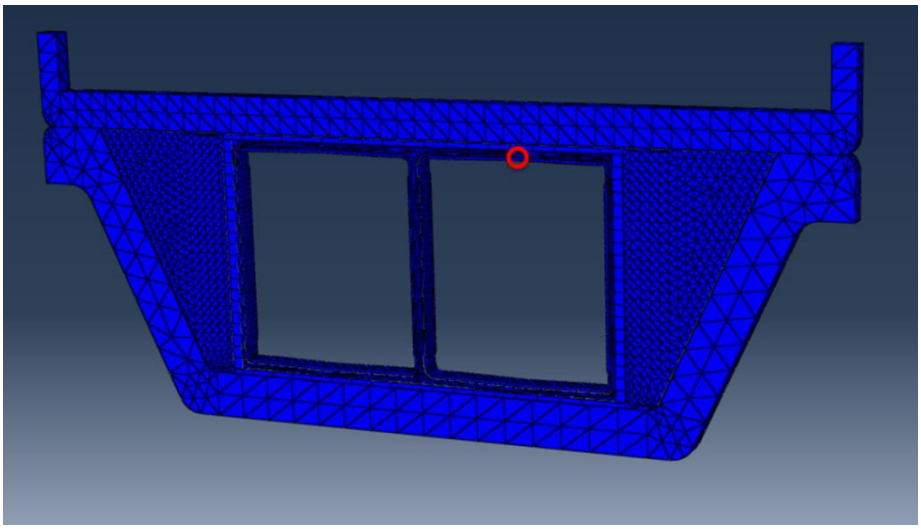

Figure 41. Location of Thermal profile data – Top composite skin

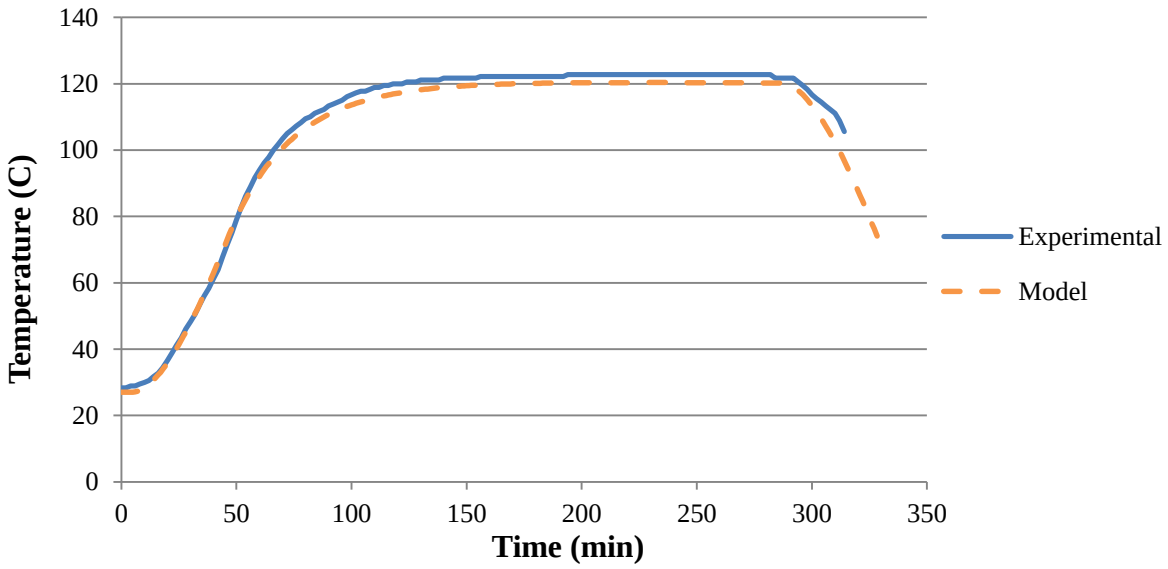

Figure 42. Graph of thermal profile in model and autoclave – Top composite skin

The final area of interest was the middle rib, as can be seen below in figure 44 the results are very similar. The model data shows good agreement to the experimental data throughout the

profile. This is a very encouraging result showing that the bottles can be accurately modelled for manufacturing. There is a small increase in temperature observed in the model during the dwell which could be indicative of an exotherm from the curing epoxy. The model may be assuming the conduction of heat out of the rib is less efficient, trapping heat in the rib as the material exotherms.

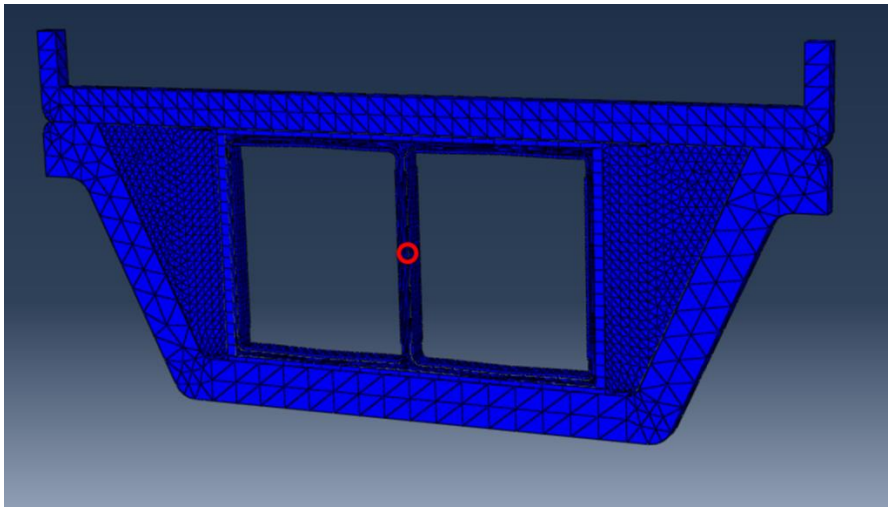

Figure 43. Location of Thermal profile data – Middle composite rib

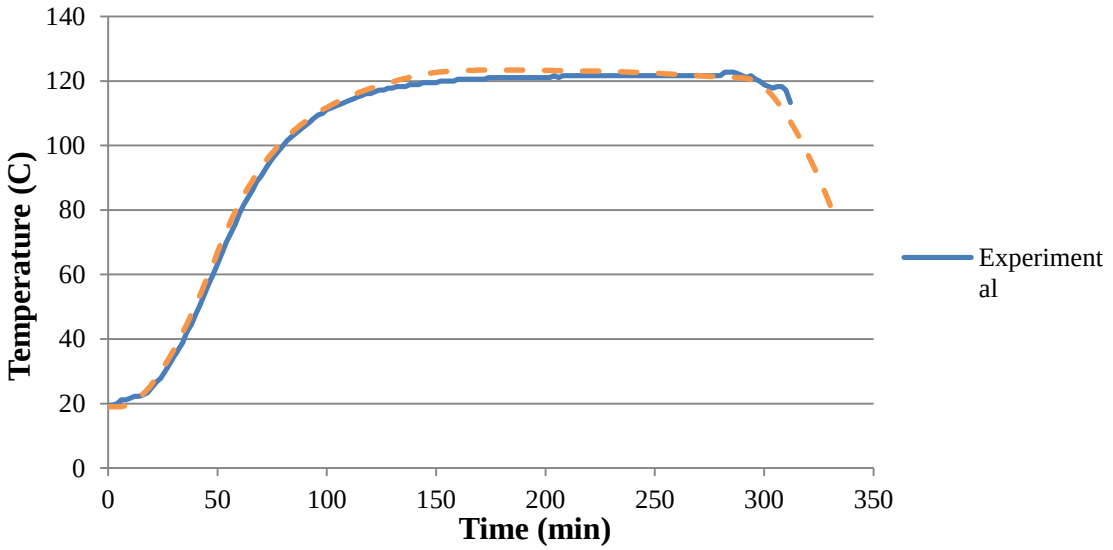

Figure 44. Graph of thermal profile in model and autoclave – Middle composite rib

As stated earlier, a lumped mass calorimeter was used to compare against the sensitivity analysis performed. The top surface was chosen for testing using a thermocouple imbedded into a steel rod. Using equation 19 the HTC at that location can be calculated. This test is discussed in more detail in Appendix B, but the calculation found that an HTC value of approximately 50.0 W/m^2K was sufficient for the top surface, while the sensitivity analysis found that 60.0 W/m^2K was ideal. Given that the value can range from 2-300 W/m^2K this difference was found to be negligible to the effect on the results. The sensitivity analysis showed that minor fluctuations (~10 W/m^2K) on most surfaces did not significantly affect the heating profile. Only when these fluctuations were performed on all the surfaces at the same time did the effects begin to compound and the heating profile would not match the experimental data. The exception to this rule was the inside surface of the cores, where the proximity to the composite would dramatically change the temperature profile.

To quantify the differences observed between the simulations and the experimental data, profiles of the temperature differences throughout the cure were made. Shown below in Figure 45 are the temperature values of the experimental data subtracted from the model data. Overall the model has proven effective at mapping the cure profile and predicting any issues that may arise during the curing of complex shapes.

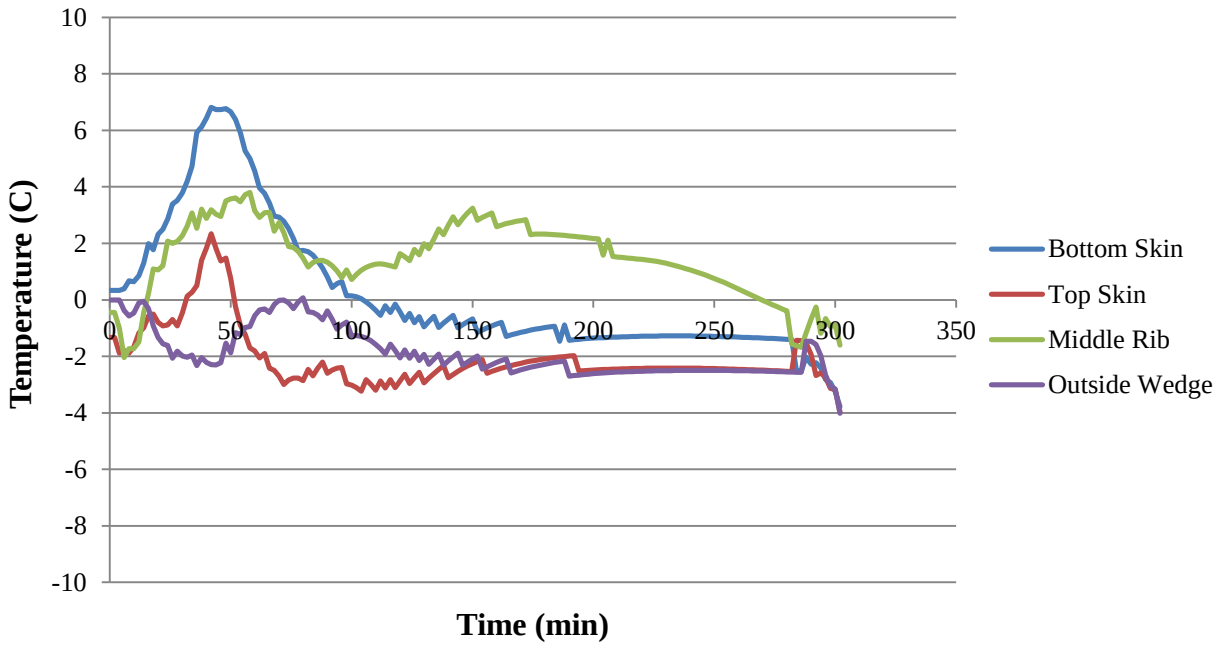

Figure 45. Graph of temperature difference between model and experimental data

3.7.3 Degree of Cure Validation

Differential Scanning Calorimetry (DSC) was observed to have a delicate balance between raising the temperature to a point where all the excess heat was generated without degrading the resin. Thermogravimetric analysis has shown that the degradation temperature is approximately 260˚C so this was set as the maximum allowable temperature. It was found that the ramp rate in the DSC process could significantly change the results; the lower the ramp rate the greater the chance that the maximum exotherm can be produced. Rates of 1˚C/min, 3˚C/min, and 5˚C/min were tested, it was found that 1˚C/min was slow enough that determining the peak became and difficult and 5˚C/min did not allow enough time for the material to exotherm under 260˚C. A rate of 3˚C/min was used to insure maximum heat generation without resin degradation.

The Cycom 5320-1 resin system is a 175˚C curing material, but allows a cure at 120˚C with a post cure at 175˚C. Because of the temperature limitations of the acetal cores the 120˚C cure has been used as previously stated. For model verification purposes the post cure was withheld from the current study affecting the final degree of cure values. This was done for multiple reasons; the melting of the acetal cores above 150˚C meant the post cure would have to be done in a second stage after tool removal which in modeling proved challenging to remove tooling and create a second heating profile. Also data collected from modeling a one stage cure to 176˚C indicated that both the model and experimental data all came within 1% of a 92% cure. In an attempt to see how well the model predicted an intermediate temperature, DSC was performed on samples only cured to 120˚C. Shown below in figure 46 is the predicted degree of cure at the three locations of interest and their progression through the cure. It is difficult to verify the rate of cure experimentally but the final values can be used for comparison.

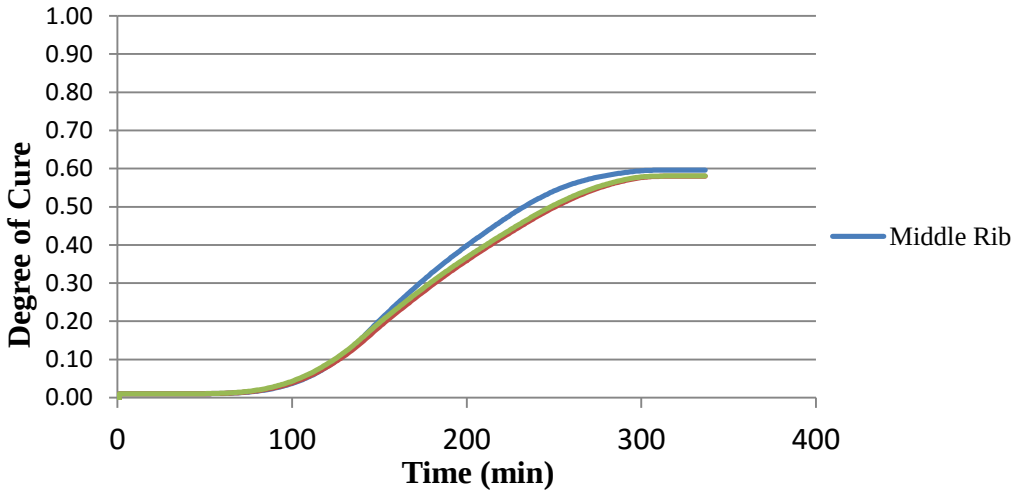

Figure 46. Graph of modeled degree of cure throughout DBB

Table 8 compares the final degree of cure values collected to those measured by the DSC. The data collected shows that the model consistently underestimates the final degree of cure; values are 7 to 17% higher than those measured by DSC. While this data does not show strong support it does not necessarily indicate the model does a poor job of predicting degree of cure. In many cases when modeling is based on data collected from testing the data may not give a comprehensive understanding of the material but work within certain parameters very well. It could be that stopping the model at 120˚C is at the boundary of the range that the material data is accurate.

Table 8. Compiled degree of cure data to 120˚C of CCT model vs. experimental

Specimen Location	Model Degree of Cure	Experimental Degree of Cure	Percent Error
Bottom Skin	58.00%	68.87%	15.78%
Top Skin	58.00%	69.88%	17.00%
Middle Rib	60.00%	64.85%	7.47%

To verify the accuracy of the model and check if the issue may be the low cure temp, the degree of cure of a panel cured directly to 176˚C was found using the same methods stated above and compared to the aluminum tooling model run straight to 176˚C. The aluminum tool model was chosen because of the feasibility in running to 176˚C and the absence of large tooling components as in the CCT model meaning it would more ideally match a flat panel. The data shown in table 9 demonstrates that the model can be used effectively to predict degree of cure. Both the model and a panel cured at 176˚C top out at approximately 92.4% cured.

Table 9. Compiled degree of cure data to 176 ˚C of Al tooling model vs. panel

Specimen Location	Model Degree of Cure	Experimental Degree of Cure	Percent Error
Bottom Skin	92.717%	92.5%	.23%
Top Skin	92.717%	92.5%	.23%
Middle Rib	92.719%	92.5%	.24%

3.8 Summary of Thermal Modeling

Good agreement has been shown between the model and experimental data for temperature prediction. A sensitivity analysis was performed to determine the most accurate HTC values on the surfaces exposed to autoclave temperature. Values of 2.0 J/sm^{2}K for the inside cores, 60.0 J/sm^{2}K for the top and sides, and 30.0 J/sm^{2}K were found to best match the actual autoclave conditions. The degree of cure values did not correlate well when stopped at the intermediate cure, possibly do to limitations in the data file of the material. However, good correlation was found when the cure was run to completion in the model and compared to a panel cured to the final cure temp of 176˚C. With the accuracy of the model demonstrated, the nodal temperature data can now be imported into the stress model for analysis.

Chapter 4: Process-Induced Stress Modeling of CCT

Chapter 4 focuses on the understanding and development of the stress model, using the thermal model as a foundation to build a 3D stress analysis model based around the results of the thermal model. The relatively new development of process modeling with FEA has been applied to complex shapes manufactured with a novel tooling method. It is shown that the COMPRO CCA approach to modeling composite processing can be applied to the CCT process. An understanding of this new processing method is developed from both experimental and modeled results. A model of the aluminum tooling process is built as well for comparison to the CCT process. Samples were also manufactured to compare spring-in angle with the model. Discussion of the measured results is presented and a summary of the conclusions made.

4.1 Mathematical Approach to Stress Analysis

There are several ways to model changing stress/modulus during cure, the behavior of the resin identifies as viscoelastic as curing takes place but these models can be complex. In many cases purely elastic models are used to great effect and require much simpler analyses. Most often there are two methods for determining stress development: incremental laminate plate theory and finite element analysis. Laminate plate theory can be relatively simple to calculate but is restricted to simple shapes. Finite element analyses can be computationally involved but has the capability to handle more complex structures. Detailed below is a general approach using classical laminate plate theory and the information obtained from the mathematical heat transfer analysis for the changing properties during cure.

From the unique thermal profile of a part we can obtain specifics about stress development during the cure. There are several factors that contribute to the final strain within a structure that must be taken into account. The curing of the resin causes a resin densification which will be referred to as chemical shrinkage strain. This is the strain put on the matrix as crosslinking occurs and stress is put on the network by new covalent bonds forming. There is also thermal strain from the changing temperature while the resin is curing and then during cooling. In addition this problem is made more complex by the inclusion of the fiber which are anisotropic; the coefficient of thermal expansion is different parallel and perpendicular to the fibers and with respect to the resin. The order and ply lay-up will also influence the strain; if a laminate is not symmetric warpage will occur due to the mismatch of thermal expansion of the plies around the mid-plane of the laminate. The final part warpage may also be influenced by other factors ranging from the tool-part interaction to the resin viscosity.

One of the first factors that must be considered is the modulus of the resin which is obviously increasing as the cure progresses. The analysis of the changing modulus during autoclave cure has not been studied as extensively as heat transfer through composite materials. The viscoelastic resin modulus is strongly cure dependent and efforts to model this change can be system specific; working only with simple shapes and within controlled boundaries. One method proposed by Bogetti and Gillespie[19] (1990) models the changing resin modulus as a function of the degree of cure as described below in equation 21.

Eq. 21 $E_m = (1-\alpha)E_m^0 + \alpha E_m^\infty + \gamma\alpha(1-\alpha)(E_m^\infty - E_m^0)$ where $-1 < \gamma < 1$

Where E_m^0 is the uncured resin modulus, E_m^∞ is the fully cured modulus, and γ is a term included to quantify the competing mechanisms between the stress relaxation and chemical hardening. In many cases γ is assumed to be equal to 0 and makes the relationship linear[35]. The resin modulus is only part of the information required to understand residual stress. The transverse modulus within a ply is obviously highly dependent on the resin modulus but in the longitudinal direction the fibers play a significant role. In addition if the resin is assumed to be viscoelastic there is some stress relaxation as the material cools. These must also be considered and incrementally calculated when determining final stress values.

To account for the chemical shrinkage strain within a given volume of resin, the incremental change in a specific volume of resin can be calculated from the incremental change in length of the three principle directions. This is then related to the strain in the principle directions to determine the volumetric shrinkage strain by the following equation developed by Bogetti and Gillespie (1990)[19].

Eq. 22 $$\Delta\epsilon_r = \sqrt[3]{1 + \Delta v_r} - 1$$

Eq. 23 $$\Delta v_r = \Delta\alpha \cdot v_{sh}^T$$

In these equations $\Delta\epsilon_r$ is the incremental isotropic shrinkage strain, Δv_r is the incremental specific volume shrinkage, $\Delta\alpha$ is the incremental change in degree of cure, and v_{sh}^T is the total specific volume change of the cured resin.

The cure dependent composite mechanical properties are the next area that must be discussed. The changing resin modulus has already been covered but in order to obtain an accurate representation of the lamina properties in all directions the fibers must be included. Assuming Poisson's ratio for the resin (v_m) is constant, the resin shear modulus (G_m) and the bulk modulus (k) can be determined from the following relationships.

Eq. 24 $$G_m = \frac{E_m}{2(1+v_m)}$$

Eq. 25 $$k = \frac{E}{2(1 - v - 2v^2)}$$

In addition to the shear modulus and the bulk modulus of the materials, other engineering constants are required for the properties of the lamina to calculate the stress. The lamina modulus (E) can be described by the mathematical expressions given in Appendix F for the primary fiber direction (1) and the transverse directions (2 and 3). The shear modulus and Poisson's ratio for the lamina can also be calculated from the constituent material properties, fiber volume fraction (V_f), and the mechanical relationships. The incremental in plane thermal expansion strains are computed by the following relationship between the change in temperature and the thermal expansion coefficients parallel and perpendicular to the fibers.

Eq. 26 $$\Delta\epsilon_1^{th} = \alpha_1 \cdot \Delta T$$

Eq. 27 $$\Delta\epsilon_2^{th} = \alpha_2 \cdot \Delta T$$

Eq. 28 $$\alpha_1 = \frac{\alpha_{1f}E_{1f}V_f + \alpha_{1m}E_{1m}(1 - V_f)}{E_{1f}V_f + E_{1m}(1 - V_f)}$$

Eq. 29 $\alpha_2 = \alpha_3 = (\alpha_{2f} + v_{12f}\alpha_{1f})V_f + (\alpha_{2m} + v_{12m}\alpha_{1m})(1 - V_f) - [v_{12f}V_f + v_{12m}(1 - V_f)]\left[\frac{\alpha_{1f}E_{1f}V_f + \alpha_{1m}E_{1m}(1 - V_f)}{E_{1f}V_f + E_{1m}(1 - V_f)}\right]$

Coupled with equations 22 and 23 the total processed induced strain from thermal expansion and chemical shrinkage can be determined[19].

Eq. 30 $\Delta\epsilon_1^T = \Delta\epsilon_1^{th} + \Delta\epsilon_1^{ch}$

Eq. 31 $\Delta\epsilon_2^T = \Delta\epsilon_2^{th} + \Delta\epsilon_2^{ch}$

Using classical laminated plate theory the laminate strains can be determined from the lamina strain increments found above. The force (N) and moment (M) resultants can be found from the incremental ply strains in the global coordinate system and the [Q] matrix as shown in the appendices. From there using the laminate compliance coefficients $\left(\begin{bmatrix} A & D \\ D & B \end{bmatrix} \text{ matrix}\right)$ the laminate strains and curvatures can be determined ($\Delta\epsilon_x^\circ$, $\Delta\epsilon_y^\circ$, $\Delta\epsilon_{xy}^\circ$, Δk_x, Δk_y, Δk_{xy}). The laminate ply strains are then calculated by the following equations with z_k representing the distance from the mid-plane to the kth ply. More detail is given in the appendices on the transformation from local lamina strains to global coordinate laminate strains.

Eq. 32 $\Delta\epsilon_x = \Delta\epsilon_x^\circ + z_k\Delta k_x$

Eq. 33 $\Delta\epsilon_y = \Delta\epsilon_y^\circ + z_k\Delta k_y$

Eq. 34 $\Delta\epsilon_{xy} = \Delta\epsilon_{xy}^\circ + z_k\Delta k_{xy}$

The laminate ply strains can be related to the incremental ply stress ($\Delta\sigma$) by the transformed [Q] matrix and the difference between the laminate ply strains and the stress-free process induced ply strains[19].

Eq. 35 $$\Delta\sigma_x^k = Q_{11}^{-k}(\Delta\epsilon_x - \Delta\epsilon_x^T)^k + Q_{12}^{-k}\left(\Delta\epsilon_y - \Delta\epsilon_y^T\right)^k + Q_{16}^{-k}\left(\Delta\epsilon_{xy} - \Delta\epsilon_{xy}^T\right)^k$$

Eq. 36 $$\Delta\sigma_y^k = Q_{12}^{-k}(\Delta\epsilon_x - \Delta\epsilon_x^T)^k + Q_{22}^{-k}\left(\Delta\epsilon_y - \Delta\epsilon_y^T\right)^k + Q_{26}^{-k}\left(\Delta\epsilon_{xy} - \Delta\epsilon_{xy}^T\right)^k$$

Eq. 37 $$\Delta\sigma_{xy}^k = Q_{16}^{-k}(\Delta\epsilon_x - \Delta\epsilon_x^T)^k + Q_{26}^{-k}\left(\Delta\epsilon_y - \Delta\epsilon_y^T\right)^k + Q_{66}^{-k}\left(\Delta\epsilon_{xy} - \Delta\epsilon_{xy}^T\right)^k$$

This method while not difficult to perform computationally on simple shapes becomes incredibly challenging for complex structures. Finite Element Analysis (FEA) has been used in some studies for modeling complex composite structures. However the complexity of process induced stress and finite element analysis has led to very few studies which use FEA to determine process-induced residual stress in complex composite structures[23].

4.2 COMRO CCA – CCT Stress Model

The part and mesh of the thermal model are used as the foundation for building the stress model. This is helpful for matching the node positions to the result file obtained from the thermal analysis. The output file from the thermal analysis records the temperature at each numbered node with respect to time, by using the same parts and mesh is can be assured that the mesh will match and the data transferred. Because of this, if any other changes were made to the part design, they were first made to the thermal analysis and a new output file created for coherency between the output files and stress model. The same material is used for the stress model because

of its alternate cure cycle allowing use with the cores. This material however, has not been characterized for resin flow analysis. It has been assumed that the system is net resin and the cured ply thickness has been used as a baseline for the ply thickness in the values. It is important to make this assumption in the model because of the 3D stress elements used; there will not be significant change in thickness during the stress analysis.

For the stress analysis, greater specificity is needed in regards to the material orientation of the composite due to the alignment of the fibers. Distinct material orientations were assigned to each of the composite plies to account for the anisotropy and varying orientations used in the lay-up. A discrete orientation was used through the part to identify the stacking and fiber directions regardless of changes in the geometry. The structure was partitioned into separate rectangular and cylindrical sections to help identify these different areas. The composite sectioning tool was assigned to each partition and a ply definition created with respect to the local material orientation used. The ply definition also becomes more involved as the in-plane fiber orientation must be specified. The material used for the experimental samples was a woven fabric in +/- 45 and 0/90 orientations, however the material data files are only written for unidirectional tape. In order to approximate a weave pattern, within one element thickness (one ply) a lay-up stack was written with either [45/-45/-45/45] or [0/90/90/0] depending on the weave orientation. This approximates one ply of fabric as four, quarter thickness tape plies. It is important when using this technique to make a single ply symmetric about its mid-plane to avoid warping.

Two element types were tested in the stress analysis, 3D quadratic stress elements (C3D20), and an 8 node linear brick element (C3D8I). C3D20 is a general quadratic brick element for use in

linear elastic problems. The high number of nodes in the brick helps capture stress concentrations at surfaces. In some cases including bending, quadratic brick elements can be too stiff to capture bending so linear brick elements are used instead. The C3D8I linear brick element is standard element for use in bending potentially capturing spring-in angle. Incompatible modes are an addition to standard C3D8 elements that adds more capability in bending by some of the shear stresses associated with displacement elements. In both cases the elements were compatible with the thermal analysis performed previously.

Material files were expanded to include mechanical properties. In most cases the data was already provided by Convergent Manufacturing Technologies or The Boeing Company. The mechanical property data for the acetal cores was taken from a combination of testing and literature. The modulus and Poisson's ratio were the only values to be considered with temperature dependency. A rough curve for the temperature dependence of the modulus and Poisson's ratio were built from literature data to represent the changing properties of the thermoplastic as the part was heated. However, an early sensitivity analysis revealed that incorporating the temperature dependence of these properties into the model did not significantly affect the results.

Interactions between surfaces become more complex during the stress analysis and most are switched from a tie constraint to a surface interaction property which incorporates friction. In some cases the model limits the use of this surface interaction so surfaces were left as tie constraints but in those cases sliding between surfaces was assumed negligible. A friction coefficient of 0.15 was used between composite and steel surfaces with a shear stress limit of

27,500 MPa. Between steel surfaces a friction coefficient of 0.2 was used and between steel and aluminum a value of 0.6 was used based on literature data. Early sensitivity analyses indicated that small variance in these values did not impact the results of the model.

Boundary conditions were placed on the model to fix the tooling in space. Two planes were created on the global X and Y axis and in line with the rib and skin of the composite for which motion in the Y and X directions was restricted respectively. The front face of the part and tooling was restricted in the Z direction so that expansion only occurs in one direction. This method creates a point at the middle of the rib on one face that is restricted in all directions and acts as a fixed location. One the cure had run to completion a tool removal step is performed and the boundary conditions altered to all free spring-in of the skins. Figure 47 below shows the final boundary condition set-up used to allow unrestricted warpage in the model after tooling was removed.

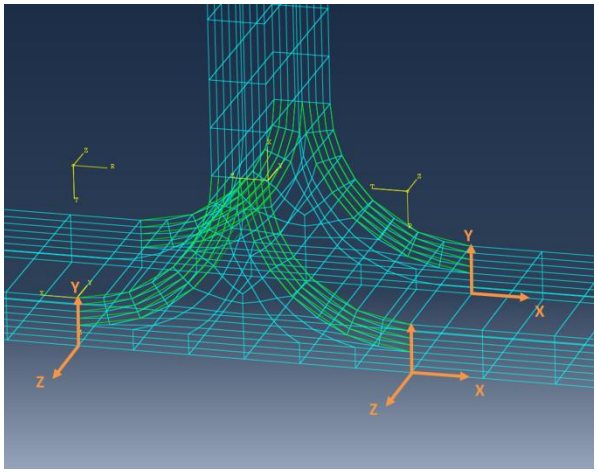

Figure 47. Boundary conditions at the end of simulation to allow warpage

Autoclave pressure was added to the load module following the ramp in the autoclave which ramps to 90 psi and holds for the duration of the cure. The thermal data from the heat transfer analysis was added as a predefined field for the main analysis step during the stress model. A new step was added after the main stress analysis step called the “Tool Removal” step where the tooling elements are removed allowing deformation to take place. In most cases the elements at the ends of the double box beam were also removed so that the final structure was an I-beam. This allows the skin plies to spring-in unconstrained and the spring in angle to be measured. The spring-in angle was measured at all four locations shown in figure 48 and compared to experimental samples.

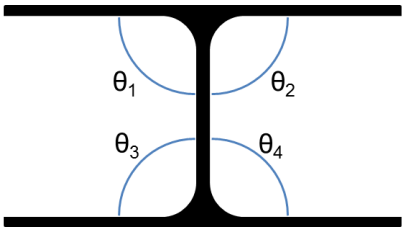

Figure 48. Image of locations of spring-in measurement

In addition to measuring spring-in, the model was designed to output stress (S), strain (E), position, and displacement at each node.

4.2.1 COMRO CCA – Aluminum Stress Model

The aluminum tooling model was developed using the same approach. Using the thermal model as a baseline the elements were changed to 3D stress elements to insure compatibility. The same boundary condition approach was used as in the CCT model, fixing the mid-planes in the X and

Y directions and the front face of the cross section in the Z direction. As with the CCT model, because no resin flow model was developed it is assumed that the systems are net resin and there is no resin lost during cure. The initial fiber volume fraction is established in the material data file and does not change.

The interaction between the aluminum and composite is defined as above, in addition separation between the composite and aluminum was not allowed after contact. The justification for this is that while release agents are used between the tool and composite interface, the materials tend to adhere during cure and must be pried off. This does not affect the ability of the material to slide, the same friction coefficients are in place as with the CCT mode.

4.3 Experimental Spring-In Approach

To obtain high accuracy spring-in angles of experimental samples, a Brown & Sharpe Gage 2000 series measurement machine for precision coordinates was used. This device uses a probe to measure the geometry of a structure by locating points in space and assigning coordinates to those points. These coordinates can be used to create planes and the angles between planes calculated. The probe was used to identify points on each surface of the inside skins and ribs and define them as planes, from these planes the angles between the surfaces were calculated to high accuracy. Show below in figure 49 is the equipment used for this testing. 10 locations were used to map each surface and create the planes; from these planes the angles between them were calculated.

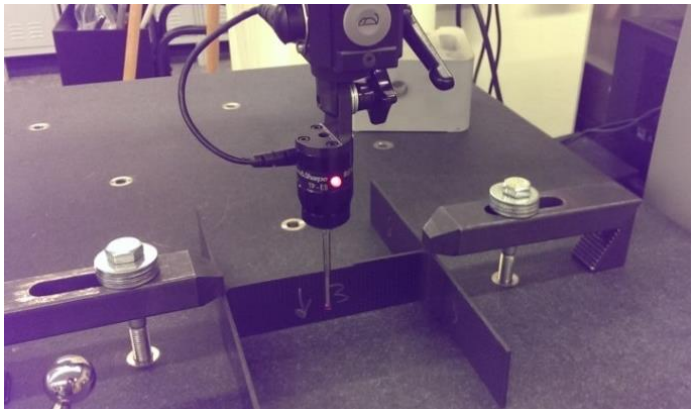

Figure 49. Image of Precision Coordinate Machine

Shown below in figure 50 are the spread of locations tested using the CMM. Two rows of five were tested at equal intervals along on the ribs and skin of both sides of the rib and all four of the inside skin surfaces. Three I-beams were tested for each processing method for comparison.

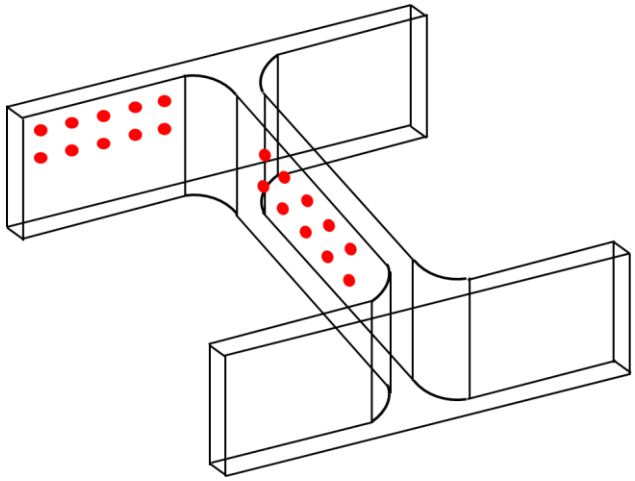

Figure 50. Sample locations for CMM measurements on rib and skin surfaces

4.4 Discussion of Results

The stress model was evaluated on the basis of accuracy of spring-in angle to identical parts manufactured from the CCT process and aluminum tooling. After proving the accuracy, comparisons were made between the CCT process and the aluminum tooling by close examination of stress in the model, specifically looking at contact pressure, and out of plane stress (S33) which can have a strong influence factors such as consolidation and lead to buckling. The hope is that differences between the two processing methods that show up in the models and correlate to differences observed in the actual parts.

4.4.1 Spring-In Comparison

After the tool removal stage in the simulation the double box beam is sectioned into an I-beam by removing the ends. This allows processing stresses to resolve as deformation in the form of spring-in. Spring-in angle has been used to measure differences between the cellular core tooling and aluminum tooling methods. The spring-in is also compared to model predictions to verify the accuracy of the model. In addition to the stress model simulating the CCT process, a stress model was developed for the aluminum tooling method used for comparison. The spring-in angle was taken from all four locations as shown in figure 41 and averaged.

When calculating the spring-in angles in the model, a vector was created along the length of the plane and likewise for the comparison plane. The angle between these vectors was found by taking the inverse cosine function of the dot product for the two vectors, this approach is

demonstrated in figure 51. This approach gives an approximate solution to the surfaces, if single points are used more variance in location was observed making the calculation vary significantly.

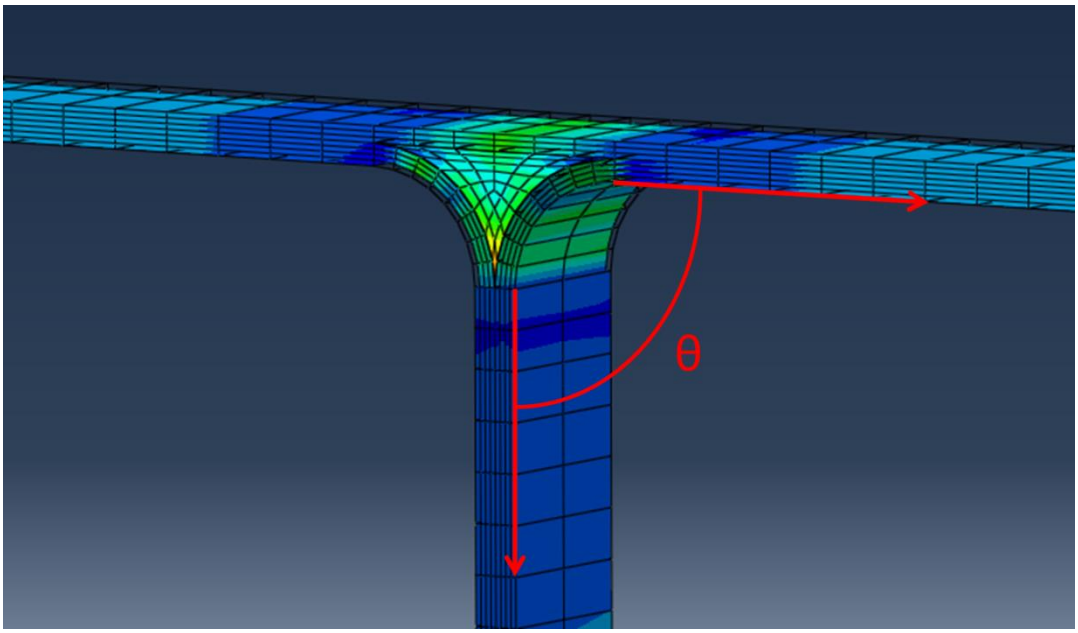

Figure 51. Spring-in angle approach

Using the CMM points were taken from the experimental samples and mapped in space. A representative plot of the coordinates measured by the probe is shown in figure 52. Using this technique the angle between the respective planes can be found and compared to the modeled spring-in.

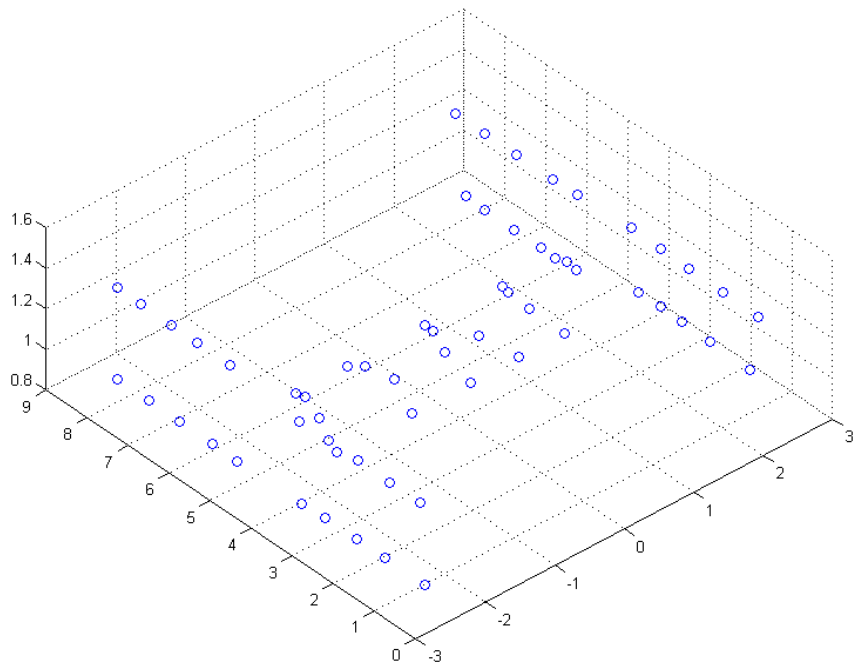

Figure 52. 3-D plot of CMM measurements taken from experimental samples

Table 10 shows the results of the measurements in both the model and experimental samples. The high variation in experimental samples was expected but makes data interpretation difficult. The spring-in values for the model are lower than the expected values, however the high standard deviation in the experimental samples makes proving the model accuracy challenging.

Table 10. Compiled Spring-in Data

Processing Method	Method	Average Angle	St. Dev.
Al Tool	Experimental	89.6815	0.4089
	Model	89.9999	0.0088
CCT	Experimental	89.5440	0.3873
	Model	89.9999	0.0165

The CCT model shows decent correlation to the observed angle despite the high variance in the experimental data. Both models are just near the standard deviation of the observed data but it is difficult to know precisely how accurate the models given the experimental data. The similar spring-in values between the two processing methods indicate that potential spring-in may not attributed to the process method but more from other factors such as the ply lay-up.

While examining the spring-in angles measured in the experimental samples it was found that there was a trend in degree of spring-in. Complimentary angles on the same side of the rib tended to show significantly more spring-in on only one of the two angles. When tracking this observation a better understanding of the warpage developed during processing can be seen. Table 11 below shows the two complimentary angles broken down into separate values to show the difference observed.

Table 11. Complimentary Spring-in angles

Processing Method	Angle	Average Angle	St. Dev.
Al Tool	Small theta	89.3077	0.0765
	Large theta	90.0553	0.1635
CCT	Small theta	89.2324	0.1587
	Large theta	89.9386	0.0744

The two complimentary angles are connected by the skin plies that run along the outside surfaces, restricting the spring-in between the angles. In production parts are not perfectly symmetric, leading to uneven residual stress and more warpage. In the case of angled laminates connected by flat skin plies the spring-in will preferentially lean towards one of the angles and pull the opposing angle apart. This effect is difficult to address in the model as the model behaves ideally and spring-in is displayed symmetrically.

In addition to the uneven spring-in observed in the samples a check was made on the aluminum tooling to determine how precise the angle around the joint was. The thermoplastic tooling used in the CCT process does not allow for accurate measurements to be made due to the flexibility of the material. Using the same technique taken for the measurement of the spring-in angle measurements, the CMM was used to create planes by mapping points along on the aluminum tooling. It was found that there was warping in the tool with one angle measuring at 90.2661 and one measuring 89.1046. When these two tooling pieces are butted against each other it creates a slightly skewed rib and explains the high difference observed in the samples. An exaggeration of this phenomenon is shown in figure 53.

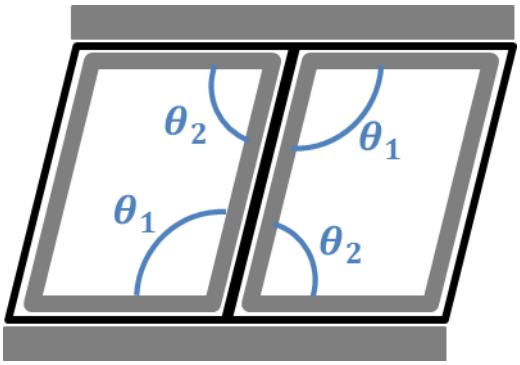

Figure 53. Representation of the effect of tool warpage

During the analysis it was found that a curvature existed in the skin plies. Figure 54 shows that most of the curvature occurs near the joint and radius, indicating that the warpage may be more influenced by geometry than ply lay-up.

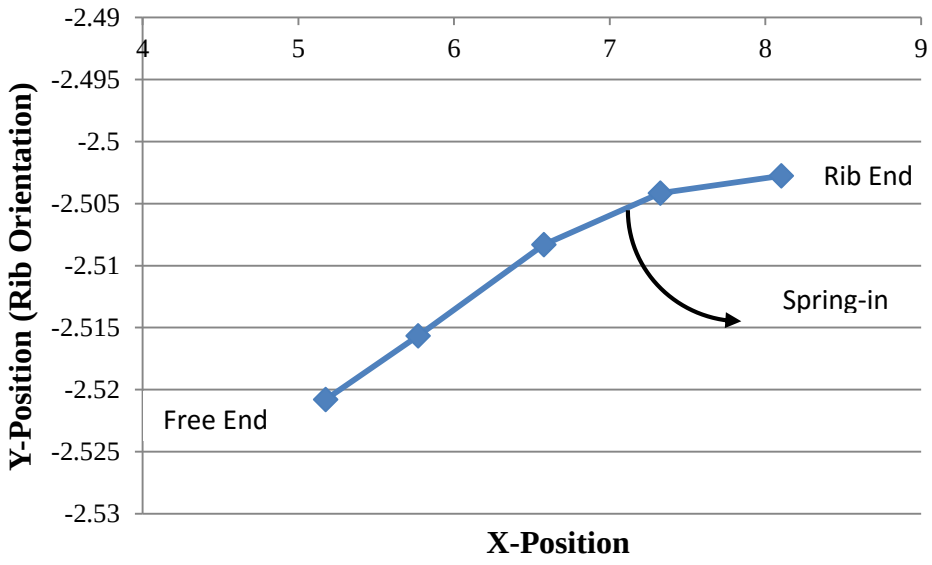

Figure 54. Curvature measure in sample processed with aluminum tooling

The CCT model was adjusted to accommodate 0/90 plies in the wrap and a spring angle of .0002 was observed. While greater than the original CCT model the value is still negligible. Possibly due to the symmetry in the lay-up, the 0/90 wrap plies put more force on the skin plies and pulling the skin down towards the rib more than +/- 45 plies would. However, it can be concluded that the model is doing a reasonable job of matching the actual data allowing further investigation into the processing differences.

4.4.2 Stress Analysis

Differences between the two processing methods were studied to assess the benefits and drawbacks to each approach. The models were also compared with actual parts to determine if these differences would show up experimentally. The method by which each process consolidates the composite is very different. The CCT method relies on heat transfer from the

outside surface and pressure from within the cores to consolidate the plies, whereas the aluminum tooled sample relies on external pressure, but has a potentially strong contribution from the internal expansion of the aluminum when heated. The presence of the internal aluminum tooling in one processing method and the direction of pressure are the primary differences between these methods that will be studied for comparison. There are several ways to identify differences in the models including directional stress (S11, S22, S33), contact forces, pressure, and strain (E11, E22, E33). The S33 stresses and E33 strains specifically can be useful at determining the through thickness variations throughout a part. The contact pressure is another valuable tool that will be used to understand how the tooling interacts with the composite surfaces. From the contact pressure the through thickness stress and strains can be observed to see how the pressure translates to stress in the composite.

Contact pressure was examined in both processing methods for differences. It was found that notable differences in pressure were observed in the middle rib in both cases. Figure 55 shows the contact pressure in the middle ribs of both processing methods with a higher variance seen in the sample processed with aluminum tooling. This contour plot of the contact pressure was taken as the temperature in the middle rib approached the hold temp which corresponds to the gel point of the resin. This timing matches with when residual stress begins to form as crosslinking has started to occur.

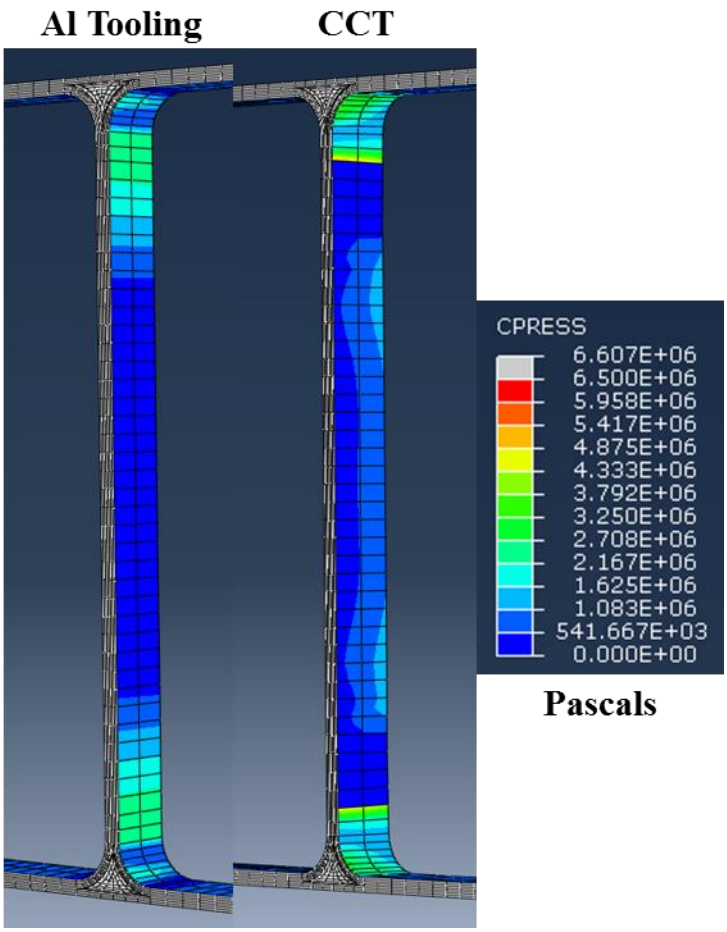

Figure 55. Contact pressure distribution on the middle rib at gel point in both processing methods

This observation agrees with the expected differences between the two processing methods. The application of pressure in the aluminum case acts on the outside surfaces, the pressure from the sides does not get evenly distributed on the middle rib but instead transferred through the tooling. The tooling adjacent to the middle rib is allowed to flex causing it to pull away from the composite rib putting less pressure on the composite which shows up in the contact pressure distribution. The pressure from inside the cellular cores makes the contact pressure higher inside the middle rib. As a check to validate that the contour plot is not just a phenomenon observed in

the model, the thickness in the middle rib is shown to demonstrate the variation seen in the sample processed with aluminum tooling. Figure 56 below shows the thickness variation observed, the sample processed with the aluminum square tubing had significantly higher variation, in agreement with the model predictions. In the case of the CCT this variation was not seen in the thickness, indicating a more even contact pressure. As mentioned previously, the thickness in the stress model cannot be used to directly check the thickness of the parts, that phenomenon is observed during a flow analysis. In a stress model the thickness can be inferred from variations in pressure and checked against experimental samples.

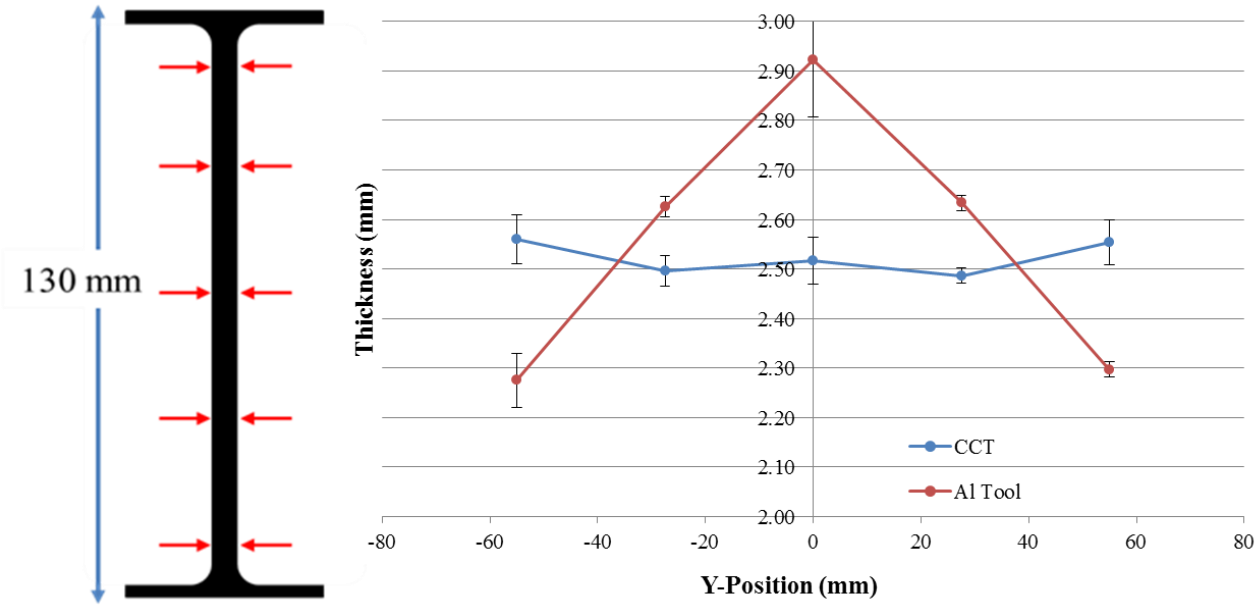

Figure 56. Measured thickness variation along middle rib

The center and edge of the middle rib were chosen for closer examination of stress and strain, these nodes studied are shown below in figure 57. It was shown that differences exist between the two regions so areas close to the joint and in the middle of the rib were chosen for study.

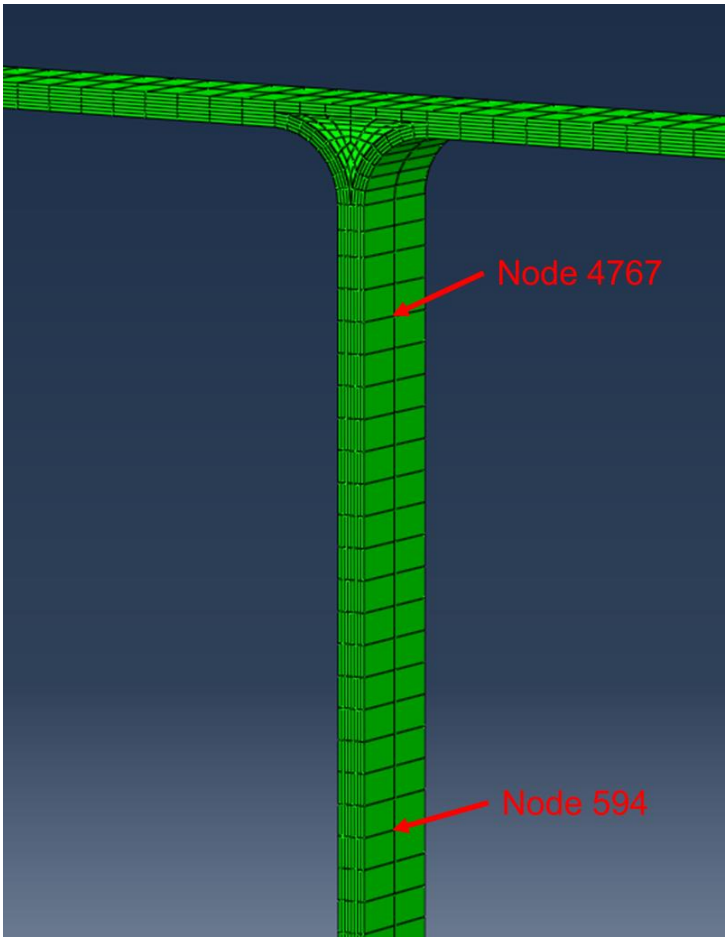

Figure 57. Image of node locations for closer study

A large disparity was observed in the through thickness stress in the rib at the two locations of interest shown in figure 58. The stress close to the joint in the aluminum processed sample is considerably higher than any other location or any stress in the CCT process. The CCT process shows approximately a quarter of the stress of the aluminum tooled part. There is also a large discrepancy between the two locations in the aluminum sample, the node in the middle of the rib was essentially no stress placed on it. As mentioned previously, this region relies on the stiffness of the aluminum tooling to translate force from the outside surfaces of the tooling into the middle

rib. However, this appears to flex enough to decrease the stress on the composite towards the center of the rib. In contrast, the CCT process shows similar behavior between the two locations, possible indicating similar consolidation at the two locations and throughout the rib.

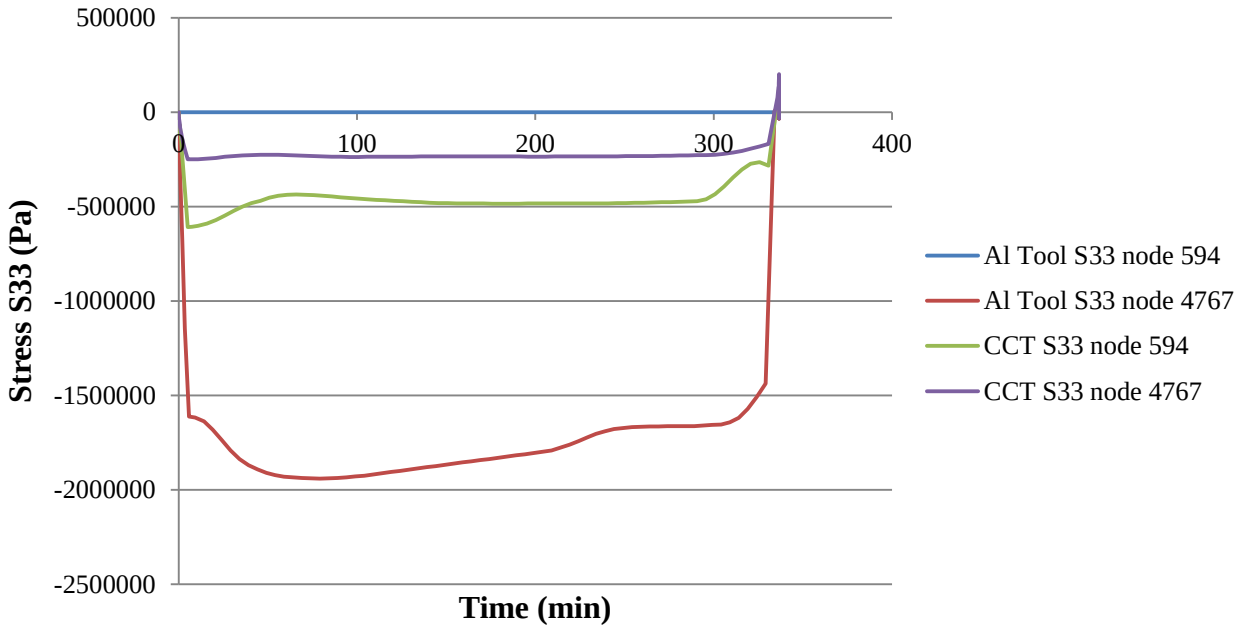

Figure 58. Graph of rib node stress (S33) profiles

The role of thermal expansion should be discussed as well. The aluminum tooling has a high coefficient of thermal expansion and this expansion along the lengths of the tooling put pressure on the joints, as this expansion occurs the tooling is restricted vertically by the composite and the top and bottom skin tools. This expansion coupled with the restriction on the tooling will cause bowing of the vertical lengths in the tool.

The areas with varying through thickness stresses may resolve as variations in resin content, warpage, or changing thickness throughout a part. These locations are susceptible to failure due

to stress concentrations or resin starved areas that cause fiber buckling. To examine this closer the E33 strain values are shown below in figure 59.

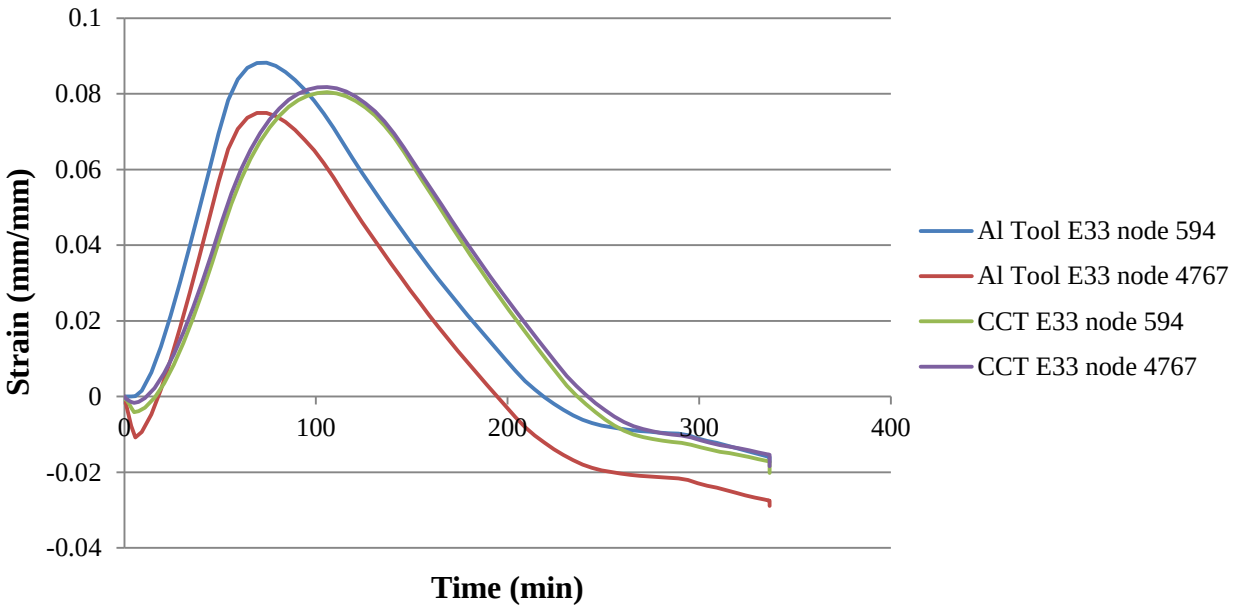

Figure 59. Graph of rib node strain (E33) profiles

In this graph compressive strain is represented as negative strain which can be seen in the profile of nodes at the beginning when pressure is applied to the parts. As the parts expand and contract during the cure cycle the strain becomes positive before fall back to negative. The aluminum tooled sample shows higher through thickness strains at the edges and lower strains in the middle of the rib as expected. The large disparity matches with the observed through thickness stress and contact pressure. The CCT process demonstrates a more even stress and strain on the composite rib throughout the cure cycle. The final strain position in the aluminum tool sample node 4767 shows more compression than the other regions in both processing methods, once again validating the model accuracy with respect to the measured thickness values.

Continuing this study of variations in contact pressure, significant differences were seen in the radii of the joints. As shown in figures 60 and 61, the aluminum tooling method has a region of more localized compressive force at the center of the radius while the CCT process applies pressure to the entire joint. Once again these images are taken during the onset of vitrification when residual stress can develop.

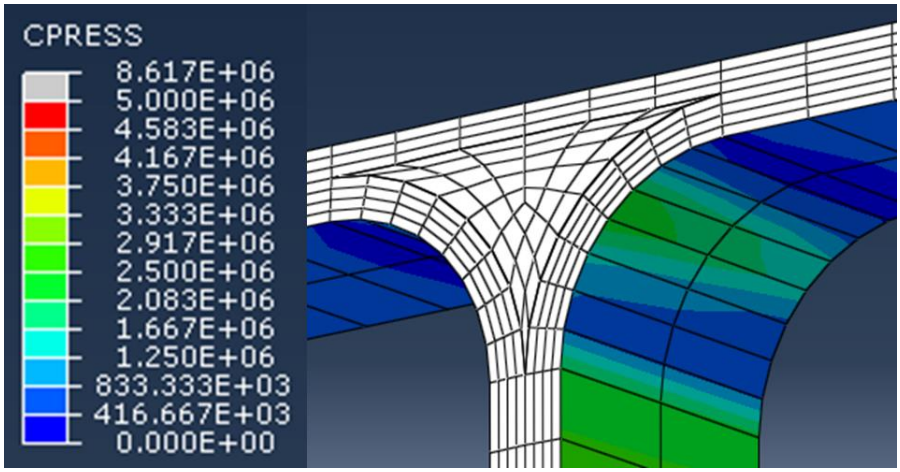

Figure 60. Contact pressure inside the T-Joint in aluminum tooling

The CCT process show a much smoother joint under higher contact pressure than the aluminum sample. The force is also distributed over the entire radii whereas in the aluminum process samples it is much more localized. The localized region in red on the contour plot below is due to the change in the surface definition at that element location and not a sudden change in force. Ignoring this, the CCT process appears to apply pressure directly to the radii with more force than the aluminum tooling. The aluminum is relying on outside forces from the autoclave pressure pushing the tooling together, and because of this the net force of the square tubing is directly inward onto the middle rib. However, this makes the consolidation at the radius a result

of indirect pressure. The CCT process applies pressure evenly on all surfaces inside the cores and therefore more direct pressure on the joints.

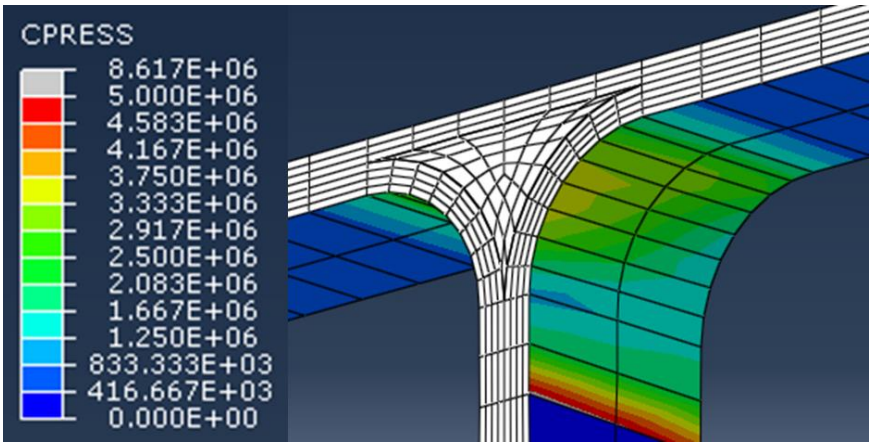

Figure 61. Contact pressure inside the T-Joint in CCT

Look at the top down significant differences can be seen around the noodle. Figure 62 shows a comparison of the two processing methods over 3 time increments; during the ramp up (20), the dwell (40), and the cool down (65). Equivalent time steps have been set to the same scale, the gradients around the noodle in the aluminum tooling are much more varied and lower than in the CCT process. The contact pressure was shown to be higher in the radius of the CCT in figure 61, but it is interesting to note that it is also the case here as there is direct pressure from the top skin tooling in the aluminum case as well. It can be seen that the contact pressure remains higher in the CCT process despite direct pressure from the aluminum tooling plate.

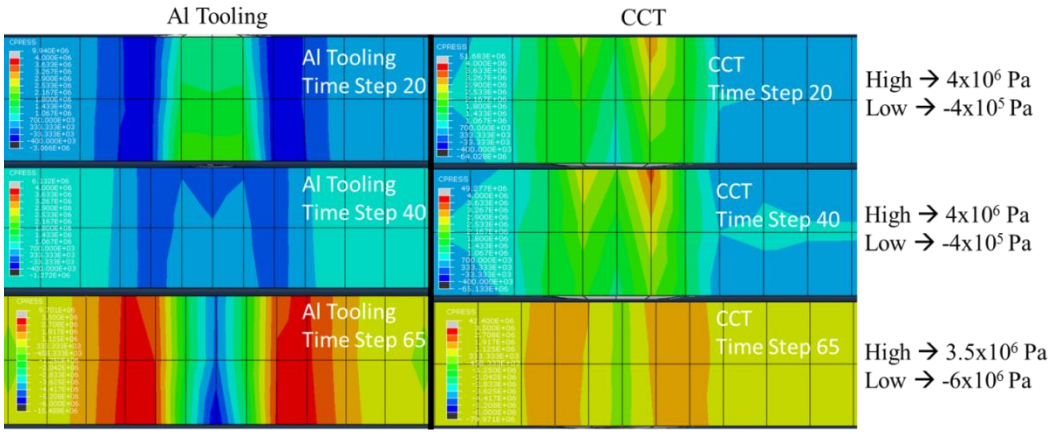

Figure 62. Contact pressure on the top skin around the noodle

Plotting the contact pressure at the radius we can see the behavior of the two methods of the course of the cure cycle with temperature and pressure. Figure 64 shows a significantly higher contact pressure throughout the cure in the CCT part. Now while this makes sense conceptually with the tool arrangement and materials, this value is significantly higher than both the autoclave pressure and pressure in the aluminum tooling sample, indicating that the model maybe be over-predicting the stress from the thermoplastic cores. This could be a symptom of the viscoelasticity of the cores being modeled as more elastic than the actual behavior.

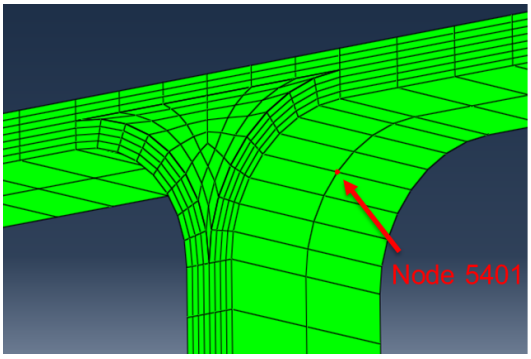

Figure 63. Image of node location for study

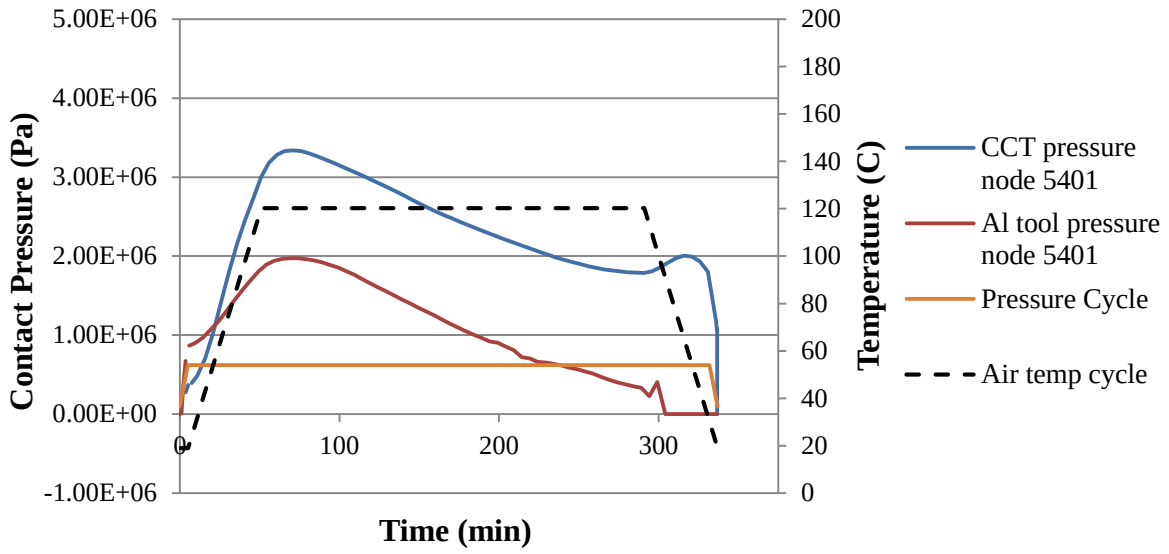

Figure 64. Contact pressure observed over cure cycle at node 5401 in both processing methods

Overall the stress models appear to behave similar to their respective processing methods, differences between the two methods can be measured in experimental samples validating that the models have contrasting approaches to curing composite parts. Based on the information presented here the CCT process has shown the capability of curing complex structures with integrated features due to the direct pressure applied to all surfaces of the composite by thermoplastic cores.

4.5 Summary of Stress Model

Variations in stress were found between the two processing methods. The aluminum tooling processing method has shown higher variation in stress than the CCT process due to the pressure direction, high stiffness, and CTE of the tooling material. In contrast the CCT process appears

more flexible and compliant with the composite, applying pressure on all surfaces as found in the radius of the composite. In addition process-induced stress and strain were evaluated based on their impact on the final part. The stress variation from the aluminum tooling showed up in the final rib thickness of samples, causing thinning towards the ends of the rib where higher stresses were observed. The CCT process appears capable of direct contact pressure over complex geometries, demonstrating the benefits of using thermoplastic cores as internal tools.

Chapter 5: Summary of Key Findings

5.1 Joint Characterization

The CCT process was studied for part quality and mechanical performance compared to traditional tooling methods. A design matrices approach was taken to maximize the data collected best capture the impact of each variable. Based on experimental data it was determined that filler noodle size has the greatest influence on the outcome of the part. In addition the shape must be well designed or the chance of porosity at the edges of the noodle will increase greatly. Pressure was observed to have a greater effect as the filler noodle size decreased, but pressure was not observed to make up for a noodle size insufficient for the space between cellular cores. The radius size was found to not influence the quality as long as the filler noodle was properly sized and shaped for the joint. Despite initial challenges when developing the CCT process, high quality, successful joints were produced indicating that this new technology has the capability to produce the features necessary for complex structures.

5.2 Mechanical Testing

Using the design matrix approach a series of mechanical tests were performed to study the effect of rib plies, radius, and splices on mechanical performance. The T-Joint geometry was chosen because of its role in complex structures and because it is a good indicator of consolidation. The T-Joint test studies matrix dominates properties such as porosity which are of interest for this project. It was found that the greatest contributing factor for strength was the number of rib plies.

Beyond this factor which was strongly expected, the next greatest contributing factor for strength was the radius size of the joint. The larger amount of materials coupled with the smooth curve at the joint made stress transfer easier with more material for carrying the load. Splices appeared to have no effect which is reassuring as complex lay-up patterns might be necessary with complex tooling and the ability to use separate plies without a drop off in strength is beneficial. Porosity was found to have a significant effect on strength given the out of plane loading and the demands on the matrix material. The high interlaminar normal stresses observed were validated by DIC and offered more proof that the interface between plies and especially between the noodle and rib plies is highly sensitive to flaws. The T-Joints manufactured with CCT were found to have equivalent if not superior strength to T-Joints processed with aluminum.

5.3 Thermal Model Profile

A thermal model was developed for the curing of parts made with CCT. This approach was taken because of the high potential for temperature variation within complex structures due to tooling, shape, and size. The model was designed in the FEA software Abaqus with COMPRO CCA designed to study process modeling of composites. Good correlation was observed between the model and experimental data collected. The model appears capable of mapping complex shapes and retains decent accuracy throughout the structure. A sensitivity analysis was performed to identify the HTC values needed to accurately map the profile. The cellular cores appear to not drastically inhibit the ability to predict the temperature profile and the model shows good ability to predict the temperature at several different locations. The model also shows the capability of expanding to other structures if HTC values around the part can be estimated.

5.4 Stress Analysis

Based on the results from the thermal model, a stress model was developed for the CCT process to examine process-induced stress. Samples tooled with aluminum appear to show greater stress states and greater variation ins stress states due to the expansion of the aluminum during cure coupled with the material stiffness. This expansion appears to benefit the consolidation of material at the joint but has been shown to increase residual stress on the part or cause processing defects such as low resin content or part thinning. Results of the model agree with thickness measurements taken supporting the variation in stress observed. Taking into consideration the results of the mechanical testing performed indicates that high quality parts can be produced with the CCT method with a potentially lower residual stress state and more consistent consolidation based on model comparisons.

5.5 Impact

This works hopes to benefit the manufacturing and development of composite structures. With the design of thermoplastic cores as novel tooling components, new complex parts can be co-cured as monolithic structures. The cores provide uniform compaction on all surfaces by applying pressure inside the cavities. Expansion of the cores creates a different consolidation technique capable of allowing all surfaces to see heat and pressure. The use of these cellular cores has been studied to understand how to optimize manufacturing with this approach. The goal of this work is to validate this new technology and demonstrate is feasibility in manufacturing aerospace structures. Using this innovative tooling design could significantly

reduce the weight of structure while taking advantage of the co-cured assembly to tailor parts to specific applications.

Process modeling was incorporated to demonstrate the benefit of process optimization on complex structures. Previously process modeling has been used with simple geometries to predict process factors such as degree of cure, resin viscosity, resin content, residual stress, and deformation. This approach has been applied to a double box beam to demonstrate that process modeling can be used effectively on complex structures and that it can predict these same processing factors. In addition the use of process modeling on CCT parts has never before been performed. Ultimately the benefit of this work is to develop a methodology for manufacturing complex composite structures. Co-curing composite structures offers many advantages over assembly methods while parts are in service, but manufacturing of these structures also becomes more complex. By incorporating process modeling into a new manufacturing method with few limitations such as CCT, new structures of almost any size or shape can be designed and optimized for any application.

5.6 Future Work

5.6.1 Resin Flow Model

Future work should focus on the development of the resin flow model. for the current work it has been assumed that the prepreg and manufacturing process are a net resin system, implying that the resin content does not change during the cure. In reality this may have an effect on the part

and may also vary with each material and geometry. Understanding the role of resin flow in the CCT process would be a valuable tool to incorporating this process. Mapping of resin content throughout the part would be valuable in evaluating any differences between CCT and other manufacturing methods. The flow data would be verified using acid digestion and thermogravimetric analysis (TGA) of localized samples[37, 38]. These techniques will be used to remove the matrix and measure the relative amount of fibers in the sample. Variations in resin content may appear throughout the sample and indicate any flow patterns that may exist.

Works Cited

[1] Agarwal, Bhagwan D. Broutman, Lawrence J. Chandrashekhara, K. *Analysis and Performance of Fiber Composites*. Third Edition. John Wiley and Sons, Inc. 2006.

[2] Wippl, Johann. Schmidt, Hans-Werner. Giesa, Reiner. *High Temperature Thermosets with a Low Coefficient of Thermal Expansion.* Macromolecular Chemistry I and Laboratory for Micro-scale Polymer Processing, University Bayreuth. 2005.

[3] Callister, William D. *Materials Science and Engineering an Introduction*. Sixth Edition. John Wiley and Sons, Inc. 2003.

[4] Bogetti, Travis A. Gillespie, John W. *Cure Simulation of Thick Thermosetting Composites*. Technical Report, Ballistic Research Laboratory. University of Delaware. 1990.

[5] Liu, Ling. Zhang, Bo-Ming. Wang, Dian-Fu. Wu, Zhan-Jun. *Effects of Cure Cycle on Void Content and Mechanical Properties of Composite Laminates.* Composite Structures, 73. 2006

[6] Anderson, J.P. Altan, M.C. *Properties of Composite Cylinders Fabricated by Bladder Molding Assisted Composite Manufacturing.* Journal of Engineering Materials and Technology. 2012

[7] Bossi, R. Carlsen, F. J. Boerio, and G. Dillingham. *Composite Surface Preparation QA for Bonding in SAMPE 2005*. Long Beach, 2005.

[8] Hart-Smith, L.J. *Bonded-Bolted Composite Joints.* American Institute of Aeronautics and Astronautics Inc. 1984.

[9] Matthews, F. L. Wong, C. M. Chryssafitis, S. *Stress Distribution around a Single Bolt in a Fibre-Reinforced Plastic. Composites*. 1982.

[10] Ireman, Tomas. *Three-Dimensional Stress Analysis of Bolted Single-Lap Composite Joints. Composite Structures*. 1998.

[11] Marshall, I. H. Arnold, W. S. Wood, J. *Observations on Bolted Connections in Composite Structures. Composite Structures*. 1989.

[12] Armstrong, Keith B. Bevan, L. Graham. Cole II, William F. *Care and Repair of Advanced Composites. Second Edition*. SAE International. 2005.

[13] Patent #8,337,740 "Reinforced Internal Composite Structures"

[14] Fernlund, G. Rahman, N. Courdji, R. Bresslauer, M. Poursartip, A. Willden, K. Nelson, K. *Experimental and Numerical Study of the Effect of Cure Cycle, Tool Surface, Geometry, and Lay-up on the Dimensional Fidelity of the Autoclave-Processed Composite Parts.* Composites, Part A: Applied Science and Manufacturing. 2002.

[15] Albert, C. Fernlund, G. *Spring-In and Warpage of Angled Composite Laminates*. Composites Science and Technology. 2002.

[16] Johnston, A. Hubert, P. Nelson, K. Poursartip, A. A Sensitivity Analysis of Factors Affecting the Warpage of Composite Structure. Institute for Aerospace Research, NRC. Boeing Defense and Space Group, Seattle, WA.

[17] Loos, Alfred C. Springer, George S. *Curing of Epoxy Matrix Composites*. Journal of Composite Materials, Vol. 17. 1983.

[18] Johnston, Andrew A. *An Integrated Model of the Development of Process-Induced Deformation in Autoclave Processing of Composite Structures*. Department of Metals and Materials Engineering. The University of New Brunswick. Ph. D. Dissertation. 1992.

[19] Bogetti, Travis A. Gillespie. *Process-Induced Stress and Deformation in Thick-Section Thermoset Composite Laminates*. Technical Report, Ballistic Research Laboratory. University of Delaware. 1990.

[20] Zienkiewicz, O. C. Taylor, R. L. Zhu, J. Z. *The Finite Element Method: Its basis and Fundamentals. Seventh Edition*. Elsevier Ltd. 2013.
[21]Advani, Suresh G. Sozer, E. Murat. *Process Modeling In Composites Manufacturing.* Second Edition. Taylor and Francis Group, LLC. 2011.
[22] COMPRO CCA for Abaqus Modeling Guidelines. Provided by Convergent Manufacturing Technologies. 2012.
[23] Fernlund, Goran. Floyd, Anthony. *Process Analysis and Tool Compensation for Curved Composite Laminates.* Presented at the Sixth Canadian International Composites Conference, Winnipeg, Canada. 2007.
[24] Zhao, Libin. Qin, Tianliang. Shenoi, R. Ajit. Zhang, Jianyu. Liang, Xianzhu. Huang, Hai. *Strength Prediction of Composite Pi Joints Under Tensile Loading*. Journal of Composite Materials. 2010.
[25] Diler, Ege Anile. Ozes, Cicek, Neser, Gokdeniz. *Effect of T-Joint Geometry on the Performance of a GRP/PVC Sandwich System Subjected to Tension*. Journal of Reinforced Plastics and Composites. 2009.
[26] Koh, T. M. Feih, S. Mouritz, A. P. *Experimental Determination of the Structural Properties and Strengthening Mechanisms of Z-Pinned Composite T-Joints*. Composite Structures. 2011.
[27] Vic-2D Guide. Provided by Correlated Solutions. 2009.
[28] Vic-2D Manual. Provided by Correlated Solutions. 2009.
[29] Montgomery, Douglas C. *Design and Analysis of Experiments*. Seventh Edition. John Wiley and Sons, Inc. 2009.
[30]https://www.google.com/search?q=design+of+experiments+2k+factorial+analysis&espv=2&biw=1455&bih=705&source=lnms&tbm=isch&sa=X&ved=0CAcQ_AUoAmoVChMIyMzt-IaJxwIVB5aICh3rZgnQ#imgrc=V1g3C6H16i0qiM%3A
[31] http://www.parkelectro.com/parkelectro/images/e-765.pdf
[32] http://www.cemselectorguide.com/pdf/CYCOM_5320-1_031912.pdf
[33] Slesinger, N. Shimizu, T. Arafath, A. R. A. Poursartip, A. *Heat Transfer Coefficient Distribution Inside an Autoclave*. The University of British Columbia, Department of Materials Engineering. ICCM Central Proceedings.
[34] Hubert, Pascal. *Aspects of Flow Compaction of Laminated Composite Shapes During Cure*. University of British Columbia, Ph. D Thesis. 1996.
[35]COMPRO Model Documentation. Release 1.2. Provided by Convergent Manufacturing Technologies. 2012.
[36] Dillman, S. H. Seferis, J. C. *Kinetic Viscoelasticity for the Dynamic Mechanical Properties of the Polymer*. Journal of Macromolecular Science-Chemistry, Vol. 26. 1989.
[37] Moon, Cho-Rok. Bang, Bo-Rae. Choi, Won-Jong. Kang, Gil-Ho. Park, Sang-Yoon. *A Technique for Determinging Fiber Content in FRP by Thermogravimetric Analysis*. Polymer Testing. 2005.
[38] Pickering, K. L. Blader, M. G. *Acid Digestion Study of Tensile Failure in Uniaxial Carbon Fibre Composites*. IPENZ Transactions, Vol. 24. 1997.
[39] Bogetti, Travis. Gillespie, John W. *Two Dimensional Cure Simulation of Thick Thermosetting Composites*. Journal of Composite Materials, Vol. 25. 1991.
[40] Polis, Daniel L. Sovinski, Marjorie F. *Determination of Fiber Volume in Carbon/Cynate Ester Composites Using Thermogravimetric Analysis*. NASA Center for Aerospace Information. 2007.

[41] Sicot, O. Gong, X. L. Cherouat, A. Lu, J. *Determination of Residual Stress in Composite Laminates Using the Incremental Hole-Drilling Method*. Journal of Composite Materials. 2003.
[42] Pagliaro, P. Zuccarello, B. *Residual Stress Analysis of Orthotropic Materials by the Through-Thickness-Hole Drilling Method*. Experimental Mechanics. 2007.
[43] Nelson, Ron H. *Prediction of Dimensional Changes in Composite Laminates During Cure*. 34th International Society for the Advancement of Material Process Engineering Symposium and Exhibition, Vol. 34. 1989.
[44] Abaqus/CAE User's Manual. Provided by Simulia. 2004.
[45] http://www.globalspec.com/learnmore/materials_chemicals/adhesives/epoxy_adhesives
[46] Prof. K. B. Das. Aircraft Composite Materials and Manufacturing Course. Boeing Company Learning, Training, and Development, Engineering and Operations Group. UW Materials Science and Engineering Department and UW Mechanical Engineering Department. 2012.

Appendix A

Demonstration of 1-dimensional heat conduction through composite thickness and evidence that heat generation from epoxy exotherm is minimal

Heat conduction equation modified to include heat generation from crosslinking ($\dot{Q}$)

$$\frac{\partial}{\partial t}(\rho C_p T) = \frac{\partial}{\partial x}\left(k_{xx}\frac{\partial T}{\partial x}\right) + \frac{\partial}{\partial y}\left(k_{yy}\frac{\partial T}{\partial y}\right) + \frac{\partial}{\partial z}\left(k_{zz}\frac{\partial T}{\partial z}\right) + \dot{Q}$$

Heat conduction modified for 1-dimension

$$\frac{\partial}{\partial t}(\rho C_p T) = \left(k_{zz}\frac{\partial T}{\partial z}\right) + \dot{Q}$$

Constants	Values	Units
Density, ρ	1.52E+03	kg/m^3
Specific Heat, C_p	9.42E-01	kJ/(kgK)
Thermal Cond., k	4.46E-04	kW/(mK)
Heat of Reaction, H_R	1.99E+02	kJ/kg

Expression for heat generated ($\dot{Q}$)

$$\dot{Q} = \frac{d\alpha}{dt}\rho H_R$$

Using approximate values taken from the modeled temperature/cure profiles the exothermic response of the material was determined ($\dot{Q}$) from the above expression

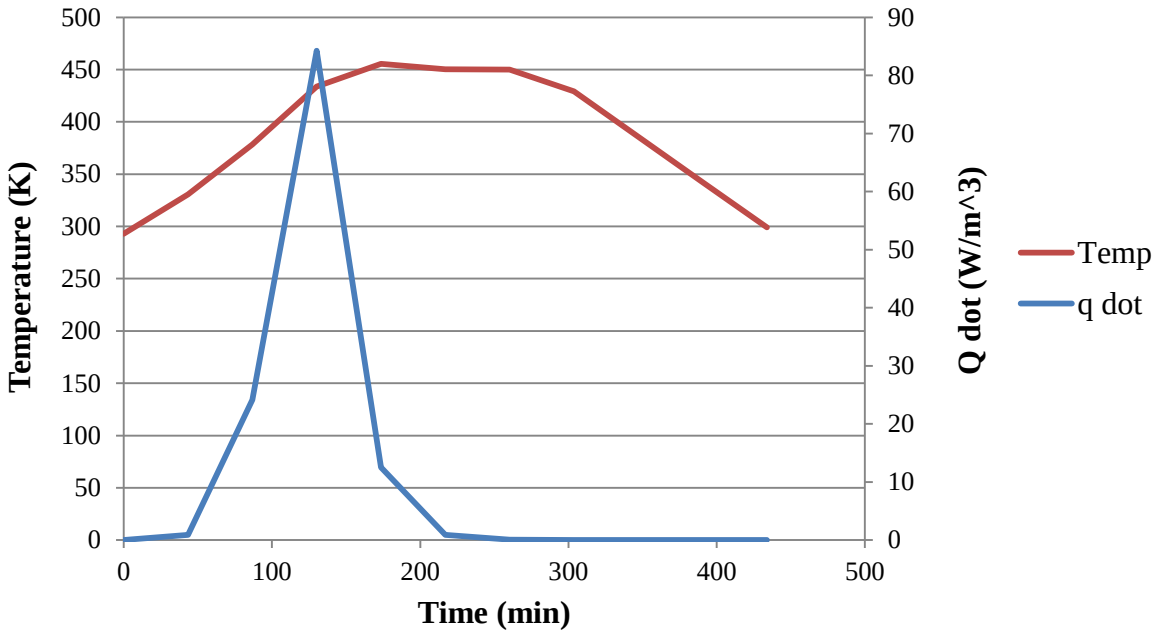

Using this profile, the instantaneous change in temperature can be found using the following expression for specific heat. For this study a 30 mm cube of material has been assumed with the corresponding mass.

$$\Delta T = \frac{Q}{mC_p}$$

Time (min)	Time (s)	Temperature	Cure	Cure Rate	Q dot	Q	ΔT (K)
0.00	0.00	293.00	0.0000	0.00	0.0204	0.0000	0.00
43.40	2604.00	330.55	0.0018	0.00	0.8704	0.0313	0.03
86.80	5208.00	378.49	0.0683	0.00	24.1337	0.9103	0.97
130.20	7812.00	433.85	0.4424	0.00	84.2644	4.7209	5.01
173.60	10416.00	455.57	0.9607	0.00	12.5338	8.1238	8.62
217.00	13020.00	450.40	0.9966	0.00	0.9241	8.5969	9.13
260.40	15624.00	450.04	0.9997	0.00	0.0917	8.6326	9.16
303.80	18228.00	429.19	1.0000	0.00	0.0062	8.6360	9.17
347.20	20832.00	385.82	1.0000	0.00	0.0006	8.6363	9.17
390.60	23436.00	342.42	1.0000	0.00	0.0001	8.6363	9.17
434.00	26040.00	299.02	1.0000	0.00	0.0000	8.6363	9.17

From this calculation only a small increase in temperature is observed over the course of the cure from the exotherm of the resin. The graph below shows the overall temperature increase due to the exothermic reaction over of the course of the cure cycle. These values agree with literature data presented by Bogetti and Gillespie in *Two Dimensional Cure Simulation of Thick Thermosetting Composites* which demonstrated that a value of approximately 8.0 K was reasonable for the exotherm of the resin[39].

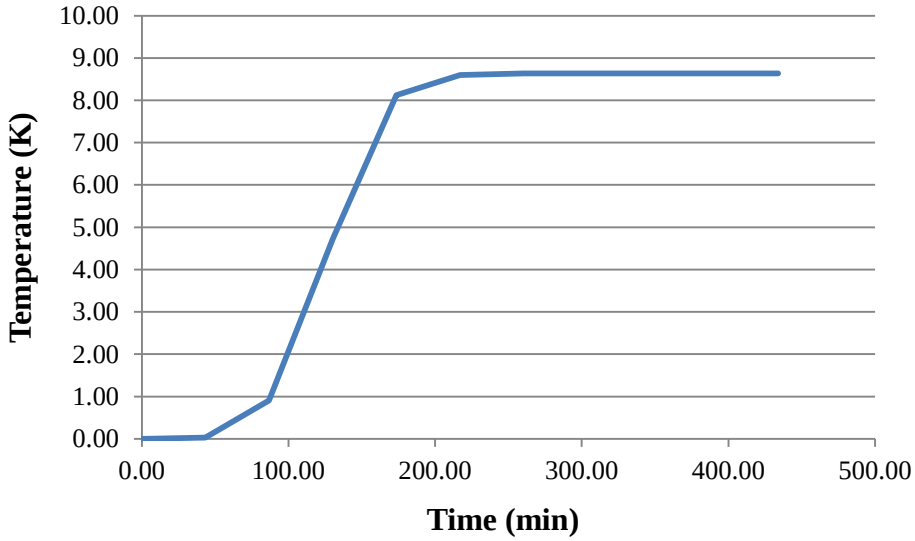

Appendix B

Example Calculation of Heat Transfer Coefficient (HTC) using lumped mass Calorimeter as demonstration of values used in thermal model. While the Cycom 5320-1 material was ideal for the novel processing method and used for the majority of this work, the AS4-3501-6 tape was used for this calculation as an established, open literature material that could be referenced with the material properties included[34]. This is the same material used in the plate model as a comparison between the FEA approach and the mathematical approach.

Heat transfer coefficient of a lumped mass calorimeter

$$h = \frac{\rho C_p V \dot{T}}{A \Delta T_s}$$

Constants	Values	Units
Density, ρ	7850	kg/m^3
Specific Heat, C_p	4.65E+02	J/kgK
Diameter	0.0127	m
Length	0.08725	m
Volume, V	1.1047E-05	m^3
Surface Area, A	0.00373258	m^2

$\dot{T}$ represents the instantaneous temperature rate of the lumped mass calorimeter and ΔT_s is the difference between the air temperature and the calorimeter. Data collected from thermocouples placed on top of the tool closure yielded the following data for the air temperature and the temperature of the calorimeter.

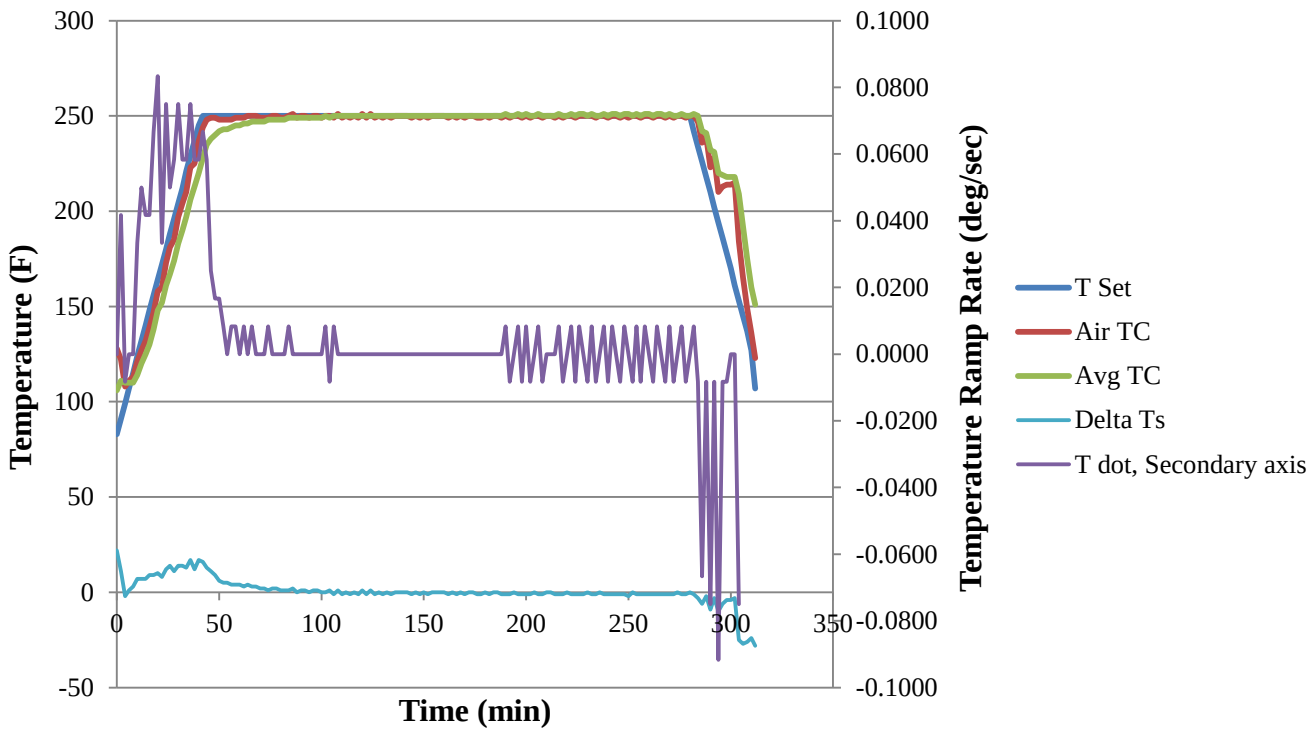

Looking at the ramp up to dwell, the heat transfer coefficient can be calculated from the equation given above. The following graph shows that the HTC value during ramp is approximately 50 W/m^2K which agree with our sensitivity analysis which found that 60 W/m^2K approximated the autoclave conditions. Typical HTC values inside an autoclave can range from 5 to 300 depending on a variety of factors including, temperature, temperature rate, autoclave size/shape, tooling, etc[33]. An approximate difference of 10 W/m^2K is negligible on the scale of autoclave heating.

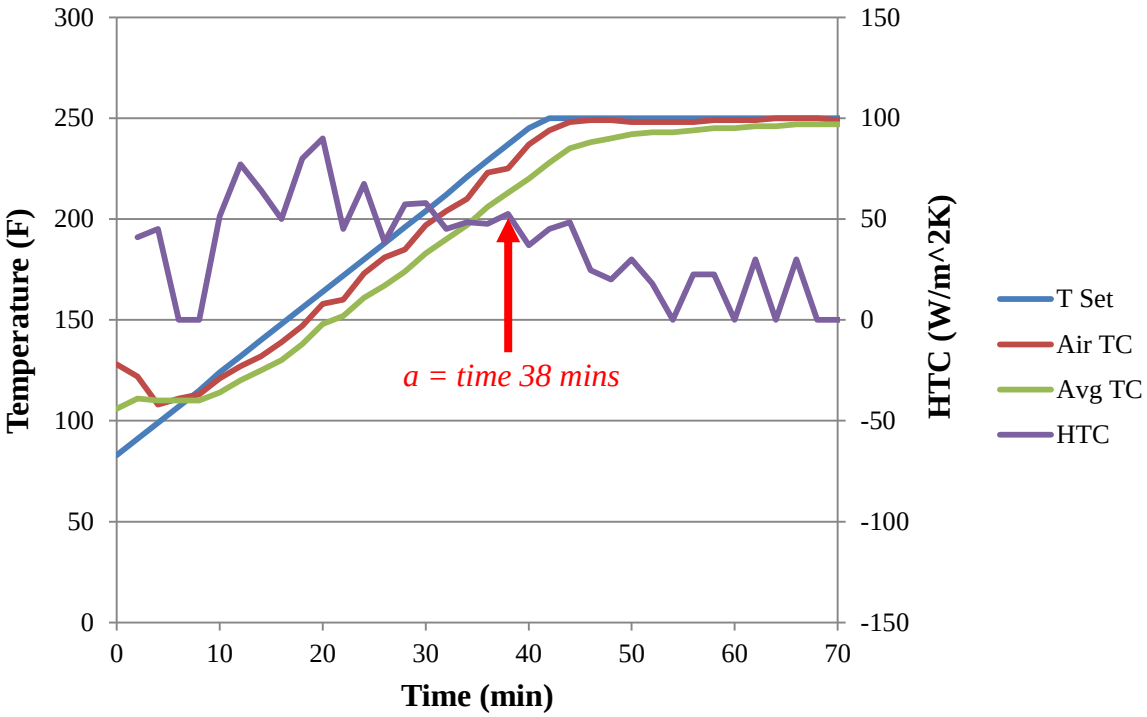

As a demonstration of the calculation for HTC, looking specifically at a moment in time of the ramp up, we can determine a precise value for HTC. This can be a good check of the approach used in this study and a validation of values used in the model. An example calculation has been included at the time t = 38 minutes which can be seen in the above graph at point a.

$$\dot{T} = .0583\ °F/s \text{ at } t = 38\ min$$

$$\Delta T_s = 12\ °F \text{ at } t = 38\ min$$

$$h = \frac{\rho C_p V \dot{T}}{A \Delta T_s} = \frac{(7850)(4.65 \times 10^2)(1.1047 \times 10^{-5})(.0583)}{(0.00373258)(12)} = 52.52\ W/m^2K$$

$$\boldsymbol{h = 52.52\ W/m^2K}$$

This calculation agrees with the graph above at time t = 38 mins and our sensitivity analysis performed with COMPRO CCA.

Appendix C

One Dimensional Heat Transfer Problem

```
C LNB - 2015 - Curtis Hickmott's problem - 1d thermal transport in a
C curing composite. The computation is based on a one-dimensional version
C of the equations presented in the paper entitled "Cure Simulation Of
C Thick Thermosetting Composites" by Bogetti and Gillespie - technical
C report BRL-TR-3121 (BRL AD-A224 885) written in 1990. All of the material
C parameters and properties, geomeotry and boundary conditions used in
C this program are taken from this paper. Also check out the paper by Loos
C and Springer (12) in the report cited above because they have apparently
C done the 1D graphite/epoxy. (In general, this is not a new problem
C mathematically, computationally nor in application.)

C In this fortran program a one-dimensional heat equation is solved. But
C the material simulated in the 2D version provided in the report above is
C anisotropic with respect to thermal conduction. Thus it is necessary
C to carefully choose the direction in which the the thermal gradient is
C applied in order that one dimensional computation is physically valid,
C for example along a principle axis. Otherwise, in general, there will be
C the generation of three components of heat flux, parallel and two
C perpendicular to the orientation of the applied thermal gradient, that
C will require a full 2D (or 3D) computation to correctly model the
C curing composite. An isotropically conductive system always will have the
C heat flux aligned with the thermal gradient, therefore, this program
C is completely appropriate for any direction of applied thermal gradient
C in an isotropic system.

C The numerical method used is an explicit finite difference scheme for a 1D
C heat equation with a source term. The source term is proportional to the
C composite curing rate. The accuracy of the numerical scheme is O(delta t)
C and O(delta x^2), i.e. first order in time and second order in space.
C The source term, being proportional to the curing rate, therefore is
C written as an ordinary differential equation in time, that has non-constant
C coefficients (i.e. can be time dependent through the temperature) but
C then which also depends on location (x). For now the cure rate is also
C computed by a first order finite difference in time, but since it is a
C function of position, the ODE's are defined on the discretized domain.

C Initial conditions are a uniform temperature field in the interior and
C whatever the temperatures are at the boundaries according to the constants
C included in the boundary conditions. The cure fraction is initially 0
C everywhere including at the boundaries. The composite also cures at the
C boundaries, i.e. the fraction of curing at x = xl and x = xr is also
```

```
C determined as part of the solution to the problem.

C Programming notes:
C (1.) The time integration of the temperature and the cure rate could be made
C more accurate by switching to a number of different schemes, for example
C using a Runge Kutta, or a Gear-based integrator, such as ddriv3.
C (2.) In this version of the code the cure level and the temperatures are
C stored as matrices for all locations and times. The longer the time
C integration and the finer the spatial dicretization the more storage that
C required.
C (3.) In the program the Courant-Frederichs-Levy (CFL)L condition for the
C numerical stability is automatically enforced as seen in the definition
C of dt.
C (4.) The output of the program is automatically set to be at 10 equal
C increments in time over tmax. This can be changed by changing the
C appropriate parameter in the parameter line.
C (5.) If resolution required leads to storage issues (which could happen for
C example if much more refinement than 100-1000 spatial nodes and integration
C for much longer times is required then it is simple to write a version that
C only stores the current values of alpha and temperature.
C (6.) The boundary conditions allow for a time dependent forcing term (for
C example a time-dependent ambient temperature or gradient, etc. through the
C function tinf. That can be changed to suit needs.
C (7.) Note that if another time dependent function is defined, or any other
C changes are made then all newly defined variables need to be declared.
C (8.) All variables are set explicilty within the program. It would be more
C efficient to read in from a data file - then you could run batch jobs.
C (9.) The program can be converted to quad precision by all of the real*8
C commands to real*16.
C (10.) To run:

C   compilation command:            $ gfortran curtis-exp.f
C   creates executable that runs with: $ ./a.out
C        or
C   compilation command:            $ gfortran -o xxxxx curtis-exp.f
C   creates executable that runs with: $ ./xxxxx
C   ($ denotes the terminal prompt and ./ denotes the current directory)
C
C This version here don't store data just print it out at each time step.

      program cure
      implicit none
      integer n0, nx, nxp1, nt, i, j, k, l, mm, ntmod, ntdim
      parameter(n0 = 0, nx = 199, nxp1 = nx + 1)

      real*8 alpha(n0:nxp1,1),temp(n0:nxp1,1)
```

```
      real*8 qdotv(n0:nxp1,1)
      real*8 x(n0:nxp1)
      real*8 tinf,t0,t1,t2,t3,thold
      real*8 a0u,b0u,a0h,b0h,a0d,b0d,alu,blu,alh,blh,ald,bld
      real*8 tinbulk,fint,tdiff,qdot0,qdotl
      real*8 tempup,alphaup

      real*8 dx,dt,tmax,time0,alen,tim
      real*8 cond,diff,cp,dens,heat,hr,gas
      real*8 a1,a2,a3,e1,e2,e3
      real*8 ao,bo,co,al,bl,cl,ainfo,ainfl,binfo,binfl,omegao,omegal
      real*8 qdot,temp0,templ

C material property definitions: graphite-epoxy system

      cond = 4.457d-04
      cp   = 9.42d-01
      dens = 1.52d3
      hr   = 198.9d0

C derived variables

      diff = cond/(dens*cp)
      heat = hr/cp

C domain dimension (cm in the direction of heat transfer) should be 2.54

      alen = 30.0d-3
      dx = alen/float(nxp1)

C thermal

      tinbulk = 293.0d0

C  times denoting thermal schedule at the end locations

C initial

      t0 = 0.0d0

C ramp up time duration

      t1 = 9420.0d0

C hold time duration
```

```
      thold = 7200.0d0

C time from initiation of curing to end of hold period
C i.e. time at beginning of ramp down period

      t2 = t1 + thold

C time from initiation of curing to end of ramp down

      t3 = t2 + 9420.0d0

C total time of cure cycle
C time from initiation of curing to end of ramp down

      tmax = t3

C time step, dt, calculated to guarantee numerical
C stability (obeys CFL condition) given a maximum
C time based on thermal schedule and given a spatial step

      fint = tmax*diff/(0.001*dx*dx)
      nt = int(fint)+1
      ntmod = (nt-1)/10
      dt = tmax/float(nt-1)

C time step calculated to guarantee numerical stability
C given a spatial step and given the number of time steps.

C     dt = 0.001d0*dx*dx/diff
C      tmax = float(nt-1)*dt
C      print *,dx,dt,tmax
C      dx = alen/float(nxp1)

C thermal coefficients for the temperature at the ends that
C is calculated by the real*8 function tinf(-,-,-,-):
C i.e.  tinf = a + b*t where the a's and b's are given below:

C     coefficients for the left hand side (x = 0):

C ramp up period

      a0u = 293.0d0
      b0u = 0.016666666666666d0

C hold period
```

```
      a0h = 450.0d0
      b0h = 0.0d0

C ramp down period

      a0d = 450.0d0
      b0d = -0.016666666666666d0

C     coefficients for the right hand side (x = l):

C ramp up period

      alu = 293.0d0
      blu = 0.016666666666666d0

C hold period

      alh = 450.0d0
      blh = 0.0d0

C ramp down period

      ald = 450.0d0
      bld = -0.016666666666666d0

C mixed boundary condition definitions. Note that below
C are set for a prescribed temperature at the ends. But
C for different choices of the coefficients there is the
C possibility of mixed conditions.

      ao = 0.0d0
      bo = 1.0d0
      co = -1.0d0
      al = 0.0d0
      bl = 1.0d0
      cl = -1.0d0

C These are the temporal frequencies for sinusoidal
C forcing at the far boundaries through the sin(wt)
C function in the commented out statement in tinf.

      omegao = 0.0d0
      omegal = 0.0d0

C curing activation parameters
C   (e_i's in units of J/mol)
```

```
C   (a_i's in units of sec^-1)
C   (commented out a_i's in units of min^-1)

      a1  = 0.035d9
      a2  = -0.03356d9
      a3  = 0.0326d5
      e1  = 8.07d4
      e2  = 7.78d4
      e3  = 5.66d4

C universal gas constant values
C  8.3145       J K^-1 mol^-1
C  8.3145 (10^7) erg K^-1 mol^-1
C  1.9872       cal K^-1 mol^-1
C  1.9872 (10^7) cal K^-1 mol^-1

      gas = 8.3145d0

C initialization of variables
C initialization alpha (cure fraction) and temperature field in domain.

        tim = 0.0d0

      do i = 0,nxp1
        x = float(i)*dx
        alpha(i,1) = 0.0d0
        temp(i,1) = tinbulk
        qdot = (1.0d0-alpha(i,1))*(0.47d0-alpha(i,1))*(a1*exp(-e1/
     .   (gas*temp(i,1))) + alpha(i,1)*a2*exp(-e2/(gas*temp(i,1))))
        qdotv(i,1) = qdot
      end do

C initial boundary temperatures and cure rates

        temp0 = (4.0d0*ao*temp(1,1)-ao*temp(2,1)+co*dx*
     .           tinf(tim,a0u,b0u,omegao))
     .           /(3.0d0*ao-bo*dx)
        temp(0,1) = temp0
        qdot0 = (1.0d0-alpha(0,1))*(0.47d0-alpha(0,1))*(a1*exp(-e1/
     .   (gas*temp(0,1))) + alpha(0,1)*a2*exp(-e2/(gas*temp(0,1))))
        qdotv(0,1) = qdot0
        templ = (4.0d0*al*temp(nx,1)-al*temp(nx-1,1)-cl*dx*
     .           tinf(tim,alu,blu,omegal))
     .           /(3.0d0*al+bl*dx)
        temp(nxp1,1) = templ
        qdotl = (1.0d0-alpha(nxp1,1))*(0.47d0-alpha(nxp1,1))*
```

```
     . (a1*exp(-e1/(gas*temp(nxp1,1))) + alpha(nxp1,1)*a2*
     . exp(-e2/(gas*temp(nxp1,1))))
       qdotv(nxp1,1) = qdotl

C If want to print to output file start with this

      open(unit=20,file='curtis-fast.dat',status='unknown')

      write(20,*)' ramp up time = ',t1
      write(20,*)' time to end of hold = ',t2
      write(20,*)' time to end of ramp down = ',tmax
      write(20,*)' total time steps, nt = ',nt,' time step, dt = ',dt
      write(20,*)'(columns: position, temperature, cure, cure rate)'

      print *,' ramp up time = ',t1
      print *,' time to end of hold = ',t2
      print *,' time to end of ramp down = ',tmax
      print *,' total time steps, nt = ',nt,' time step, dt = ',dt
      print *,'(columns: position, temperature, cure, cure rate)'
      print *,'(columns: position, temperature, cure, cure rate)'

         print *,'time =', tim
         write(20,*)'time =', tim
         do l = 0,nxp1
         print *, dx*float(l), temp(l,1), alpha(l,1), qdotv(l,1)
         write(20,*) dx*float(l), temp(l,1), alpha(l,1), qdotv(l,1)
         end do

C Iterate over time:

      do j=1,nt-1

C Actually repeating here what is done above for j = 1. Above is needed
C to output the initial data.

         tim = float(j-1)*dt

         if(tim.lt.t1)then
           ainfo = a0u
           binfo = b0u
           ainfl = alu
           binfl = blu
           tdiff = tim
           else if(tim.ge.t1.and.tim.le.t2) then
           ainfo = a0h
           binfo = b0h
```

```
        ainfl = alh
        binfl = blh
        tdiff = tim - t1
        else if(tim.gt.t2) then
        ainfo = a0d
        binfo = b0d
        ainfl = ald
        binfl = bld
        tdiff = tim - t2
        end if

      do i=n0,nxp1
        x(i) = float(i)*dx
        if (alpha(i,1).le.0.3)then
         qdot = (1.0d0-alpha(i,1))*(0.47d0-alpha(i,1))*(a1*exp(-e1/
     .   (gas*temp(i,1))) + alpha(i,1)*a2*exp(-e2/(gas*temp(i,1))))
         qdotv(i,1) = qdot
         alphaup = alpha(i,1) + dt*qdot
         alpha(i,1) = alphaup
        else if (alpha(i,1).gt.0.3) then
         qdot = (1.0d0-alpha(i,1))*(a3*exp(-e3/(gas*temp(i,1))))
         qdotv(i,1) = qdot
         alphaup = alpha(i,1) + dt*qdot
         alpha(i,1) = alphaup
        end if
        if (i.ne.n0.and.i.ne.nxp1)then
        tempup = temp(i,1) + (diff*dt/(dx*dx))*(temp(i+1,1)
     .      - 2.0d0*temp(i,1) + temp(i-1,1)) + (dt*heat)*qdot
        temp(i,1) = tempup
        end if

C Temperatures at the ends are recalculated using updated adjacent
C values within the layer

        temp0 = (4.0d0*ao*temp(1,1)-ao*temp(2,1)+co*dx*
     .           tinf(tdiff,ainfo,binfo,omegao))
     .           /(3.0d0*ao-bo*dx)
        temp(0,1) = temp0

        templ = (4.0d0*al*temp(nx,1)-al*temp(nx-1,1)-cl*dx*
     .           tinf(tdiff,ainfl,binfl,omegal))
     .           /(3.0d0*al+bl*dx)
        temp(nxp1,1) = templ
       end do

         mm = mod(j,ntmod)
```

```
        if (mm.eq.0)then
        write(20,*)'time =', tim
        print *,'time =', tim
        do l = 0,nxp1
        print *, float(l)*dx, temp(l,1), alpha(l,1), qdotv(l,1)
        write(20,*) dx*float(l), temp(l,1), alpha(l,1), qdotv(l,1)
        end do
        end if

      end do

      tim = float(nt-1)*dt


      temp0 = (4.0d0*ao*temp(1,1)-ao*temp(2,1)+co*dx*
     .          tinf(tdiff,ainfo,binfo,omegao))
     .          /(3.0d0*ao-bo*dx)
      temp(0,1) = temp0
      templ = (4.0d0*al*temp(nx,1)-al*temp(nx-1,1)-cl*dx*
     .          tinf(tdiff,ainfl,binfl,omegal))
     .          /(3.0d0*al+bl*dx)
      temp(nxp1,1) = templ

C last time step

      print *,'time =', tim
      write(20,*)'time =', tim
      do l = 0,nxp1
C Check why temp(0,nt-1) is appropriate but not temp(0,nt)
      print *, dx*float(l), temp(l,1), alpha(l,1), qdotv(l,1)
      write(20,*) dx*float(l), temp(l,1), alpha(l,1), qdotv(l,1)
      end do
        close(unit = 20)

      end

    real*8 function tinf(t,a,b,om)
    implicit none
    real*8 t,a,b,om

     tinf = a + b*t

    return
    end
```

Appendix D

Model Assembly Components

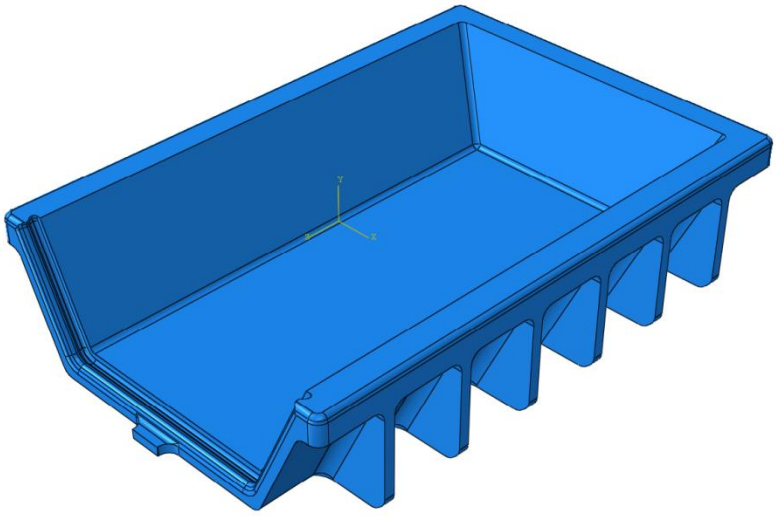

Model Base

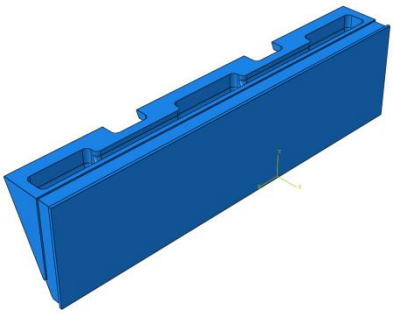

Side Wedge (aluminum)

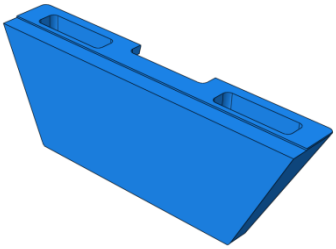

Rear Wedge (aluminum)

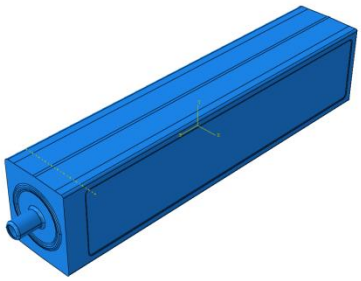

Cellular Core (Acetal)

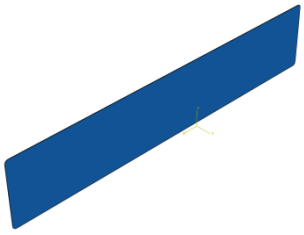

Pressure Plate (steel)

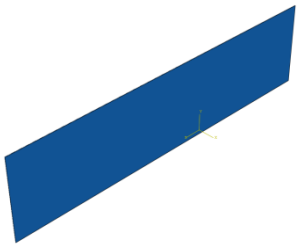

Side Spacer (steel)

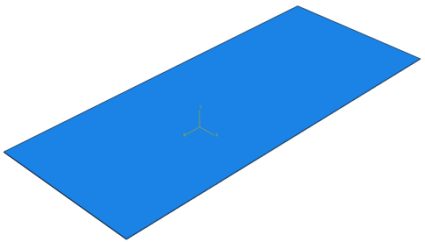

Top Spacer (steel)

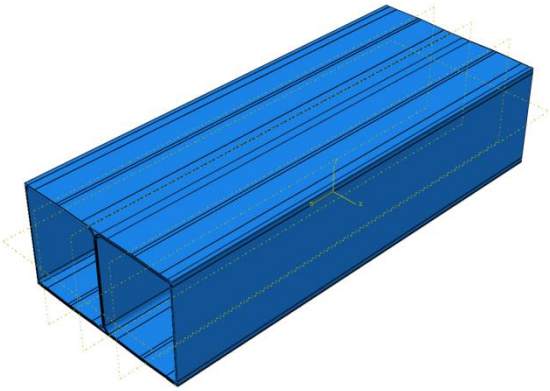

Composite Plies (Cycom 5320-1)

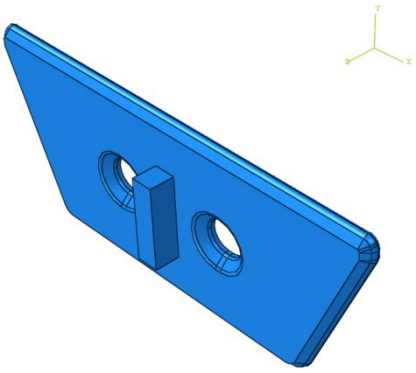

Front Insert (aluminum)

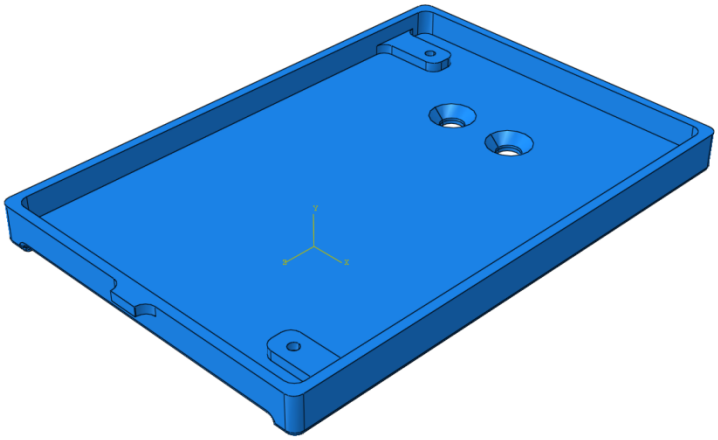

Closure (aluminum)

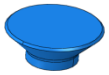

Plug (aluminum)

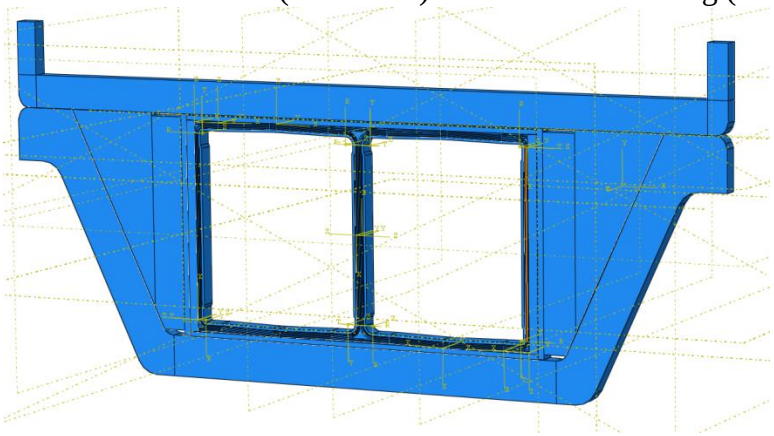

Cross Section of Assembly

Appendix E

Example File for Composite Material Data Sheet – AS4-3501-6 Composite

```
<!-- $Id: COMPOSITE-HEXCEL-3501-6-AS4-Tape-v1.xml 2486 2010-02-05 22:20:24Z anthony $ -->
<!-- ================================================================ -->
<!-- Convergent Common Component Architecture (CCA) for COMPRO/Raven  -->
<!--                                                                  -->
<!-- Convergent Manufacturing Technologies Inc.                       -->
<!-- 6190 Agronomy Road, Suite 403                                    -->
<!-- Vancouver, British Columbia, Canada                              -->
<!-- support@convergent.ca  or www.convergent.ca                      -->
<!--                                                                  -->
<!-- (c)2008 Convergent Manufacturing Technologies, Inc               -->
<!-- All rights reserved.                                             -->
<!-- ================================================================ -->
<!--                                                                  -->
<!--      Models          Developer/Source           Date         -->
<!--   ++++++++++++++    ++++++++++++++++++++       ++++++++++      -->
<!--       CTE         source not known - MASKED    2008-08-01      -->
<!--    Permeability     PH thesis,p262-3           2008-08-01      -->
<!--   FB Compaction     PH thesis,p277,FB.14       2008-08-01      -->
<!--   Ply thickness     HEXCEL datasheet           2010-01-22      -->
<!--                                                                  -->
<!-- Comments:                                                        -->
<!--                                                                  -->
<!--                                                                  -->
<!-- ================================================================ -->
<!-- RELEASE/PERMISSIONS                                              -->
<!--    Release:   Open                                               -->
<!--    Internal:  Open                                               -->
<!--    Customer:  N/A                                                -->
<!--                                                                  -->
<!-- ================================================================ -->
<material unique_name="COMPOSITE-HEXCEL-3501-6-AS4-Tape-v1"
general_name="COMPOSITE" display_name="HEXCEL AS4/3501-6 Tape" type="composite"
last_update="2008-08-01" last_update_by="AS" comments="Input values verified.">
  <revision value="1" date="2010-02-04" comment="Initial model in revisioning system">
    <constituent volume_fraction="0.558" type="fibre" revision="1">FIBRE-AS4-v1</constituent>
    <constituent volume_fraction="0.442" type="matrix" revision="1">MATRIX-HEXCEL-3501-6-
v1</constituent>
    <previously_known_as name="HEXCEL-3501-6-AS4-Tape-v1.xml" />
    <ply_thickness value="0.150E-3" units="m" />
    <property_mask mask="16515975"/>
    <micromechanics model="default" />
    <lamina_properties>
      <LumpedDensity model="none" />
      <LumpedCp model="none" />
      <LumpedK model="none" />
```

```
  <LumpedCTE model="default" number_of_parameters="8">
    <parameter name="NomCTE11" parameter_number="1" units="1/K" value="0.000" />
    <parameter name="CTE11TF" parameter_number="2" units="1/K2" value="2.000E-09" />
    <parameter name="CTE11AF" parameter_number="3" units="1/K" value="0.00" />
    <parameter name="NomCTE22" parameter_number="4" units="1/K" value="2.250E-05" />
    <parameter name="CTE22TF" parameter_number="5" units="1/K2" value="2.500E-08" />
    <parameter name="CTE22AF" parameter_number="6" units="1/K" value="-3.500E-06" />
    <parameter name="CTET0" parameter_number="7" units="C" value="20.00" />
    <parameter name="CTEAL0" parameter_number="8" units="none" value="0.000" />
  </LumpedCTE>
  <permeability model="4" number_of_parameters="4">
    <parameter name="Rf" parameter_number="1" units="m" value="4.0000E-06" />
    <parameter name="Va" parameter_number="2" units="none" value="8.100E-01" />
    <parameter name="kx" parameter_number="3" units="none" value="0.7" />
    <parameter name="kz" parameter_number="4" units="none" value="0.2" />
  </permeability>
  <fibre_bed_compaction model="2" number_of_parameters="6">
  <!-- The modulus values are obtained based on micromechanics for a unidirectional laminate -->
    <parameter name="E1" parameter_number="1" units="Pa" value="1.17E+11" />
    <parameter name="E2" parameter_number="2" units="Pa" value="7.92E+06" />
    <parameter name="E3T" parameter_number="3" units="Pa" value="7.92E+06" />
    <parameter name="G12" parameter_number="4" units="Pa" value="2.64E+06" />
    <parameter name="G13" parameter_number="5" units="Pa" value="2.64E+06" />
    <parameter name="G23" parameter_number="6" units="Pa" value="2.64E+06" />
    <table col1="EPS3" units1="none" col2="SIG3" units2="Pa">
      <datarow  col1="0.000E+00"  col2="0.000E+00" />
      <datarow col1="-6.000E-02" col2="-2.400E+04" />
      <datarow col1="-1.000E-01" col2="-6.700E+04" />
      <datarow col1="-1.300E-01" col2="-1.360E+05" />
      <datarow col1="-1.600E-01" col2="-2.670E+05" />
      <datarow col1="-1.800E-01" col2="-5.250E+05" />
      <datarow col1="-2.070E-01" col2="-9.790E+05" />
      <datarow col1="-2.270E-01" col2="-1.617E+06" />
      <datarow col1="-2.356E-01" col2="-2.082E+06" />
      <datarow col1="-2.380E-01" col2="-2.251E+06" />
    </table>
  </fibre_bed_compaction>
</lamina_properties>
<cure_cycle name="1.0 C/min, hold @ 180 C 2 hrs">
  <segment type="initial">
    <parameter type="initial" value="20.0" units="C"/>
  </segment>
  <segment type="ramp">
    <parameter type="target" value="180.0" units="C"/>
    <parameter type="rate" value="1.0" units="C/min"/>
  </segment>
  <segment type="hold">
    <parameter type="time" value="120.0" units="min"/>
  </segment>
  <segment type="ramp">
    <parameter type="target" value="20.0" units="C"/>
```

```
      <parameter type="rate" value="2.0" units="C/min"/>
    </segment>
  </cure_cycle>
  <cure_cycle name="0.5 C/min, hold @ 180 C 2 hrs">
    <segment type="initial">
      <parameter type="initial" value="20.0" units="C"/>
    </segment>
    <segment type="ramp">
      <parameter type="target" value="180.0" units="C"/>
      <parameter type="rate" value="0.5" units="C/min"/>
    </segment>
    <segment type="hold">
      <parameter type="time" value="120.0" units="min"/>
    </segment>
    <segment type="ramp">
      <parameter type="target" value="20.0" units="C"/>
      <parameter type="rate" value="2.0" units="C/min"/>
    </segment>
  </cure_cycle>
  <cure_cycle name="1.0 C/min, hold @ 120 C 2 hrs">
    <segment type="initial">
      <parameter type="initial" value="20.0" units="C"/>
    </segment>
    <segment type="ramp">
      <parameter type="target" value="120.0" units="C"/>
      <parameter type="rate" value="1.0" units="C/min"/>
    </segment>
    <segment type="hold">
      <parameter type="time" value="120.0" units="min"/>
    </segment>
    <segment type="ramp">
      <parameter type="target" value="20.0" units="C"/>
      <parameter type="rate" value="2.0" units="C/min"/>
    </segment>
  </cure_cycle>
  <cure_cycle name="0.5 C/min, hold @ 120 C 2 hrs">
    <segment type="initial">
      <parameter type="initial" value="20.0" units="C"/>
    </segment>
    <segment type="ramp">
      <parameter type="target" value="120.0" units="C"/>
      <parameter type="rate" value="0.5" units="C/min"/>
    </segment>
    <segment type="hold">
      <parameter type="time" value="120.0" units="min"/>
    </segment>
    <segment type="ramp">
      <parameter type="target" value="20.0" units="C"/>
      <parameter type="rate" value="2.0" units="C/min"/>
    </segment>
  </cure_cycle>
```

```
    <cure_cycle name="1.0 C/min, hold @ 120 C 1 hr, hold @180 C 2 hrs">
      <segment type="initial">
        <parameter type="initial" value="20.0" units="C"/>
      </segment>
      <segment type="ramp">
        <parameter type="target" value="120.0" units="C"/>
        <parameter type="rate" value="1.0" units="C/min"/>
      </segment>
      <segment type="hold">
        <parameter type="time" value="60.0" units="min"/>
      </segment>
      <segment type="ramp">
        <parameter type="target" value="180.0" units="C"/>
        <parameter type="rate" value="1.0" units="C/min"/>
      </segment>
      <segment type="hold">
        <parameter type="time" value="120.0" units="min"/>
      </segment>
      <segment type="ramp">
        <parameter type="target" value="20.0" units="C"/>
        <parameter type="rate" value="2.0" units="C/min"/>
      </segment>
    </cure_cycle>
  </revision>
</material>
```

Example File for Fiber Material Data Sheet – AS4-3501-6 Composite

```
<!-- $Id: FIBRE-AS4-v1.xml 2486 2010-02-05 22:20:24Z anthony $ -->
<!-- ================================================================= -->
<!-- Convergent Common Component Architecture (CCA) for COMPRO/Raven  -->
<!--                                                                   -->
<!-- Convergent Manufacturing Technologies Inc.                        -->
<!-- 6190 Agronomy Road, Suite 403                                     -->
<!-- Vancouver, British Columbia, Canada                               -->
<!-- support@convergent.ca  or www.convergent.ca                       -->
<!--                                                                   -->
<!-- (c)2008 Convergent Manufacturing Technologies, Inc                -->
<!-- All rights reserved.                                              -->
<!-- ================================================================= -->
<!--                                                                   -->
<!--      Models          Developer          Date                      -->
<!--   +++++++++++++    +++++++++++++     ++++++++++                   -->
<!--                                                                   -->
<!--                                                                   -->
<!-- Comments:                                                         -->
<!--                                                                   -->
<!-- ================================================================= -->
<!-- RELEASE/PERMISSIONS                                               -->
<!--    Release:   Open                                                -->
```

```
<!--   Internal:  Open                                    -->
<!--   Customer:  N/A                                     -->
<!--                                                     -->
<!-- ============================================================== -->
<material unique_name="FIBRE-AS4-v1" general_name="FIBRE" display_name="AS4 Fibre"
type="fibre">
  <revision value="1" date="2010-02-04" comment="Initial model in revisioning system">
    <density model="default" number_of_parameters="3">
      <parameter name="NominalDensity" parameter_number="1" units="kg/m3" value="1.790E+03" />
      <parameter name="T0" parameter_number="2" units="C" value="20." />
      <parameter name="Tf" parameter_number="3" units="kg/(m3 K)" value="0." />
    </density>
    <specific_heat model="default" number_of_parameters="3">
    <!-- Note: Cp has also been given as 712.2 and 904.0 nominal, with
            T0=20, Tf=0 and T0=75, Tf=2.05 respectively
            in the AS435016.DAT and AS48552.DAT files -->
      <parameter name="NominalCp" parameter_number="1" units="J/(kg K)" value="750." />
      <parameter name="T0" parameter_number="2" units="C" value="0." />
      <parameter name="Tf" parameter_number="3" units="J/(kg K2)" value="2.05" />
    </specific_heat>
    <conductivity model="default" number_of_parameters="5">
    <!-- Here too, the AS43501 data file reports conductivities different than below
        K11=2.6, K33=2.6, T0=20, Tf1=0, Tf2=0

        The above parameters do not seem reasonable -->
      <parameter name="NominalKt" parameter_number="1" units="W/(m K)" value="2.4" />
      <parameter name="NominalKl" parameter_number="2" units="W/(m K)" value="7.69" />
      <parameter name="T0" parameter_number="3" units="C" value="0." />
      <parameter name="Tft" parameter_number="4" units="W/(m K2)" value="1.560E-02" />
      <parameter name="Tfl" parameter_number="5" units="W/(m K2)" value="5.070E-02" />
    </conductivity>
    <cte model="cte1" number_of_parameters="5">
      <parameter name="NominalCTEl" parameter_number="1" units="1/K" value="-3.6E-07" />
      <parameter name="NominalCTEt" parameter_number="2" units="1/K" value="4.83E-06" />
      <parameter name="T0" parameter_number="3" units="C" value="20." />
      <parameter name="Tft" parameter_number="4" units="1/K" value="0." />
      <parameter name="Tfl" parameter_number="5" units="1/K" value="0." />
    </cte>
    <elastic_properties model="default" number_of_parameters="15">
      <parameter name="E11" parameter_number="1" units="Pa" value="2.100E+11" />
      <parameter name="E11_refT" parameter_number="2" units="C" value="0" />
      <parameter name="E11_Tf" parameter_number="3" units="Pa/C" value="0" />
      <parameter name="E33" parameter_number="4" units="Pa" value="1.724E+10" />
      <parameter name="E33_refT" parameter_number="5" units="C" value="0" />
      <parameter name="E33_Tf" parameter_number="6" units="Pa/C" value="0" />
      <parameter name="G13" parameter_number="7" units="Pa" value="2.760E+10" />
      <parameter name="G13_refT" parameter_number="8" units="C" value="0" />
      <parameter name="G13_Tf" parameter_number="9" units="Pa/C" value="0" />
      <parameter name="nu13" parameter_number="10" units="Pa" value="0.2" />
      <parameter name="nu13_refT" parameter_number="11" units="C" value="0" />
      <parameter name="nu13_Tf" parameter_number="12" units="Pa/C" value="0" />
```

```
      <parameter name="nu23" parameter_number="13" units="Pa" value="0.25" />
      <parameter name="nu23_refT" parameter_number="14" units="C" value="0" />
      <parameter name="nu23_Tf" parameter_number="15" units="Pa/C" value="0" />
    </elastic_properties>
  </revision>
</material>
```

Example File for Matrix Material Data Sheet – AS4-3501-6 Composite

```
<!-- $Id: MATRIX-HEXCEL-3501-6-v1.xml 2486 2010-02-05 22:20:24Z anthony $ -->
<!-- ============================================================= -->
<!-- Convergent Common Component Architecture (CCA) for COMPRO/Raven  -->
<!--                                                               -->
<!-- Convergent Manufacturing Technologies Inc.                    -->
<!-- 6190 Agronomy Road, Suite 403                                 -->
<!-- Vancouver, British Columbia, Canada                           -->
<!-- support@convergent.ca  or www.convergent.ca                   -->
<!--                                                               -->
<!-- (c)2008 Convergent Manufacturing Technologies, Inc            -->
<!-- All rights reserved.                                          -->
<!-- ============================================================= -->
<!--                                                               -->
<!--      Models          Developer/Source           Date        -->
<!--  ++++++++++++++    ++++++++++++++++++++++      ++++++++++     -->
<!--  Cure Kinetics     PH thesis,p268,TB.1         2008-08-01     -->
<!--                  (x0=0.01,PH thesis,p255)                     -->
<!--                  (xc=0.30,PH thesis,p254)                     -->
<!--  Modulus (E)       source not known - MASKED    2008-08-01     -->
<!--  PR (v)           constant nu=0.37 used        2008-08-01     -->
<!--  Cure Shrinkage    source not known - MASKED    2008-08-01     -->
<!--  Density (ro)      PH thesis,p103,T4.1          2008-08-01     -->
<!--  viscosity         PH thesis,p268,TB.2          2008-08-01     -->
<!--  Heat Capacity     PH thesis,p103,T4.1          2008-08-01     -->
<!--  Conductivity      PH thesis,P103,T4.1          2008-08-01     -->
<!--                                                               -->
<!--                                                               -->
<!-- Comments:                                                     -->
<!--                                                               -->
<!-- ============================================================= -->
<!-- RELEASE/PERMISSIONS                                           -->
<!--   Release:   Open                                             -->
<!--   Internal:  Open                                             -->
<!--   Customer:  N/A                                              -->
<!--                                                               -->
<!-- ============================================================= -->
<material unique_name="HEXCEL-3501-6-v1" general_name="MATRIX" display_name="Hexcel
3501-6 Resin" type="matrix">
  <revision value="1" date="2010-02-04" comment="Initial model in revisioning system">
    <cure_kinetics model="ck1" number_of_parameters="9">
      <parameter name="HeatOfReaction" parameter_number="1" units="J/kg" value="4.740E+05"  />
```

```
      <parameter name="A1" parameter_number="2" units="1/s" value="3.502E+07" />
      <parameter name="DELE1" parameter_number="3" units="J/mol" value="8.070E+04" />
      <parameter name="A2" parameter_number="4" units="1/s" value="-3.357E+07" />
      <parameter name="DELE2" parameter_number="5" units="J/mol" value="7.780E+04" />
      <parameter name="A3" parameter_number="6" units="1/s" value="3.267E+03" />
      <parameter name="DELE3" parameter_number="7" units="J/mol" value="5.660E+04" />
      <parameter name="BB" parameter_number="8" units="none" value="0.4700" />
      <parameter name="AlphaC" parameter_number="9" units="none" value="0.3000" />
      <constraint variable="doc" value="0.01" isMinimum="True" severity_model="1"
initial_severity="100.0" severity_parameters="0.0;100.0;" />
    </cure_kinetics>
    <modulus_development model="rm1" number_of_parameters="7">
      <parameter name="Er0" parameter_number="1" units="Pa" value="3.500E+06" />
      <parameter name="Erinf" parameter_number="2" units="Pa" value="3.500E+09" />
      <parameter name="Gamma" parameter_number="3" units="none" value="0.0" />
      <parameter name="Alpha1" parameter_number="4" units="none" value="0.3500" />
      <parameter name="Alpha2" parameter_number="5" units="none" value="1.0000" />
      <parameter name="TZero" parameter_number="6" units="C" value="0.0" />
      <parameter name="TFact" parameter_number="7" units="1/K" value="0.0" />
    </modulus_development>
    <poissons_ratio model="pr1" number_of_parameters="5">
      <parameter name="NuR0" parameter_number="1" units="none" value="0.37" />
      <parameter name="ANuR" parameter_number="2" units="none" value="0.00" />
      <parameter name="NuRT0" parameter_number="3" units="C" value="0.00" />
      <parameter name="BNuR" parameter_number="4" units="none" value="0.00" />
      <parameter name="NuRA1" parameter_number="5" units="none" value="0.00" />
    </poissons_ratio>
    <cure_shrinkage model="cs1" number_of_parameters="4">
      <parameter name="VSHI" parameter_number="1" units="none" value="0.03" />
      <parameter name="ALC1" parameter_number="2" units="none" value="0.0000" />
      <parameter name="ALC2" parameter_number="3" units="none" value="0.5000" />
      <parameter name="ASH" parameter_number="4" units="none" value="0.03" />
    </cure_shrinkage>
    <density model="default" number_of_parameters="5">
      <parameter name="NominalDensity" parameter_number="1" units="kg/m3" value="1.265E+03" />
      <parameter name="T0" parameter_number="2" units="C" value="20." />
      <parameter name="Tf" parameter_number="3" units="km/(m3 K)" value="0." />
      <parameter name="a0" parameter_number="4" units="none" value="0." />
      <parameter name="af" parameter_number="5" units="none" value="0." />
    </density>
    <viscosity model="1" number_of_parameters="4">
      <!-- viscosity model valid up to 200C (strange behaviour after that). Constraints should be applied. -
->
      <parameter name="MuInf" parameter_number="1" units="Pa s" value="4.600E-17" />
      <parameter name="U" parameter_number="2" units="J/mol" value="1.145E+05" />
      <parameter name="K" parameter_number="3" units="none" value="1.480E+01" />
      <parameter name="Vimax" parameter_number="4" units="none" value="1.E5" />
    </viscosity>
    <specific_heat model="default" number_of_parameters="5">
      <parameter name="NominalCp" parameter_number="1" units="J/(kg K)" value="1260." />
      <parameter name="T0" parameter_number="2" units="C" value="20." />
```

```
      <parameter name="Tf" parameter_number="3" units="J/(kg K2)" value="0.0" />
      <parameter name="a0" parameter_number="4" units="none" value="0." />
      <parameter name="af" parameter_number="5" units="none" value="0.0" />
    </specific_heat>
    <conductivity model="default" number_of_parameters="5">
      <parameter name="NominalK" parameter_number="1" units="W/(m K)" value="0.167" />
      <parameter name="T0" parameter_number="2" units="C" value="20." />
      <parameter name="Tf" parameter_number="3" units="W/(m K2)" value="0.0" />
      <parameter name="a0" parameter_number="4" units="none" value="0.0" />
      <parameter name="af" parameter_number="5" units="none" value="0.0" />
    </conductivity>
  </revision>
</material>
```

Appendix F

Lamina Engineering Constants

$$E_1 = E_{1f}V_f + E_{1m}(1 - V_f) + \left[\frac{4\left(v_{12m} - v_{12f}^2\right)k_f k_m G_{23m}(1 - V_f)V_f}{(k_f + G_{23m})k_m + (k_f - k_m)G_{23m}V_f}\right]$$

$$E_2 = E_3 = \frac{1}{\left(\frac{1}{4k_T}\right) + \left(\frac{1}{4G_{23}}\right) + \left(\frac{v_{12}^2}{E_1}\right)}$$

$$G_{12} = G_{13} = G_{12m}\left[\frac{(G_{12f} + G_{12m}) + (G_{12f} - G_{12m})V_f}{(G_{12f} + G_{12m}) - (G_{12f} - G_{12m})V_f}\right]$$

$$G_{23} = \frac{G_{23m}\left[k_m(G_{23m} + G_{23f}) + 2G_{23f}G_{23m} + k_m(G_{23f} - G_{23m})V_f\right]}{k_m(G_{23m} + G_{23f}) + 2G_{23f}G_{23m} - (k_m + 2G_{23m})(G_{23f} - G_{23m})V_f}$$

$$v_{12} = v_{13} = v_{12f}V_f + v_{12m}(1 - V_f) + \left[\frac{(v_{12m} - v_{12f})(k_m - k_f)G_{23m}(1 - V_f)V_f}{(k_f + G_{23m})k_m + (k_f - k_m)G_{23m}V_f}\right]$$

$$v_{23} = \frac{2E_1k_T - E_1E_2 - 4v_{12}^2k_TE_2}{2E_1k_T}$$

$$k_T = \frac{(k_f + G_{23m})k_m + (k_f - k_m)G_{23m}V_f}{(k_f + G_{23m}) - (k_f - k_m)V_f}$$

Lamina Plate Theory

In-plane force (N) and moment (M) resultants:

$$(\Delta N_x^T, \Delta M_x^T) = \sum_{k=1}^{N}(Q_{11}^k\Delta\epsilon_x^T + Q_{12}^k\Delta\epsilon_y^T + Q_{16}^k\Delta\epsilon_{xy}^T)(1, z)$$

$$\left(\Delta N_y^T, \Delta M_y^T\right) = \sum_{k=1}^{N}(Q_{12}^k\Delta\epsilon_x^T + Q_{22}^k\Delta\epsilon_y^T + Q_{26}^k\Delta\epsilon_{xy}^T)(1, z)$$

$$\left(\Delta N_{xy}^T, \Delta M_{xy}^T\right) = \sum_{k=1}^{N}(Q_{16}^k\Delta\epsilon_x^T + Q_{26}^k\Delta\epsilon_y^T + Q_{66}^k\Delta\epsilon_{xy}^T)(1, z)$$

Transformed plane stress stiffness matrix

$$Q_{11}^{-} = (\cos\theta)^4 Q_{11} + 2(\cos\theta)^2(\sin\theta)^2(Q_{12} + 2Q_{66}) + (\sin\theta)^4 Q_{22}$$

$$Q_{12}^{-} = (\cos\theta)^2(\sin\theta)^2(Q_{11} + Q_{22} - 4Q_{66}) + ((\cos\theta)^4 + (\sin\theta)^4)Q_{12}$$

$$Q_{22}^{-} = (\sin\theta)^4 Q_{11} + 2(\cos\theta)^2(\sin\theta)^2(Q_{12} + 2Q_{66}) + (\cos\theta)^4 Q_{22}$$

$$Q_{16}^{-} = (\cos\theta)^3(\sin\theta)(Q_{11} - Q_{12} - 2Q_{66}) + (\cos\theta)(\sin\theta)^3(Q_{12} - Q_{22} + 2Q_{66})$$

$$Q_{26}^{-} = (\cos\theta)(\sin\theta)^3(Q_{11} - Q_{12} - 2Q_{66}) + (\cos\theta)^3(\sin\theta)(Q_{12} - Q_{22} + 2Q_{66})$$

$$Q_{66}^{-} = (\cos\theta)^2(\sin\theta)^2(Q_{11} + Q_{22} - 2Q_{12} - 2Q_{66}) + ((\cos\theta)^4 + (\sin\theta)^4)Q_{66}$$

Non-zero stiffness Constants in the principle direction

$$Q_{11} = \frac{E_1}{(1 - v_{12}v_{21})}$$

$$Q_{12} = \frac{E_1 v_{21}}{(1 - v_{12}v_{21})}$$

$$Q_{22} = \frac{E_2}{(1 - v_{12}v_{21})}$$

$$Q_{66} = G_{12}$$

Stress free incremental ply strains in global coordinate system

$$\begin{Bmatrix} \Delta\epsilon_x^T \\ \Delta\epsilon_y^T \\ \Delta\epsilon_{xy}^T \end{Bmatrix} = \begin{bmatrix} (\cos\theta)^2 & (\sin\theta)^2 & (\cos\theta)(\sin\theta) \\ (\sin\theta)^2 & (\cos\theta)^2 & -(\cos\theta)(\sin\theta) \\ -2(\cos\theta)(\sin\theta) & 2(\cos\theta)(\sin\theta) & (\cos\theta)^2 - (\sin\theta)^2 \end{bmatrix} \begin{Bmatrix} \Delta\epsilon_1^T \\ \Delta\epsilon_2^T \\ 0 \end{Bmatrix}$$

In-plane strains (ϵ) and curvatures (k)

$$\begin{Bmatrix} \Delta\epsilon_x^{\circ} \\ \Delta\epsilon_y^{\circ} \\ \Delta\epsilon_{xy}^{\circ} \\ \Delta k_x \\ \Delta k_y \\ \Delta k_{xy} \end{Bmatrix} = \begin{bmatrix} a_{11} & a_{12} & a_{16} & b_{11} & b_{12} & b_{16} \\ a_{12} & a_{22} & a_{26} & b_{12} & b_{22} & b_{26} \\ a_{16} & a_{26} & a_{66} & b_{16} & b_{26} & b_{66} \\ b_{11} & b_{12} & b_{16} & d_{11} & d_{12} & d_{16} \\ b_{12} & b_{22} & b_{26} & d_{12} & d_{22} & d_{26} \\ b_{16} & b_{26} & b_{66} & d_{16} & d_{26} & d_{66} \end{bmatrix} \begin{Bmatrix} \Delta N_x^T \\ \Delta N_y^T \\ \Delta N_{xy}^T \\ \Delta M_x^T \\ \Delta M_y^T \\ \Delta M_{xy}^T \end{Bmatrix}$$

Appendix G

Example calculation of spring-in on L-shaped composite laminate due to thermal expansion and resin cure shrinkage. Following the paper written by Albert and Fernlund *Spring-in and Warpage of Angled Composite Laminates*, the following equation has been proven to approximate spring-in of angled laminated due to thermal expansion strains and resin cure shrinkage[15].

$$\Delta\theta = \Delta\theta_{CTE} + \Delta\theta_{CS} = \theta\frac{((\alpha_l - \alpha_t)\Delta T)}{(1 + \alpha_t \Delta T)} + \theta\frac{(\emptyset_l - \emptyset_t)}{(1 + \emptyset_t)}$$

Terms:

$$\Delta\theta_{CTE} = \text{spring in due to thermal expansion}$$

$$\Delta\theta_{CS} = \text{spring in due to resin cure shrinkage}$$

$$\theta = \text{original angle of laminate } (90^{\circ})$$

$$\Delta T = \text{change in temperature from cure temp to final temperature } (180^{\circ} - 20^{\circ})$$

$$\alpha_l = \text{coefficient of thermal expansion in longintudinal direction}$$

$$\alpha_t = \text{coefficient of thermal expansion in through} - \text{thickness direction}$$

$$\emptyset_l = \text{cure shrinkage in longintudinal direction}$$

$$\emptyset_t = \text{cure shrinkage in through} - \text{thickness direction}$$

Values:

$$\theta = 90^{\circ}$$

$$\Delta T = 180^{\circ} - 20^{\circ} = 160^{\circ}$$

The coefficient of thermal expansion (CTE) values and cure shrinkage values were taken from the COMPRO CCA data file for AS4-3501-6 tape properties. The CTE and cure shrinkage values were given for the fiber directions and the direction transverse to the fibers. α_t and $\emptyset_t$ were approximated as equivalent to α_2 and $\emptyset_2$ given the through thickness expansion and cure shrinkage of the resin to be similar to the transverse expansion as both are perpendicular to the fiber direction. For the longitudinal direction, to approximate the fibers running at 45 degrees as in the work done in this paper, a component of the thermal expansion and cure shrinkage was used

$$\alpha_1 = 0\frac{m}{mC^\circ}$$

$$\alpha_2 = \alpha_t = 2.25 \times 10^{-5}\frac{m}{mC^\circ}$$

$$\alpha_l = \alpha_1 \cos(45^\circ) + \alpha_2 \sin(45^\circ) = 0 \times \cos(45^\circ) + 2.25 \times 10^{-5} \times \sin(45^\circ)$$

$$\alpha_l = 1.591 \times 10^{-5}\frac{m}{mC^\circ}$$

$$\emptyset_1 = 0\frac{m}{m}$$

$$\emptyset_2 = \emptyset_t = .01\frac{m}{m}$$

$$\emptyset_l = \emptyset_1 \cos(45^\circ) + \emptyset_2 \sin(45^\circ) = 0 \times \cos(45^\circ) + .01 \times \sin(45^\circ)$$

$$\emptyset_l = .007071\frac{m}{m}$$

Final Calculation:

$$\Delta\theta = \Delta\theta_{CTE} + \Delta\theta_{CS} = 90\frac{((1.591 \times 10^{-5} - 2.25 \times 10^{-5})160^\circ)}{(1 + (2.25 \times 10^{-5})160^\circ)} + 90\frac{(.007071 - .01)}{(1 + .01)}$$

$$\Delta\theta = \Delta\theta_{CTE} + \Delta\theta_{CS} = (-.0946) + (-.261) = -.356$$

$$\boldsymbol{\Delta\theta = -.356}$$

The calculated spring-in is found to be greater than the model and experimental data from this study. This is not unexpected as the geometry used in this study is a T-joint or I-beam while this calculation approximates spring-in for an L-shaped laminate. Despite this difference the above approach has been shown to accurately model the potential spring-in of angled laminates. Typical spring-in values for angled laminates can fall between 0° and 1° with .5° being very common. An approximation of .326° is a good estimation of the spring-in expected from this geometry. This equation also does not consider tooling effects and depending on the tool-part interaction this component can be more significant. A tooling material such as aluminum has a higher CTE and will put more strain on the composite than a steel tool which changes shape less as temperature varies. In addition this equation does not consider radius or part thickness, both of which have conflicting literature reports, some papers say these factors influence spring-in while other do not[15].